TUNABLE SLOW AND FAST LIGHT GENERATION AND THE APPLICATIONS IN MICROWAVE PHOTONICS

By

Hiva Shahoei

Thesis submitted to the Faculty of Graduate and Postdoctoral studies in partial fulfillment of the requirements for the Doctorate in Philosophy degree in Electrical and Computer Engineering

Ottawa-Carleton Institute of Electrical and Computer Engineering

School of Electrical Engineering and Computer Science

Faculty of Engineering

University of Ottawa

June 2014

In memory of my father

ACKNOWLEDGMENTS

First of all, I would like to express my deepest gratitude toward my supervisor, Professor Jianping Yao for the immense amount of support and valuable guidance he has provided during my study. His constant encouragement and patient are greatly appreciated. Without his advice and encouragement, this work would never been possible.

Special thanks to Prof. Jacques Albert, Prof. Robert W. Boyd, and Dr. Patrick Dumais for their generosity in passing down their knowledge, their valuable inspiring conversations, and countless helps.

Enormous appreciations are to Chao Wang, Wangzhe Li, Ming Li, Honglei Guo, Yichen Han, Weilin Liu, and Ramon Maldonado-Basilio for their constant help. Inspiring insights from them and having valuable discussions with them help me to do my research as quickly and smooth as possible.

I would like also to thank the following people who are current or former colleagues working with me in the Microwave Photonics Research Laboratory at the School of Electrical Engineering and Computer Science, University of Ottawa: Sebastian Blais, Shilong Pan, Shawn Kostyk, Montasir Qasymeh, Tong Shao, Weifeng Zhang, Wentao Cui, Jiejun Zhang, Fanqi Kong, Yang Chen, Xiang Chen, Liang Gao, Bruno Romeira, Nasrin Ehteshami, and Ruming Li. I will always cherish the good memories of working with them.

I would like to thank my two brothers Veria and Vahid for their assistance and encouragement. Most importantly, I am greatly indebted to my beloved mother Farkhondeh Hosseini and my late father Saber Shahoei whose supports have been invaluable. My father was the symbol of knowledge, effort, and modesty in my family. He was the one who instilled in me the passion for knowledge and diligence. Regret that his short life does not allow him to see my graduation; may he rest in peace. I am greatly thankful for their immeasurable love and support throughout my entire life.

Finally, I would like to thank my beloved husband Himan Hojat Jalali, for all his support from far away. Undoubtedly, without the warmth of his love enduring overseas distance and finishing this work were impossible.

ABSTRACT

In this thesis, new techniques to generate slow and fast light are proposed and investigated. The use of the slow and fast light for microwave photonics applications is also investigated.

This thesis consists of four parts. In the first part, the generation of slow and fast light based on fiber Bragg gratings (FBGs) is studied. Two techniques are proposed. In the first technique, slow and fast light is generated based on a linearly chirped fiber Bragg grating (LCFBG); and in the second technique, slow and fast light is generated based on a tilted fiber Bragg grating (TFBG). Theoretical analysis is performed which is verified by experiments. In the second part, the applications of FBG-based slow and fast light in microwave photonics are studied. These applications include all-optical tunable microwave frequency multiplication, tunable microwave chirped pulse generation, tunable phase shifting, tunable fractional order differentiation, and tunable microwave photonic filtering. In the third part, the generation of slow and fast light based on microring resonators (MRRs) is studied. Novel methods to obtain continuously tunable slow to fast light are proposed and experimentally demonstrated by using a silicon-on-insulator (SOI) MRR with MMI (multi-mode interference) couplers, and a high-contrast Ge-doped silica-on-silicon (SOS) MRR. In the fourth part, the applications of the MRR-based slow and fast light in microwave photonics are studied. These applications include all-optical tunable fractional order differentiation, and tunable fractional order Hilbert transformation.

TABLE OF CONTENTS

LIST OF FIGURES

LIST OF TABLES

LIST OF ACRONYMS

AOT	All optical tuning
ASE	Amplified spontaneous emission
AWGN	Additive white Gaussian noise
BPD	Balanced photodetector
BERT	Bit error rate tester
CFBG	Chirped fiber Bragg grating
CPO	Coherent population oscillation
CROW	Coupled-resonator optical waveguide
CW	Continuous wave
DCDR	Double-waveguide coupled disk
DCF	Dispersion compensating fiber
DFB	Distributed feedback
DSF	Dispersion-shifted fiber
EA	Electroabsorber
EDFA	Erbium-doped fiber amplifier
EO	Electro-optic
Er/Yb	Erbium/Ytterbium
FBG	Fiber Bragg grating
FHT	Fractional Hilbert transformer
FIR	Finite impulse response
FSR	Free spectral range
FWHM	Full-width at half-maximum
FWM	Four wave mixing
HNLF	Highly nonlinear fiber
HT	Hilbert transformer
KK	Kramers Kronig
LCFBG	Linear chirped fiber Bragg grating

LD	Laser diode
LPG	Long period grating
MMI	Multi-mode interferometer
MPF	Microwave photonic filter
MRR	Microring resonator
MZM	Mach-Zehnder modulator
OC	Optical circulator
OEO	Optoelectronic oscillator
ONF	Optical notch filter
OSC	Oscilloscope
OSSB	Optical single-sideband
PC	Polarization controller
PD	Photodetector
PhCW	Photonic crystal waveguide
PIC	Photonic Integrated Chip
PM	Phase modulator
PolM	Polarization modulator
PS-FBG	Phase shifted-fiber Bragg grating
RMSE	Root mean square error
RR	Ring resonator
SAW	Surface acoustic wave
SBS	Stimulated Brillouin scattering
SMF	Single-mode fiber
SOA	Semiconductor optical amplifier
SOI	Silicon-on-insulator
SOS	Silica-on-silicon
SPM	Self-phase modulation
TBWP	Time-bandwidth product
TE	Transverse electric
TFBG	Tilted fiber Bragg grating
TLS	Tunable laser source

TM	Transverse Magnetic
TPS	Temporal pulse shaping
UTPS	Unbalanced temporal pulse shaping
VNA	Vector network analyzer
WDM	Wavelength division multiplexing
XPM	Cross-phase modulation

CHAPTER 1 INTRODUCTION

1.1. Introduction to slow and fast light and their applications in microwave photonics

In the recent years, controlling the speed of light has become an interesting topic which finds numerous applications such as in optical communications, optical signal processing and microwave photonics [1]. The speed of light in a dispersive medium depends on the group refractive index (n_g). In the presence of a normal dispersive medium, the light travels slower than the speed of light in vacuum and is called slow light. On the other hand, in a medium with an anomalous dispersion, the light travels faster than the speed of light in vacuum and is called fast light. Slow light (time delay) and fast light (time advance) have been demonstrated based on different techniques such as electromagnetically induced transparency (EIT) [2], coherent population oscillation (CPO) [3-5], stimulated Brillouin scattering (SBS) [6-9], and wavelength shifting [10, 11].

Fiber Bragg gratings (FBGs) are well known for their unique filtering properties which have been used in variety of lightwave applications [12]. One of the most interesting applications of FBGs is in microwave photonics. The amplitude response and phase response of an FBG can be properly designed and employed to process RF, microwave, and millimeter-wave signals [13]. The amplitude and phase of an optical pulse can be manipulated by passing it through a properly designed FBG. Therefore, FBGs are excellent candidates for slow and fast light generation. In [14], a tunable time delay is achieved in an apodized FBG by introducing a high-power signal (~2 kw). Since the power of the signal is very large, the practical applications of this method are limited. Tunable time delays based on mechanical tunings have also been achieved by using a linearly chirped fiber Bragg grating (LCFBG) [15, 16]. In this method, the tunable range can be large, but the tuning speed is low and the system has a poor stability. Thermal heating has been also used in an LCFBG to demonstrate a tunable time delay [17]. Slow and fast light have been generated using a tilted fiber Bragg grating (TFBG), in which the group delay response is tuned by controlling the refractive index of the medium surrounding the TFBG or via thermal tuning [18]. Again, the tuning speed is low and the tuning resolution is poor.

Recently, photonic integrated circuits (PICs) implemented based on silicon have attracted great interest due to the advantages such as compact size, low loss and high stability. The fabrication process is compatible with the mature electronic integrated circuit technology, thus making the fabrication greatly simplified with significantly reduced cost. Slow and fast light have been demonstrated based on silicon photonics microring resonators (MRRs) [19-30]. The structures include cascaded MRRs [20], zigzag chain of MRRs [21], vertically cascaded MRRs [22], and multi-state microrings [23], which have been used to generate slow and fast light. A tunable slow and fast light can also be generated using an MRR by controlling the mutual mode coupling inside a MRR cavity [24, 25]. In [26], a p-i-n diode is incorporated into a MRR to change the free carrier injection and change the absorption loss of the cavity and consequently achieve electro-optically tunable slow and fast light. In [27], metallic micro-heaters are utilized for the modulation of the bus waveguide-to-cavity coupling, thus the linewidth of the resonance is changed which leads to the change of the group velocity. In [28, 29], the gain in an MRR is changed by optically pumping the ring cavity that is erbium-ytterbium co-doped [28], or by electrically pumping the ring cavity that incorporates an optical semiconductor amplifier (SOA) [29], consequently the linewidth of the resonance is changed and the group delay is changed correspondingly. The main drawback in the schemes in [26-29] is that an additional procedure is needed in the fabrication process, making the fabrication more complicated. In addition, the use of the tuning schemes in [26-29] would increase the circuit footprint. A solution to the problem is to use all optical tuning (AOT). Recently, on-chip generation of a slow and fast light based on stimulated Brillouin scattering (SBS) in a long chalcogenide rib waveguide has been reported [30]. A large time delay (20 ns) and time advance (-10 ps) was achieved. However, the bandwidth was very small (in the order of tens of MHz). In addition, the optical carrier should be tuned at two different wavelengths corresponding to the Stokes and anti-Stokes wavelengths to generate the slow and fast light.

Slow and fast light can find numerous applications in microwave photonics including tunable microwave frequency multiplication or division, microwave chirped pulse generation, tunable phase shifting, fractional order differentiation, fractional order Hilbert transformation, and microwave photonic filtering.

Microwave frequency multiplication or division is an important topic which can find applications in radar systems, communication systems and microwave tomography [31]. In the past few years, numerous techniques have been proposed for achieving microwave frequency multiplication [32-35]. In [32], microwave frequency division or multiplication is demonstrated through dispersively stretching or compressing a highly chirped optical pulse that is modulated by a microwave signal. In this method, the maximum microwave frequency is limited by the dispersion-induced power penalty due to the use of optical double-sideband (DSB) modulation. In [33], optical single-sideband (SSB) modulation was used; thus the limitation in [32] is eliminated. However, the implementation of SSB modulation requires the use of a dual-port intensity modulator and a broadband 90^{o} hybrid, which may increase the complexity of the system. Recently, an approach to achieving frequency multiplication based on a general temporal self-imaging effect was proposed [34]. The frequency upshifting of the microwave signal from 10 to 50 GHz was demonstrated by using this approach. The limitation of this method is that the multiplication factor can only be tuned to specific values since the focused image of the microwave drive signal can only be obtained under specific dispersion conditions called integer Talbot conditions. In [35], continuously tunable frequency multiplication was achieved by using an unbalanced temporal pulse shaping (UTPS) system consisting of two dispersive elements. The tuning was demonstrated by tuning the dispersion of the dispersive elements in the system. In the experimental demonstration, a 6.1 km dispersion-compensating fiber (DCF) was used as the first dispersive element and a length of a single-mode fiber (SMF) was used as the second dispersive element. By changing the length of the second dispersive element, the tunability of the multiplication was achieved. The problem associated with this technique is that the length of the SMF should be changed to achieve frequency tuning which is hard to implement for fast and continuous frequency tuning. In addition, the lengths of the two fibers are long in order to have large dispersion, which makes the system bulky with poor stability.

Photonic generation of microwave waveforms with a large time-bandwidth product (TBWP) has been a topic of interest recently [36]. Large TBWP waveforms can find numerous applications such as in radar systems where the resolution range can be significantly improved. Large TBWP microwave waveforms can also find applications in wireless communications, medical imaging, and instrumentation. To achieve a large TBWP, the waveforms are usually frequency chirped or phase coded. Chirped microwave waveforms are usually generated in the electrical domain using digital or analog electronics, but with relatively low frequency and small bandwidth. For example, a state-of-the-art electronic arbitrary waveform generator can generate microwave waveforms at a sampling rate of 50 Gs/s and a bandwidth of 14 GHz [37], but for many applications microwave waveforms with a bandwidth up to tens of GHz is needed. Thanks to the broad bandwidth and high speed of modern photonics, the generation of chirped microwave waveforms with a large TBWP in the optical domain has been a promising solution. Among the numerous methods [36, 38, 39], those based on pure fiber optics are more interesting since they offer advantages such as smaller size, lower loss, better stability and higher potential for integration [40-44]. A chirped microwave waveform can be generated based on spectrum shaping and wavelength-to-time mapping [42-44]. In [42, 43], an ultra-short pulse from a femtosecond pulsed laser source is shaped by a Sagnac loop filter that has a sinusoidal frequency response. The spectrum-shaped optical pulse is then sent to a dispersive fiber with higher order dispersion [42] or a nonlinearly chirped fiber Bragg grating (NLCFBG) [43] to perform nonlinear frequency-to-time mapping. The chirp rate can be tuned by changing the dispersion nonlinearity of the fiber or the NLCFBG. The limitation of the techniques in [42] and [43] is that the tuning of the chirp rate is difficult, especially in [42], where the nonlinearity of the fiber is tuned by changing the fiber length. A chirped microwave waveform can also be generated by passing an ultra-narrow microwave pulse through a microwave delay-line filter with a quadratic phase response or equivalently a linear group delay response which can be implemented using a non-uniformly spaced photonic microwave delay-line filter [45].

However, the limitation of this technique is that the tuning of the chirped profile is done by tuning the wavelengths of the laser sources, which makes the system complicated and costly.

A microwave phase shifter implemented based on photonics can generate a tunable phase shift at a high frequency over a broad bandwidth with a large tunable range, which is particularly useful for applications such as phased-array antennas [46, 47], and microwave filters [48]. So far, several photonic schemes have been reported for the purpose of implementing microwave phase shifters [49-52]. For instance a phase shift of 114^o at 3 GHz was obtained by using a distributed-feedback (DFB) laser through optical wavelength conversion [53]. In [50], a phase shifter with 18 GHz bandwidth and 360^o tuning range was demonstrated based on SBS in an optical fiber in which the phase tuning was achieved by changing the optical carrier wavelength. The slow and fast light effects induced by CPO in semiconductor optical amplifiers (SOAs) have been also used to implement microwave photonics phase shifters [51-54]. A 200^o phase shifter at a microwave frequency of 1 GHz was realized in a 2.5-mm quantum-well SOA [51]. By cascading two SOAs with two electroabsorber sections, a phase shift of 110^o at 4 GHz was achieved [52]. In [53], a continuously tunable phase shift of 240^o at 19 GHz was demonstrated by cascading three SOAs. However, the use of multiple SOAs makes the structure more complicated especially when a larger range of phase shift with a wider bandwidth is needed. Recently, Capmany and his group have demonstrated a 360^o phase shift at 20 GHz by using a single SOA [54]. The phase shift was achieved by tuning the carrier wavelength and the optical input power injected to the SOA. Although a full phase shift of 360^o was achieved in [54], the phase shift tuning was realized by changing the carrier wavelength, and as a result, the phase shift is not constant for different microwave frequencies or at least by changing the microwave frequency the injection current to the SOA should be changed accordingly in order to achieve a constant phase shift.

With the rapid development of photonic technologies, the implementation of basic signal processing functions in the optical domain has been considered as an effective solution for ultra-wideband signal processing. A differentiator is one of these essential signal processing elements which provides the *n*-th order time derivative of the complex envelope of an arbitrary input optical pulse. In addition to signal processing purposes [55], a temporal differentiator can also be used for ultra-fast signal generation [56, 57], and ultra-high-speed coding [58, 59]. Numerous techniques have been proposed recently to perform an all-optical temporal differentiator. In [60], a temporal differentiator is implemented based on cross-gain-modulation (XGM) in a SOA. A temporal differentiator can also be achieved by using a long period grating (LPG) [61], a π-phase shifted fiber Bragg grating (PS-FBG) [62, 63], and a micro-ring resonator [64]. In addition to the implementation of a regular first-order differentiator, a temporal differentiator with a fractional order can also be implemented. A fractional order differentiator is the generalized format of a regular first-order differentiator which provides us with an additional degree of freedom. In [65], a photonic fractional order differentiator based on an asymmetrical PS-FBG in the reflection domain was demonstrated. The limitation of this technique is the absence of the differentiation order tunability.

Another main signal processing block is a Hilbert transformer (HT) [66] including a classical HT (with an order of 1) and a fractional HT (FHT) (with a tunable order). A fractional Hilbert transformer HT (FHT) is a generalized form of a classical HT which provides us with an additional degree of freedom [67]. Different methods have been proposed to implement a HT or a FHT. Generally, a HT can be implemented based on free-space optics

[67, 68], fiber optics [69-75], and integrated optics [76, 77]. Free-space optics-based HTs usually have large size, heavy weight and high loss, which may not be suitable for applications where light weight and small size are required. Fiber-optics-based HTs have been extensively investigated due to the advantages of smaller size and light weight. In [69-72], a microwave photonic HT was implemented by using a multi-tap microwave photonic filter. To produce a microwave photonic filter with a spectral response corresponding to a Hilbert transformer, negative taps are needed. In [69, 70], the negative taps of the microwave photonic filter were generated by two Mach-Zehnder modulators (MZMs) biased at the quadrature points in the opposite slopes of the transfer functions. In [71], the negative taps were generated based on polarization-modulation to intensity-modulation inversion. A tunable FHT based on a non-uniformly spaced delay-line microwave photonic filter was proposed and demonstrated [72]. A sampled fiber Bragg grating (FBG) was used to implement a classical HT [73]. A HT can also be implemented using a uniform weak-coupling FBG with a π-phase shift [74]. Recently, the inverse scattering method has been used to design and fabricate an FBG to implement a classical HT [75]. On the other hand, the implementation of a HT based on a photonic integrated circuit (PIC) has been extensively researched. Compared with fiber-optics-based implementation, the implementation based on a PIC has significant advantages such as greatly reduced size, and significantly increased long term stability. In addition, the ruggedness and low cost offered by PIC-based solutions are also highly expected for practical applications. In [76], a Bragg grating written in a planar silicon-on-silica (SOS) waveguide was used to implement a HT. Recently, Zhuang et al. proposed a tunable FHT using an integrated MRR-based optical all-pass filter [77], in which the fractional order was tuned via thermal tuning the coupling

coefficient and the loss factor via changing the currents sent to the two resistor-based heaters. However, this tuning mechanism needs an additional procedure in the fabrication process, and also requires additional electrical power supplies. In addition, the thermal tuning is a relatively a slow procedure, with a response time between 1 to 50 ms. To achieve fast tuning, all-optical approach is needed.

One of the key functions of a microwave photonic system is microwave filtering. For microwave filtering, it is desirable that the filter has large frequency tunability and a high Q factor. Numerous techniques have been proposed to implement photonic microwave filters in the last few years [78-80]. In general, a photonic microwave filter can be implemented in the optical domain based on a delay-line structure with multiple taps. A delay-line filter has a finite impulse response (FIR) and is also called a FIR filter. To avoid optical interference which is very sensitive to environmental perturbations, a photonic microwave filter is usually implemented in the incoherent regime. It is known that an incoherent photonic microwave filter has only positive coefficients, or special designs have to be employed to generate negative or complex coefficients. Based on signal processing theory, a FIR filter with all positive coefficients can only function as a low-pass filter. For many applications, however, band-pass filters are needed. The advantage of a photonic microwave FIR filter with complex coefficients is that the shape of the spectral response is maintained unchanged when the filter is tuned by tuning the phase terms of the coefficients. Thus, it is highly desirable to design and implement a photonic microwave FIR filter with complex coefficients with large tunability. A few techniques have been proposed to generate complex coefficients [81-87]. In [81], the complex coefficients are achieved by using a phase shifter based on optical single-sideband modulation and stimulated Brillouin scattering. In [82], a complex coefficient was generated using a phase shifter consisting of two electro-optic intensity modulators. The phase of the RF signal is shifted by adjusting the bias voltages applied to the two electro-optic intensity modulators. In [83], the slow and fast light effect in a SOA is used to implement a complex coefficient. A tunable two-tap microwave photonic FIR filter was demonstrated based on a phase shifter implemented using a single III-V SOI micro-disk resonator [84]. The phase shift in the complex coefficient was tuned by modifying the refractive index through carrier injection. In [85, 86], programmable wavelength processors have been used to manipulate the amplitude and phase of the filter taps to implement complex coefficients. Recently, a tunable three-tap microwave photonic filter based on a SOI microring resonator with 40 GHz tunability was demonstrated in [87]. In this method, the tunability of the complex coefficients is achieved by tuning of the continuous wave (CW) laser emission wavelength.

1.2. Major contribution of this research work

In this research work, novel solutions for the generation of continuously tunable slow and fast light are proposed and demonstrated. The use of the slow and fast light for microwave photonics applications is also investigated.

First, the generation of slow and fast light based on fiber Bragg gratings (FBGs) is studied. Two techniques are proposed. In the first technique, slow and fast light is generated based on a linearly chirped fiber Bragg grating (LCFBG) [88], and in the second technique, slow and fast light is generated based on a tilted fiber Bragg grating (TFBG) [89]. Theoretical analysis is performed which is verified by experiments.

Then, the applications of FBG-based slow and fast light in microwave photonics are studied. These applications include all-optical tunable microwave frequency multiplication [90], tunable microwave chirped pulse generation [91], tunable phase shifting [92], tunable fractional order differentiation [93], and tunable microwave photonic filtering [94, 95].

The generation of slow and fast light based on microring resonators (MRRs) is studied [96]. Novel methods to obtain continuously tunable slow to fast light are proposed and experimentally demonstrated by using a silicon-on-insulator (SOI) MRR with MMI (multi-mode interference) couplers, and a high-contrast Ge-doped silica-on-silicon (SOS) MRR.

Finally, the applications of the MRR-based slow and fast light in microwave photonics are studied. These applications include all-optical tunable fractional order differentiation [97], and tunable fractional order Hilbert transformation [98].

1.3. Organization of this thesis

This thesis consists of seven chapters. In Chapter 1, a brief introduction to slow and fast light and their applications in microwave photonics are presented. The background review of important schemes which have been proposed up to now to achieve tunable slow and fast light are presented in Chapter 2. In Chapter 3, the theoretical study and experimental demonstration of slow and fast light based on FBGs are presented. More specifically, the mathematical models of FBGs are presented in Section 3.1. In Section 3.2 and Section 3.3, schemes to achieve tunable slow and fast light based on an LCFBG and a TFBG are proposed and demonstrated experimentally. In Chapter 4, different applications of the FBG-based slow and fast light effects in microwave photonics are investigated. Continuously tunable microwave frequency multiplication, chirped microwave generation, tunable microwave phase shifting, tunable fractional order differentiation, and finally continuously tunable microwave photonic filtering are implemented in Sections 4.1 to 4.5, respectively. In Chapter 5, slow and fast light generation based on an integrated microring resonator (MRR) is presented. Specifically, in Section 5.1, the mathematical model of a MRR is presented. A novel scheme to achieve tunable slow and fast light based on a MRR with MMI (multi-mode interference) couplers is proposed and demonstrated experimentally in Section 5.2. In Chapter 6, two applications of the MRR-based slow and fast light effects in microwave photonics are investigated. More specifically, a continuously tunable fractional order differentiator and a continuously tunable fractional order Hilbert transformer are proposed and demonstrated experimentally in Sections 6.1 and 6.2 respectively. Finally, a conclusion is drawn in Chapter 7 with some recommendations for future works.

CHAPTER 2 BACKGROUND REVIEW OF SLOW AND FAST LIGHT

Controlling the speed of light has been a topic of interest in the past several years, and can find numerous applications such as in microwave filtering, phased array beamforming, phased array antennas, and arbitrary waveform generation [99]. In order to have a tunable delay-line with a large bandwidth, high speed, and large tunability range, it should be implemented in the optical domain.

The term "slow light" describes a technology which changes the propagation of pulses through a medium and results time delays or equivalently subluminal propagation velocities. On the other hand, "fast light" refers to superluminal propagation velocities and results time advances. First we briefly review the fundamentals of pulse propagation.

The phase velocity $v_p = c/n$ is the speed at which a monochromatic wave propagates through a medium with real refractive index n. A pulse of light consists of different wavelengths, and each of them travels at its own phase velocity. In a special case where n varies linearly with frequency, the pulse distortion as a result of different phase velocities preserves the shape of pulse but shifts the peak of it. In this case, the pulse travels at a velocity which is different from the phase velocity and depends on the amount of dispersion. This speed is named the group velocity. The group velocity applied to a pulse with a center frequency of ω_0 is equal to

$$v_g = \left.\frac{d\omega}{dk}\right|_{\omega_0} = \frac{c}{n_g} \tag{2-1}$$

where n_g is the group index and can be written as

$$n_g(\omega_0) = c\left.\frac{dk}{d\omega}\right|_{\omega_0} = n + \omega_0 \left.\frac{dn}{d\omega}\right|_{\omega_0} . \tag{2-2}$$

As can be seen from (2-2) the group index for dispersion-less materials ($\frac{dn}{d\omega} = 0$) is equal to phase index, and the pulse propagates at the phase velocity as expected. If we consider our special case of linear dispersion over the pulse bandwidth, the group index is nearly constant over the region of the pulse spectrum that contains most of the spectral energy. However, if the frequency dependency of n varies significantly from linearity, the group velocity will change over the pulse-bandwidth and will cause an effect that is known as group velocity dispersion (GVD). It means that the pulse will begin to experience distortion effects due to higher order dispersion that may degrade or change the pulse shape. Generally the concept of group velocity is used when the pulse distortion is not very large. Therefore, most slow and fast light experiments attempt to minimize the distortion by limiting the bulk of the pulse spectra energy to the region of linear dispersion, or by using dispersion compensation methods.

The group delay is a common metric used to describe or evaluate slow light systems. For a pulse whose bandwidth is considerably smaller than the region of linear dispersion, the group index is directly proportional to the delay experienced during propagation [100]. If such a pulse traverses through a slow light material of length *L*, the delay experienced by the pulse is

$$\tau_g = \frac{n_g L}{c}. \tag{2-3}$$

It is clear from (2-2) that the group index can be changed dramatically from the phase index by changing dispersive properties of the material. $dn/d\omega$ can be either positive or negative. Positive dispersion slope ($dn/d\omega > 0$) leads to slow light (time delay) and negative dispersion slope ($dn/d\omega < 0$) leads to fast light (time advance).

The Kramers–Kronig (KK) relations are bidirectional mathematical relations, connecting the real and imaginary parts of any complex function which is analytic in the upper half-plane. These relations are often used to calculate the real part from the imaginary part (or vice versa) of response functions in physical systems because for stable systems causality implies the analyticity condition, and conversely analyticity implies causality of the corresponding stable physical system [101]. The relation is named in honor of Ralph Kronig and Hendrik Anthony Kramers.

For achieving the KK relations between the dispersion and loss of a material, we start with the fact that electric susceptibility ($\chi(t) = \chi'(t) + i\chi''(t)$) which is a complex vector, does not change by multiplying with a step function ($\Theta(t)$) in a causal system. Therefore

$$\chi(t) = \chi(t) \times \Theta(t). \tag{2-4}$$

By getting Fourier transform of the both sides of (2-4), we have

$$F[\chi(t)] = F[\chi(t) \times \Theta(t)] = F[\chi(t)] * F[\Theta(t)] \tag{2-5}$$

while $F[\chi(t)] = \int \chi(t) e^{i\omega t} dt$, and $F[\Theta(t)] = \frac{1}{2}\delta(\omega) + \frac{i}{2\pi\omega}$. Therefore,

$$\begin{aligned} &\mathrm{X}(\omega) = \iint \chi(t) e^{i\omega' t} dt \left(\frac{1}{2}\delta(\omega - \omega') + \frac{i}{2\pi(\omega - \omega')} \right) d\omega' = \\ &\frac{1}{2}\int \chi(t) e^{i\omega t} dt + \int \frac{i}{2\pi(\omega - \omega')} \int \chi(t) e^{i\omega' t} dt d\omega' = \\ &\frac{1}{2}\mathrm{X}(\omega) + \frac{i}{2\pi}\int \frac{1}{\omega - \omega'} \mathrm{X}(\omega') d\omega' \end{aligned} \tag{2-6}$$

and we can get the following equations,

$$\mathrm{X}(\omega) = \frac{i}{\pi}\int \frac{1}{\omega - \omega'} \mathrm{X}(\omega') d\omega' . \tag{2-7}$$

$$\mathrm{X}'(\omega) + i\mathrm{X}''(\omega) = \frac{i}{\pi}\int \frac{\mathrm{X}'(\omega')}{\omega - \omega'} d\omega' + \frac{i}{\pi}\int \frac{i\mathrm{X}''(\omega')}{\omega - \omega'} d\omega' . \tag{2-8}$$

Based on (2-8), the imaginary part of X can be linked to the real part and vice versa by grouping real and imaginary terms such as

$$\begin{aligned} \mathrm{X}'(\omega) &= -\frac{1}{\pi}\int \frac{\mathrm{X}''(\omega')}{\omega - \omega'} d\omega' \\ \mathrm{X}''(\omega) &= \frac{1}{\pi}\int \frac{\mathrm{X}'(\omega')}{\omega - \omega'} d\omega' \end{aligned} . \tag{2-9}$$

These KK relations for $\mathrm{X}(\omega)$ relate $\mathrm{X}'(\omega)$ to $\mathrm{X}''(\omega)$ and vice versa. Based on reality condition, $\mathrm{X}'(\omega)$ is an even function, and $\mathrm{X}''(\omega)$ is an odd function. This allows KK relations be written as

$$\mathrm{X}'(\omega) = \frac{2}{\pi}\int_0^\infty \frac{\omega' \mathrm{X}''(\omega')}{\omega'^2 - \omega^2} d\omega' \tag{2-10}$$

$$X''(\omega) = -\frac{2\omega}{\pi}\int_0^\infty \frac{X''(\omega')}{\omega'^2 - \omega^2} d\omega' . \tag{2-11}$$

The frequency dependent complex refractive index ($\eta(\omega)$) is in relation with susceptibility such as

$$\eta(\omega) = \sqrt{1 + X(\omega)} = \sqrt{1 + X'(\omega) + iX''(\omega)} . \tag{2-12}$$

For a dilute media or weak susceptibility, $X'(\omega)$ and $X''(\omega)$ are small, and the approximation $\sqrt{1+X} \approx 1 + \frac{1}{2}X$ can be used which leads to

$$\eta(\omega) = n(\omega) + i\kappa(\omega) \approx 1 + \frac{X'(\omega)}{2} + i\frac{X''(\omega)}{2} \tag{2-13}$$

where $\kappa(\omega)$ is the wave-propagation factor. Comparing real and imaginary terms respectively, we have

$$n(\omega) \approx 1 + \frac{X'(\omega)}{2} \tag{2-14}$$

$$\kappa(\omega) \approx \frac{X''}{2} . \tag{2-15}$$

By considering the relation between the absorption and the wave-propagation vector,

$\alpha(\omega) = 2\kappa(\omega)\frac{\omega}{c}$, where c is the speed of light in vacuum, we can derive

$$\alpha(\omega) \approx \frac{\omega}{c} X''(\omega) . \tag{2-16}$$

By placing (2-15) and (2-16) in (2-10), we have

$$n(\omega) = 1 + \frac{c}{\pi}\int_0^\infty \frac{\alpha(\omega')}{\omega'^2 - \omega^2} d\omega' . \tag{2-17}$$

Therefore, one can get the frequency dependent refractive index from an absorption spectrum. We simplified the math by assuming dilute media, but the result is true in general.

The KK relations can be also achieved for reflection spectrum as well. The reflected lightwave from a dispersive medium can be expressed as a complex exponent such as

$$r(\omega) = \rho(\omega)e^{i\varphi(\omega)} . \tag{2-18}$$

By getting natural logarithm of the both sides of (2-18), we have

$$\ln(r(\omega)) = \ln(\rho(\omega)) + i\varphi(\omega) . \tag{2-19}$$

By comparing (2-19) and ($\chi(t) = \chi'(t) + i\chi''(t)$), we can derive a KK relation for $\ln(r(\omega))$,

$$\begin{aligned} \ln(\rho(\omega)) &= -\frac{1}{\pi}\int \frac{\varphi(\omega')}{\omega - \omega'} d\omega' \\ \varphi(\omega) &= \frac{1}{\pi}\int \frac{\ln(\rho(\omega'))}{\omega - \omega'} d\omega' \end{aligned} . \tag{2-20}$$

It can be seen that the reflection amplitude response and phase response of a system are related through Hilbert-transform. The same relations can be derived out between the transmission amplitude response and phase response of a medium. Therefore, when there is a change in the magnitude response, there would be a change in the phase response and vice versa.

According to KK relations, a gain peak will create a region of large normal dispersion ($dn/d\omega > 0$) which based on (2-1) and (2-2), would result in a small group velocity ($v_g << c$) within the gain bandwidth. A pulse carried by a wavelength in this bandwidth will experience a time delay (slow light, $\Delta\tau > 0$) in comparison with a pulse carried by a wavelength outside the bandwidth. On the other hand, a loss spectrum will create a region of large anomalous dispersion ($dn/d\omega < 0$). Within this region, the group index can be <1 or even negative and a group velocity larger than c ($v_g > c$) or a negative group velocity can be obtained. A pulse that is carried by a wavelength in this loss bandwidth will experience a time advance (fast light, $\Delta\tau < 0$). The amount of the introduced dispersion depends on gain or loss feature such as the strength and bandwidth. By considering a Lorentzian gain feature such as

$$g(\delta) = \frac{g}{1 + \dfrac{\delta^2}{\Omega^2}} \tag{2-21}$$

where $\delta = \omega - \omega_0$ is the detuning from the resonance frequency ω_0, Ω is the resonance linewidth, and g is the value of the intensity gain coefficient at the line center ($\delta = 0$), and using KK relations the refractive index can be derived out such as

$$n(\delta) = n_0 + \left(\frac{gc}{2\omega_0}\right) \frac{\dfrac{\delta}{\gamma}}{1 + \dfrac{\delta^2}{\Omega^2}} \tag{2-22}$$

where n_0 is the real frequency-independent background index. By using (2-2) and (2-22), the group index is calculated such as

$$n_g(\delta) = n(\delta) + \left(\frac{g \cdot c}{2\gamma}\right) \frac{1 - \frac{\delta^2}{\gamma^2}}{(1 + \frac{\delta^2}{\Omega^2})^2}. \quad (2\text{-}23)$$

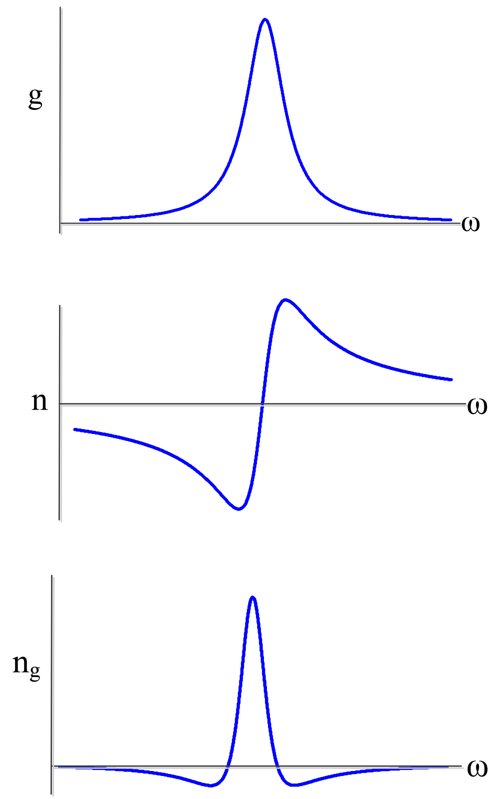

Fig. 2.1. Lorentzian gain peak, corresponding refractive index *n,* and group index n_g associated with this gain spectrum by the KK relations.

The Lorentzian gain peak, and corresponding refractive index *n*, and group index n_g achieved by using KK relations are shown in Fig. 2.1. At the line center, the group delay based on (2-23) is

$$\tau_g = \frac{n_0 L}{c} + \frac{gL}{2\Omega}. \quad (2\text{-}24)$$

As can be seen from (2-24), the pulse delay of $\tau_d = \frac{gL}{2\Omega}$ is an additional delay introduced by the gain feature.

As a general case, by considering both material dispersion and waveguide dispersion in a propagating waveguide, the group velocity can be written as

$$v_g = \frac{\partial \omega}{\partial k} = \frac{c - \omega \dfrac{\partial n(k,\omega)}{\partial k}}{n(k,\omega) + \omega \dfrac{\partial n(k,\omega)}{\partial \omega}} \tag{2-25}$$

where c is the speed of light in vacuum, n is the real part of the refractive index, and k is the waveguide propagation constant. The "slow-down" factor S which is a measure to evaluate slow and fast light systems is expressed as

$$S = \frac{c}{v_g} = \frac{n + \omega \dfrac{\partial n}{\partial \omega}}{1 - \dfrac{\omega}{c}\dfrac{\partial n}{\partial k}}. \tag{2-26}$$

From (2-26), the slow-down factor is tunable by tuning waveguide dispersion $\partial n / \partial k$ and/or material dispersion $\partial n / \partial \omega$. The material dispersion can be achieved by various methods including electromagnetically induced transparency (EIT), coherent population oscillations (CPOs), four-wave-mixing (FWM), stimulated Brillouin scattering (SBS), and stimulated Raman scattering. The waveguide dispersion can be also designed by using different schemes such as different gratings, periodic resonant cavities, and photonic crystal. Both material and waveguide dispersions can be included together in one device in order to increase the slow and fast light effect. In this thesis, we get benefit of the waveguide dispersion for achieving slow and fast light and tune the material dispersion in order to achieve tunability.

In the following part we are discussing some important techniques have been proposed to generate slow and fast light based on either fiber optics such as dispersive fibers, fiber Bragg gratings, stimulated Brillouin scattering (SBS), coherent population oscillation (CPO), and dispersion-conversion in a fiber, or based on integrated optics such as integrated waveguides, microring resonators (MRRs), photonic crystal waveguides (PhCWs), and integrated Bragg gratings. In the following, we will discuss these techniques in detail.

2.1. FBG-based slow and fast light

A fiber Bragg grating (FBG) is a section of an optical fiber in which the refractive index in the core region is perturbed forming a periodic index modulation profile so that certain wavelengths are transmitted and others are reflected. Typical FBGs have grating periods of a few hundred nanometers (nm), which allows mode coupling between two counter-propagation modes in the fiber core. When the Bragg condition is fulfilled, we have maximum mode coupling which leads to maximum reflection. The center wavelength of reflection is called Bragg wavelength λ_B, which is related to the grating period (Λ) by

$$\lambda_B = 2n_{eff}\Lambda \tag{2-27}$$

where n_{eff} is the effective refractive index of the optical fiber core. By modulating the periodic index perturbation in amplitude and/or phase, an FBG with different spectral characteristics can be obtained. More details about the principle of FBGs and the fabrication can be found in Chapter 3. By using an FBG array, a tunable slow light is generated by tuning the wavelength of the optical carrier at the central wavelength of one of the FBGs. This scheme has been used to implement tunable time delays in phased array antennas [102, 103]. A linearly chirped FBG (LCFBG) is achieved by varying grating period along the length of the grating. The chirp in the period of an LCFBG leads to the broadening of the reflection or transmission spectrum. The broadened spectrum is expressed as [104]

$$\Delta\lambda_{chirp} = 2n_{eff}\Delta\Lambda_{chirp}. \tag{2-28}$$

where n_{eff} is the effective refractive index of the grating and $\Delta\Lambda_{chirp}$ is the chirp in the period of grating. The group delay response of an LCFBG is a function of wavelength. A lightwave reflected from an LCFBG would experience a time delay $\tau(\lambda)$ inside the reflection spectrum which is a function of wavelength, and can be expresses as

$$\tau(\lambda) \approx \frac{\lambda_0 - \lambda}{\Delta\lambda_{chirp}} \times \frac{2L}{v_g} \tag{2-29}$$

where λ_0 is the central wavelength of the reflection spectrum, v_g is the average group velocity of the light in the LCFBG, and L is the length of the LCFBG. Based on (2-29), a light wave tuned at a different wavelength would experience a different time delay when reflected by the LCFBG. The maximum time delay depends on the chirp rate and the length of the LCFBG. The reflection spectrum of an LCFBG is shown in Fig. 2.2. As can be seen, it has a broad reflection bandwidth and a linear group delay response. By using this LCFBG, a time delay of $\Delta\tau$ is introduced to an RF signal if it is carried by a light wave at two different wavelengths λ_1 and λ_2, shown in Fig. 2.2(b). Tunable slow light based on an LCFBG has been explored experimentally [105-109]. The use of LCFBG-based tunable slow light (delay-line) for true-time-delay phased array beamforming [107, 108] and tunable transversal filtering [109] have been demonstrated.

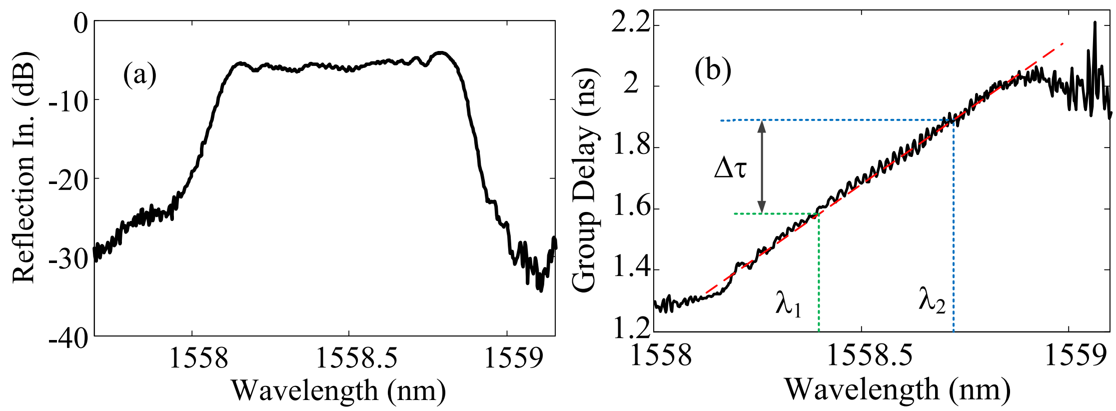

Fig. 2.2. The (a) magnitude and (b) phase spectrums of an LCFBG [88].

2.2. Stimulated Brillouin scattering (SBS)-based slow and fast light

Stimulated Brillouin scattering (SBS) is a nonlinear effect which can be seen in an optical fiber. The SBS effect has been employed to implement slow and fast light. Due to the interaction between a pump field at a frequency of ω_p and an acoustic wave at a frequency of Ω_B, some light would be scattered from the pump field to a counter-propagating Stokes wave at a new frequency given by $\omega_s = \omega_p - \Omega_B$. The beating between the pump light and the Stokes field would increase the acoustic wave which would cause stronger scattering of the pump to the Stokes wave, leading to enhance the SBS. As a result, an exponential gain is experienced by the Stokes wave through propagating in the fiber. At the same time, an exponential loss would be experienced by the anti-Stokes wave at frequency of $\omega_{as} = \omega_p + \Omega_B$ [110, 111]. A probe field near a frequency of ω_s is usually seeded to stimulate the SBS effect. The resulted gain and the loss spectra have a Lorentzian shape with a bandwidth which is inversely proportional to the photon lifetime in the material [112]. The Brillouin frequency shift $v_B = \Omega_B / 2\pi$ for an optical fiber operating near the telecommunication wavelength is typically around 10 GHz and the Brillouin bandwidth $\Delta v_B = \Delta\Omega_B / 2\pi$ is around 35 MHz. The Brillouin gain and loss spectra are shown in Fig. 2.3.

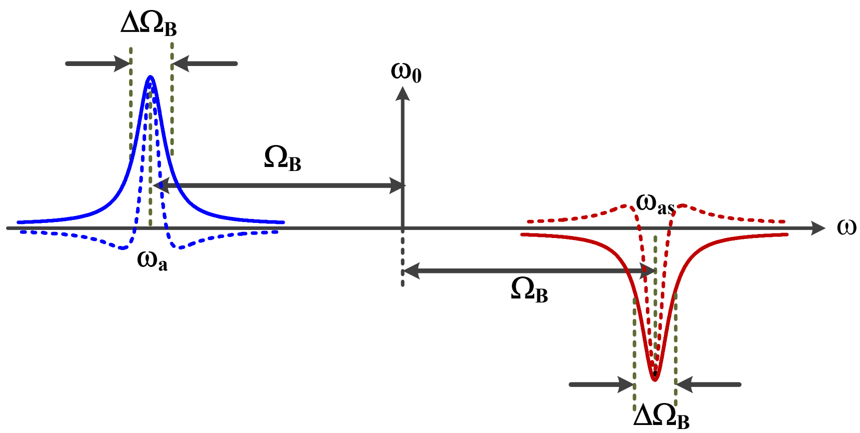

Fig. 2.3. The Brillouin gain and absorption spectra (solid lines), and the corresponding group indices n_g (dashed lines).

According to the KK relations, the refractive index and absorption of a material are related through Hilbert transform. The corresponding group index n_g of the Brillouin gain and loss spectra are also shown in Fig. 2. 3. The Brillouin gain spectrum will create a region of large normal dispersion ($dn/d\omega > 0$) which based on (2-1) and (2-2), would result in a small group velocity ($v_g << c$) within the gain bandwidth. A pulse carried by a wavelength in this bandwidth will experience a time delay (slow light, $\Delta\tau > 0$) in comparison with a pulse carried by a wavelength outside the bandwidth. On the other hand, the Brillouin loss spectrum will create a region of large anomalous dispersion ($dn/d\omega < 0$). Within this region, the group index can be <1 or even negative and a group velocity larger than c

($v_g > c$) or a negative group velocity can be obtained. A pulse that is carried by a wavelength in this loss bandwidth will experience a time advance (fast light, $\Delta\tau < 0$).

In a small signal regime, the slow and fast light achieved by the SBS is considered as a linear slow and fast light since the time delay linearly dependents on the logarithmic signal gain. However, the maximum achievable time delay is limited by the pump depletion. The gain will saturate when the Brillouin system undergoes the pump depletion. The significantly amplified signal may generate another Stokes wave by self-depletion and consequently the signal delay is decoupled from the signal gain [113-115]. The tunability in the SBS-based delay line can be achieved by tuning the pump power, pump frequency, and the optical carrier frequency.

The SBS gain resonance linearly depends on the pump frequency. Thus if a polychromatic pump wave is used in the SBS process, a gain resonance would be resulted from each monochromatic wave and consequently the bandwidth can be increased. Therefore by modifying the pump power spectrum, the spectral distribution of the SBS gain can be shaped and engineered [9, 116-117]. In [116-117], the pump was randomly modulated in order to increase the effective bandwidth. In this method, the presence of the SBS loss resonance has restricted the Brillouin gain bandwidth and inversely, the SBS gain resonance has restricted the Brillouin loss bandwidth. However, in [9] by introducing another pump (pump 2) at a frequency $+2\nu_{\mathbf{B}}$ above the frequency of pump 1, this limitation is solved since the SBS gain resulted by pump 2 will cancel out the SBS loss resulted by pump 1. The broadening of the effective SBS bandwidth led to the significant improvement in the signal bandwidth. Since the amount of time delay is inversely proportional to the bandwidth of the Brillouin resonance, thus an increased pump power is needed to achieve an equivalent time delay if the bandwidth is increased.

Another way to achieve a broadband SBS-based slow and fast light is to use two pumps which are frequency separated in the order of several Δv_B [118-120]. The structure is shown in Fig. 2.4, two pumps are generated by externally modulating a pump beam at an MZM that is biased at the minimum transmission point. A SMF with a length of a few km is used as the SBS gain medium. In between the two SBS gains (gain doublet) resulted from the two pumps, a spectral region with anomalous dispersion appears which can be used to implement a fast light (a negative time delay). On the other hand, in the middle of the loss doublet, a spectral region with a normal dispersion appears which can be used to achieve a slow light (a positive time delay). This scheme is very flexible. For example, by increasing the frequency doublet separation Δv and broadening the pump spectra, the bandwidth of the delay-line can be increased to several GHz. The optimum time delay-bandwidth product in this scheme is achieved for a resonance separation of $\Delta v / \Delta v_B \approx 3$ [119, 120]. By using this method a good adjustment of the time delay and distortion can be achieved. In an SBS system there is a trade-off between the achievable time delay and the amount of distortion which is caused by the magnitude and phase spectral responses of the system, for minimum pulse distortion, a uniform magnitude response and a linear phase response over the finite pulse bandwidth are needed [121-123]. Such a gain and loss doublet can also be achieved by using one pump and two SBS gain mediums with different Brillouin shifts [120]. Since the velocity of the acoustic wave propagating along the fiber determines the Brillouin shift, it is strongly dependent on the mechanical properties of the fiber such as an applied strain or temperature to the fiber [124]. The doping concentrations in the core and cladding of the fiber can also affect the Brillouin shift [125]. The bandwidth of the slow and fast light achieved by this scheme depends on the spectral distance between the two Brillouin shifts. It is easy to find two fibers with two different Brillouin shifts separated by 1 GHz, such as a standard SMF and a DCF. The materials of the two fibers should be different in order to achieve a large Brillouin shift separation. For example, a fluoride or chalcogenide glass shows a Brillouin shift of several GHz lower than that of a silica fiber [126, 127].

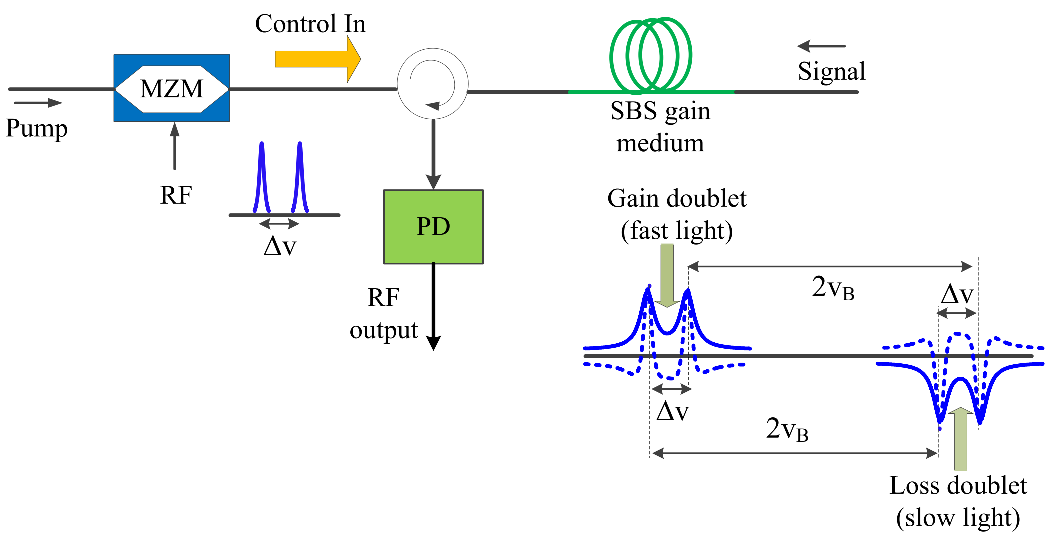

Fig. 2.4. Schematic of a broadened SBS-based slow and fast light by producing a Brillouin gain and loss doublet (solid lines) using two wavelength separated pumps generated by external modulation, and the corresponding group indices n_g (dashed lies). TLS: tunable laser source, MZM: Mach-Zehnder modulator, PD: photodetector.

Although by using the mentioned methods the bandwidth of an SBS-based slow and fast light can be increased, all of them still suffer from the drawback of a significant amplitude change associated with the time delay change, which may affect the use for applications where the signal amplitude is expected to be constant over the entire delay tuning range. For example, in a SBS-based slow light using a standard SMF, a time delay of 30 ns was achieved for a pulse with a temporal width of 100 ns (full-width at half-maximum or

FWHM) while the power change is as large as 30 dB [128]. In order to reduce the amplitude change in an SBS-based slow and fast light, we may combine the gain and loss spectral profiles with identical depth but different widths [129]. The depth and the bandwidth of each spectral profile can be tuned independently in order to achieve an ideal transparent window in the spectral profile of an SBS-based delay-line. In addition, as a result of higher-order dispersion of a SBS-based slow and fast light, the pulse delay is always accompanied by pulse broadening. The time delay and the distortion of the SBS-based slow and fast light have been explored for several kinds of SBS systems [130-132]. It should be noted that SBS-based slow and fast light will never be a candidate for making a distortion-free delay-line [133], and always there is a trade-off between the signal time delay and signal distortion. However, in order to overcome this trade-off, several schemes have been investigated such as combining the SBS effect with FBG [134], using closely spaced SBS gains [122, 123], and designing optimal pump and pulse profiles [121, 135, 136]. Another solution to have a transparent window is to use coherent population oscillation in which narrow atomic absorption lines would produce a large time delay with a much reduced amplitude change.

2.3. Coherent population oscillation (CPO)-based slow and fast light

Coherent population oscillation (CPO) is a quantum effect that generates a spectrally narrow hole in the center of an absorption profile. In a two-level absorption system, by applying an intense optical pump beam at a frequency of ω with the photon energy near the transition energy of the system, atomic population would be depleted in the lower energy state. If a weaker signal beam near an allowed transition at a frequency slightly detuned from the pump beam at $\omega+\Omega$ is applied to the system, as shown in Fig. 2.5(a), atomic population will oscillate between the ground and excited states at a beat frequency Ω. As a result of this temporally modulated ground state population, light is scattered from the pump to the probe and causes a reduced absorption of the probe wave. Consequently, a hole is generated in the absorption spectrum of the probe beam, as shown in Fig. 2.5(b) [112, 137]. Based on KK relations, this absorption dip is accompanied with the variation of the refractive index with a positive slope, and based on (2-1) and (2-2), a slow light would be generated. This population oscillation is significant when the detuning frequency Ω is smaller than the inverse carrier life time *T*. Therefore, the CPO bandwidth is limited by *T*, and gigahertz bandwidth can be provided in semiconductor quantum wells and quantum dots. Practically, it is not necessary to use two separate beams as the pump and probe; they can be generated by different methods such as using a single beam with temporal modulation or a single strong pulse which is self-delayed. Instead of using an absorption medium, we may use an amplifying medium. As a result of CPO, a spectral dip is created in the gain spectrum of the probe beam, which based on KK relations, would result in a fast light. The spectral properties resulted by CPO has been explored for implementing slow and fast light at room temperature in different materials such as crystals [3, 138], semiconductors [139-147] including quantum wells, quantum dots, and quantum structure optical amplifiers, and erbium-doped fibers [4, 148, 149]. For example, a CPO-based slow and fast light based on a quantum-well semiconductor optical amplifier (SOA) was demonstrated [146, 147]. The intensity modulated signal composes a strong central carrier at frequency ω_0 and two weak sidebands at $\omega_1 = \omega_0 + \Omega$ and $\omega_2 = \omega_0 - \Omega$. The two sidebands and a strong carrier work as probe and pump beams. Beating between the strong pump and the weaker beam at ω_1 leads to the modulation of the carrier density and as a result of CPO effect, light is scattered from the pump to the probe beam, leading to change of the both magnitude and phase of the probe. In addition as a result of wave-mixing in the non-linear medium (SOA), another component of the pump is scattered to the mirror frequency of the probe beam at ω_2 and built up a conjugate signal which leads to change of the magnitude and phase of the initial signal at ω_2. The initial signal at the mirror frequency ω_2, with the same mechanism explained above, also leads to the contribution at the both sides. Therefore, the magnitude and phase of the different components of the modulated signal are changed by passing through the SOA, and after beating through the PD, a time delay is introduced to the RF signal [52, 140]. The tunability in this slow and fast light is achieved by controlling the input optical power to the SOA, RF modulating frequency, and amplification of the SOA by changing the injection current [146, 147]. The use of SOA-based slow and fast light to achieve a fully tunable microwave photonic notch filter with a central frequency around 30 GHz was demonstrated [83]. By cascading sections of SOAs and electroabsorbers (EAs), a slow light with a larger time delay and a net gain can be achieved [142, 147]. This SOA-EA-based slow light has been used to implement a phased array antenna [150]. By changing the injection current to the SOAs and the bias voltage to the EA sections, both the time delay and amplitude of each radiation line can be adjusted independently. It has been demonstrated that a CPO-based time delay can be increased significantly by optical filtering [151]. A component of the phase shift applied to the sidebands of a modulated signal by passing through a SOA is equal for the both sidebands but in different signs. Therefore, when the carrier and sidebands are detected by a photodetector, this phase portion is canceled out. By using filtering after CPO system to cancel out one sideband, the phase change and correspondingly the time delay is increased significantly. In [152], by using optical filtering in an SOA-based slow light, a time delay is increased up to 400 ps. This slow light is used to implement a tunable 10-GHz optoelectronic oscillator (OEO) with a tuning range of 2.5 GHz by using the slow light in the loop of the OEO. In fact, the slow light is continuously tunable by tuning the amount of sideband filtering [152].

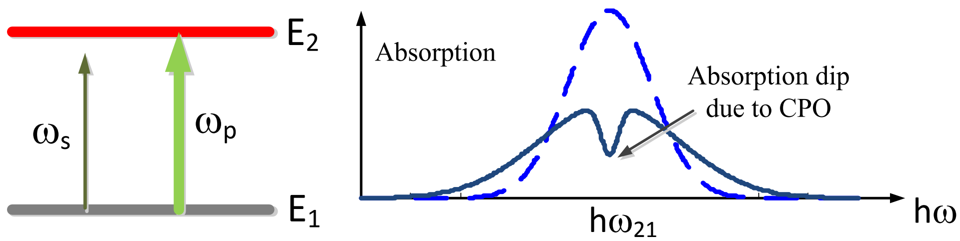

Fig. 2.5. (a) Two-level system in the presence of a resonant pump applied at frequency ω_p and a detuned probe applied at frequency ω_s. (b) absorption spectrum of the probe in the absence (dashed curve) and the presence (solid) of a strong pump.

2.4. Dispersion-conversion (wavelength-shifting)-based slow and fast light

Dispersion-conversion or wavelength-shifting is a novel method to achieve slow and fast light. It is different from a SBS and the CPO-based slow and fast light, a slow and fast light based on dispersion-conversion or wavelength-shifting does not result from the gain or loss spectra. The basic principle of this technique is shown in Fig. 2.6. The input signal to be time-delayed (blue-solid line) is wavelength shifted, and the wavelength-shifted signal (red-solid line) is sent to a dispersive element possessing a large group delay. By passing through the dispersive element, different time delays are introduced to different wavelengths, thus the signal at the new wavelength (red-solid line) acquires a dispersive delay τ_D as compared with the signal at the original wavelength (blue-dotted line). Finally, the pulse is converted back to the original wavelength (blue-solid line). The time delay depends on the product of the wavelength shift and the dispersion of the dispersive element [112]. Therefore, tunability in this delay line can be achieved by tuning these two parameters. The wavelength-shifting has been achieved by four wave mixing (FWM) in a high nonlinear fiber (HNLF) [11, 153, 154] or in a periodically poled lithium-niobate (PPLN) waveguide [10] followed by narrowband filtering. By using this method, 44 ns continuously tunable slow light was demonstrated on a 10 Gbit/s non-return to zero (NRZ) system [10].

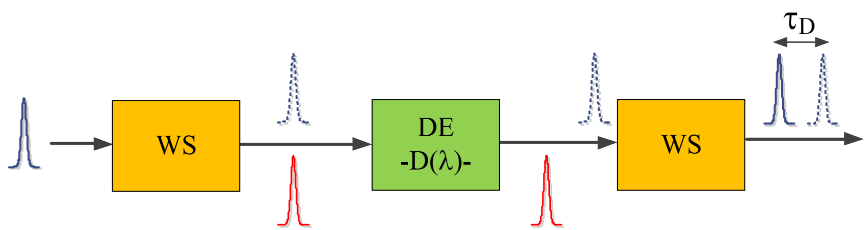

Fig. 2.6. Schematic diagram of a dispersion-conversion based delay-line. WS: wavelength shifter, DE: dispersive element.

2.5. Silicon photonics-based slow and fast light

Silicon photonics has attracted intensive research interest in recent years since photonic circuits implemented based on silicon have compact size and better performance. In addition, due to the compatibility with the mature CMOS fabrication process, photonic circuits based on silicon photonics have much lower cost. Silicon photonics-based circuits can also be used to implement slow and fast light. Microring resonators (MRRs) have attracted significant attention among other silicon photonic structures since they have compact size and good stability. Single and cascaded optical ring resonators have been used to implement tunable slow and fast light [155-161]. A basic schematic diagram of a continuously slow and fast light based on multiple MRRs is shown in Fig. 2.7. It is a coupled-resonator optical waveguide (CROW) consisting of a chain of directly coupled ring-resonators (RRs). The management of the RRs' resonant frequencies is achieved by a tuning control unit. If the spectrum of the input optical signal falls in the passband of the ring with the bandwidth of

$B = 2FSR\sin^{-1}(t_1)/\pi$ [20], where FSR is the free spectral range of the ring and t_1 is the field coupling coefficient between two adjacent resonators, the signal can propagate along the ring, and the ring is called an open ring. Otherwise, the ring is a closed ring. If all rings are closed, the incoming signal cannot access to the rings and it would be directly transferred to the output with no appreciable time delay. If the resonant frequencies of the first M RRs are changed to have open rings, the signal would propagate along all the open rings and would be reflected back at the first closed ring. The delay experienced by the signal would be $T_d = 2M/\pi B$ [20]. The time delay depends on the number of open rings which can be chosen by controlling the round-trip phase shift of the rings. Depending on the waveguide technology, this can be conveniently obtained by thermo-optic or electro-optic controlling. For electro-optic controlling, p-n junction diodes are embedded in the ring waveguide. By applying a voltage to the p-n junction, the refractive index of the ring waveguide is changed through the free-carrier plasma effect which leads to the change of the time delay. For thermo-optic controlling, micro-heaters are added at the top of the ring waveguide, and the time delay is changed as a result of the thermo-optic effect. In [155], a tunable slow light with a time delay of 300 ps has been achieved for a 10-GHz bandwidth signal by using 6 RRs.

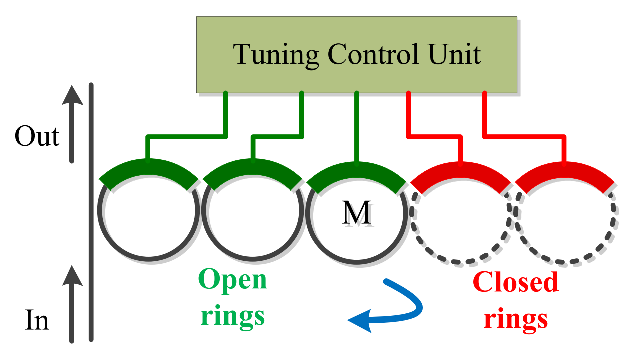

Fig. 2.7. Continuously tunable slow and fast light based on cascaded microrings.

Photonic crystal waveguides (PhCWs) can also be used to implement slow light [162-167]. A photonic crystal line-defect waveguide shows a high group velocity dispersion (GVD) near the transmission band edge. In a specific spectral region, the TE (transverse-electric) group index increases almost linearly in a broad bandwidth. However, the TM (transverse-magnetic) group index is wavelength-independent. This large GVD enables a continuous and wavelength-tunable slow light. For example, in a 4 mm-long PhCW, the group index in the spectral region from 1535 nm to 1550 nm is increased linearly with a slope of $dn_g / d\lambda = 0.45\ nm^{-1}$, which corresponds to a time delay slope of 6 ps/nm and a GVD of 1.5 ps/mm/nm [168]. The corresponding dispersion length L_D for a 9 ps FWHM Gaussian pulse is equal to 15.4 mm [113]. Since for $L << L_D$, where L is the length of the dispersive waveguide, the GVD effect can be neglected, the 4-mm-long PhCW operates almost dispersion-free at bit rates up to 100 Gb/s. The tunability for this delay line can be achieved by tuning the optical carrier wavelength. In [165], a phased array antenna with four channels has been demonstrated by using PhCW-based slow light.

Optical time delay based on integrated structures such as ring resonators and photonic crystal waveguides suffer from high optical losses. A new integrated structure called integrated Bragg grating on an SOI platform has been proposed with a good compromise between the loss and the size [169-171]. The core concept of this scheme is based on engineering the time delay spectrum of the grating waveguide by apodizing the grating through the change of the rib width. The tuning of the time delay can be realized either electronically or thermally. For electrical tuning, the SOI rib waveguide is straddled with a p-n junction diode. By keeping the incident wavelength fixed and applying a voltage to the p-n junction, the refractive index of the rib waveguide is changed through the free-carrier plasma effect.

Thus, the whole delay spectrum of the device is shifted, and the delay would increase or decrease depending on the delay slope at the operating wavelength. For thermal tuning, micro-heaters are integrated on top of the waveguides and as a result of the thermo-optic effect, the time delay is changed. In an integrated Bragg grating, the time delay depends on the length and period of the grating, same as in an FBG. In order to get a larger time delay, a longer grating is needed while it leads to a sharp variation of the group delay response around the operating wavelength. A solution to get a smooth delay response is to use an apodized grating through changing the rib width. In the transmission operation mode of a grating waveguide with an outward supper-Gaussian apodization profile which the grating width increases along the grating, the delay spectrum above the stopband becomes smooth. On the other hand, by using an inward supper-Gaussian apodization profile, the delay spectrum below the stopband becomes smooth [169, 170]. In [170], cascaded apodized grating waveguides with complementary index profile was proposed to compensate the dispersion caused by the grating which enables a high operation bandwidth. By using this technique, a 125-ps thermally tunable slow light at a bit-rate of 355 Gbit/s was demonstrated. However, by using a single Gaussian apodized grating waveguide, a larger tunability (225 ps) can be achieved but at a much lower bit-rate of 23.5 Gbit/s. In [171], a chirped grating with a chromatic dispersion of 500 ps/nm was implemented by using a linear apodization profile in which the rib width is linearly varying along the grating. By using this chirped integrated Bragg grating, a 450 ps thermally tunable slow light at a bit-rate of 25 Gbit/s was demonstrated.

CHAPTER 3 SLOW AND FAST LIGHT BASED ON FIBER BRAGG GRATINGS

3.1. Mathematical model of fiber Bragg gratings

Photosensitivity of silica was first discovered at the Communications Research Centre (CRC) of Canada in 1978 [172], which is the basis that enables the realization of fiber Bragg gratings (FBGs) in a photosensitive fiber. Significant advantages offered by fiber Bragg gratings (FBGs) include all-fiber geometry, low insertion loss, high return loss or extinction, and low cost. The most distinguishing feature of FBGs is the flexibility they offer for achieving desired spectral characteristics by varying numerous physical parameters such as induced index change, length, apodization, period chirp, and fringe tilt. Recently, FBGs have been widely employed for microwave photonics application. In general, microwave photonics is an area that studies the interactions between microwave and optical waves for the generation, processing, control and distribution of microwave, millimeter-wave and THz-frequency signals. In this research work, FBGs are playing a key role in our proposed structures to achieve slow and fast light.

An FBG can be produced by exposing an optical fiber to a spatially varying pattern of ultraviolet intensity. Due to the photosensitivity, a perturbation of the refractive index is achieved along the fiber. By having a periodic index modulation profile along the fiber, certain wavelengths are reflected and others are transmitted. The maximum reflection is obtained at the wavelength for which the phase matching condition (Bragg condition) is satisfied between counter-propagating modes in the fiber core. This wavelength is called Bragg wavelength (λ_B) and is equal to

$$\lambda_B = 2n_{eff}\Lambda \tag{3-1}$$

where Λ is the grating period and n_{eff} is the mode effective refractive index of the optical fiber. Different frequency responses may be obtained by modulating the periodic index perturbation in amplitude and/or phase.

Coupled-mode theory [173-175] is a useful tool for modeling FBGs and obtaining the quantitative information on the spectral properties (both magnitude and phase). By considering $R(z)$ and $S(z)$ as two counter-propagating modes in the fiber core, the coupled-mode equation can be written as [176],

$$\begin{aligned} \frac{dR}{dz} &= j\hat{\sigma}R(z) + j\kappa S(z) \\ \frac{dS}{dz} &= -j\hat{\sigma}S(z) - j\kappa^{*}R(z) \end{aligned} \tag{3-2}$$

where $R(z) = A(z)\exp(j\delta z - \phi/2)$, $S(z) = B(z)\exp(-j\delta z + \phi/2)$ and $A(z)$ and $B(z)$ are the amplitude of the counter-propagating modes, δ is the propagation constant detuning, ϕ describes the grating chirp, κ is the "ac" coupling coefficient, and $\hat{\sigma}$ is the general "dc" self-coupling coefficient. The reflectivity of a uniform FBG with the length of L can be derived out by assuming that the forward-going mode is one at the beginning of grating $R(-L/2) = 1$, and no backward going mode exists at the end of grating $S(+L/2) = 0$. By these initial conditions, the amplitude reflection $\rho = S(-L/2)/R(-L/2)$ can be derived out from (3-2) such as

$$\rho = \frac{-\kappa \sinh(\sqrt{\kappa^2 - \hat{\sigma}^2} L)}{\hat{\sigma} \sinh(\sqrt{\kappa^2 - \hat{\sigma}^2} L) + j\sqrt{\kappa^2 - \hat{\sigma}^2} \cosh(\sqrt{\kappa^2 - \hat{\sigma}^2} L)} . \tag{3-3}$$

Then the group delay response τ_g and dispersion D (in ps/nm) for the reflected light can be obtained from the phase pattern of reflection, $\theta = phase(\rho)$, such as

$$\tau_g = \frac{d\theta}{d\omega} = -\frac{\lambda^2}{2\pi c} \frac{d\theta}{d\lambda} \tag{3-4}$$

$$D = \frac{d\tau_g}{d\lambda} = -\frac{2\pi c}{\lambda^2} \frac{d^2\theta}{d\omega^2} . \tag{3-5}$$

By modulating the refractive index of the FBG, different spectral characteristics can be obtained. Different apodization profiles such as Gaussian can be used to reduce the sidelobes in the FBG's reflection spectrum.

For non-uniform gratings, it is not easy to find out the transmission or reflection spectrum based on (3-2). The most precise numerical method which is used for modeling a non-uniform grating is based on dividing it to some uniform sections, and identifying a 2×2 matrix for each uniform section. By multiplying all of the 2×2 matrices describing uniform sections, a single 2×2 matrix is obtained which describes the whole grating. This numerical method is called piecewise-uniform transfer matrix method [176]. By considering that the whole grating is divided into M uniform sections, and R_i and S_i are amplitudes of the counter-propagating modes after traveling section *i (i=1:M)*, we can start with $R_0 = R(+L/2) = 1$ and $S_0 = S(+L/2) = 0$ and calculate $S(-L/2) = S_M$ and $R(-L/2) = R_M$. The describing matrix of each section is defined as F_i, such as

$$\begin{bmatrix} R_i \\ S_i \end{bmatrix} = F_i \begin{bmatrix} R_{i-1} \\ S_{i-1} \end{bmatrix}, \tag{3-6}$$

$$F_i = \begin{bmatrix} \cosh(\gamma_B \Delta z) - i\dfrac{\hat{\sigma}}{\gamma_B}\sinh(\gamma_B \Delta z) & -i\dfrac{\kappa}{\gamma_B}\sinh(\gamma_B \Delta z) \\ i\dfrac{\kappa}{\gamma_B}\sinh(\gamma_B \Delta z) & \cosh(\gamma_B \Delta z) + i\dfrac{\hat{\sigma}}{\gamma_B}\sinh(\gamma_B \Delta z) \end{bmatrix}, \tag{3-7}$$

where Δz is the length of *i*th uniform section, and $\gamma_B = \sqrt{\kappa^2 - \hat{\sigma}^2}$. It should be noted that κ^2 and $\hat{\sigma}^2$ are local coupling coefficients values in the *i*th section. The simulations done in this research work are all based on this transfer matrix method.

3.2. Tunable slow and fast light based on a linearly chirped FBG

In this section, a new technique to achieve a continuously tunable slow light by using a linearly chirped FBG (LCFBG) written in an Er/Yb co-doped fiber is proposed and experimentally demonstrated. By introducing a pump power to an LCFBG written in an Er/Yb co-doped fiber, the temperature in the fiber would increase, which would lead to the change of the period and the refractive index distribution of the LCFBG. Consequently, the group delay response would change, resulting in the change of the time delays. In this proposed method, the undesirable birefringence effects existing in the mechanical tuning technique can be avoided. The tuning speed is much faster than the approaches using thermal heating or mechanical tuning. Despite thermo-electric heating, this pump induced thermo-optic heating is rapid and localized which does not need additional procedure during fabrication or additional setup for heat controlling such as a heat sink, sealed environment and feedback.

An LCFBG is an FBG in which the period varies linearly with the length of grating. The chirp is applied in several ways including exposure the fiber to UV beams of linear intensity of fringe pattern, applying strain, using a chirped phase mask. We used a chirped phase mask for fabricating LCFBGs[1].

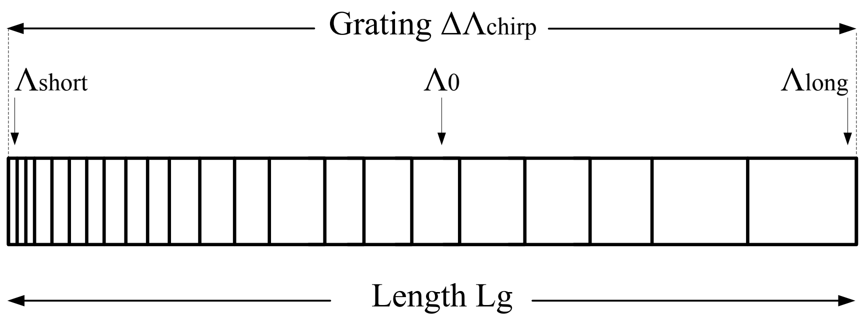

Fig. 3.1. The schematic of a LCFBG.

Fig. 3.1 shows the schematic of a LCFBG of length L_g. By considering the structure in Fig. 3.1, a chirp in the period leads to a chirp in the bandwidth ($\Delta\lambda_{chirp}$) of the fiber grating such as

$$\Delta\lambda_{chirp} = 2n_{eff}(\Lambda_{long} - \Lambda_{short}) = 2n_{eff}\Delta\Lambda_{chirp} \qquad (3\text{-}8)$$

where n_{eff} is the effective refractive index of the grating, $\Delta\Lambda_{chirp}$ is the chirp in the period of the LCFBG, and Λ_{long} and Λ_{short} are the longest and shortest periods of the LCFBG, respectively. The group delay response of a LCFBG is a function of wavelength. A lightwave reflected from the LCFBG would experience a time delay $\tau(\lambda)$ for $2n_{eff}\Lambda_{short} < \lambda < 2n_{eff}\Lambda_{long}$ which is a function of wavelength,

$$\tau(\lambda) \approx \frac{\lambda_0 - \lambda}{\Delta\lambda_{chirp}} \frac{L}{v_g} \qquad (3\text{-}9)$$

where λ_0 denotes the central wavelength of the reflection spectrum, v_g is the average group

1- The phase mask was borrowed from Prof. Jacques Albert's group in Carleton University.

velocity of the light in the LCFBG, and L is the length of the LCFBG. The slope of the time delay in the reflection bandwidth can be calculated as

$$\frac{d\tau(\lambda)}{d\lambda} = \frac{-L}{\Delta\lambda_{chirp} v_g}. \tag{3-10}$$

From (3-10), it can be understood that by changing $\Delta\lambda_{chirp}$, different time delays are induced to a specific wavelength. We have proposed for the first time, continuously changing of $\Delta\lambda_{chirp}$ by pumping the LCFBG with a 980-nm laser diode (LD) with different pump powers. The characteristics of a continuously pumped LCFBG can be explored by modeling the pumping effect in a doped fiber [177]. When a doped fiber is optically pumped, two effects are introduced; the first is the change of the refractive index and the second is the longitudinal expansion of the fiber. Since the second effect amounts to less than 2% of the first one, only the refractive index change due to the thermo-optic effect is considered here. An Er/Yb co-doped fiber has a strong pump absorption (around 2 dB/cm) around 980 nm. Therefore, when it is optically pumped, a large portion of the pumping power can be absorbed which leads to the heating of the fiber. In fact, the temperature rise in the fiber is due to the pump induced heating within the Er/Yb co-doped fiber.

Firstly, it is assumed that the fiber is unjacketed and is long enough such that the z-dependence of the temperature profile is time invariant (z is the position along the fiber). The temperature distribution, $T(r,t)$, should satisfy the heat conduction equation [178],

$$\rho c_v \frac{\partial T(r,t)}{\partial T} - k\nabla^2 T(r,T) = \eta P_v(r), \tag{3-11}$$

where r is the radius position of the fiber, η is the fraction of the absorbed pump power which is turned to heat, k is the thermal conductivity of the fiber, ρ is the density of the fiber material, c_v is the specific heat, and p_v is the average pump power absorbed per unit volume. Since we need steady state condition for the practical case, it is useful to drive the steady-state temperature change relation. In this case the time derivative in (3-11) is zero. For solving this equation, two conditions should be considered. The first one is energy conservation. If the cooling is due to natural air convection, the heat flowing out of the fiber at $r = b$, b is the outer radius of the unjacketed fiber, is proportional to the temperature difference between the fiber and the surrounding air. This proportionality factor is named as heat transfer coefficient h. The second condition is that at $t = 0$; the temperature distribution equals the initial distribution $T(r, t = 0)$. In this regard, s is the absorption boundary, the radius of the step initial profile of $T(r, t = 0)$. By considering these two conditions, the steady state temperature profile can be written as [177]

$$\Delta T_{ss}(r) = \frac{\eta P_v s^2}{2bh} - \frac{\eta P_v s^2}{2k} \ln\left(\frac{r}{b}\right). \qquad (3\text{-}12)$$

To obtain the steady-state index change due to ΔT_{ss}, the absorbed power per unit volume can be expressed as ,

$$P_v(z) = \frac{-1}{\pi s^2} \frac{dP_p(z)}{dz} \qquad (3\text{-}13)$$

where $P_p(z)$ is the pump power distribution along the fiber (which depends on the input pump power, the dopant absorption properties, and the pump mode size). The z dependence of ΔT_{ss}

can be approximated by inserting (3-13) in (3-12) and retaining only the first term. So that the steady state thermal index change is given by

$$\Delta n_{ss}(z) = \frac{\partial n}{\partial T}\frac{-\eta}{2\pi bh}\frac{dP_p(z)}{dz} \tag{3-14}$$

where $\frac{\partial n}{\partial T}$ is the index temperature coefficient. Therefore, depending on the pump power distribution, the refractive index of the fiber would change along the LCFBG, and correspondingly $\Delta\lambda_{chirp}$ is changed leading to changing $\tau(\lambda)$ for a specific wavelength. If the introduced pump is not strong enough to be distributed along all the length of the LCFBG, it would be distributed just in the periods that are located closer to the 980-nm LD. We assume that the probe light is introduced to the LCFBG from the red end (i.e., with the longest period). When the 980-nm pump light is also introduced to the LCFBG from the red end and all the pump power is absorbed before the blue end (i.e., with the shortest period), the temperature at the red end of the LCFBG is increased leads to shift the second reflection edge to a longer wavelength while the first edge is fixed. By inserting (3-14) in (3-8) and (3-9), we can establish the relationship between the pumping power and the time delay as

$$\tau(\lambda) = \frac{\left[n_s\Lambda_s + n_l\Lambda_l + \frac{\partial n}{\partial T}\frac{\eta}{2\pi bh}\frac{dP_p(z)}{dz}\Lambda_l - \lambda\right]}{2\left[n_l\Lambda_l - n_s\Lambda_s + \frac{\partial n}{\partial T}\frac{\eta}{2\pi bh}\frac{dP_p(z)}{dz}\Lambda_l\right]}\frac{L}{v_g} \tag{3-15}$$

where Λ_s and Λ_l are the shortest and longest periods of the LCFBG, and n_s and n_l are the corresponding refractive indices, respectively. Also the slope of the time delay in the reflection band can be written as

$$\frac{\tau(\lambda)}{d\lambda} = \frac{-L}{2\left[n_l\Lambda_l - n_s\Lambda_s + \frac{\partial n}{\partial T}\frac{\eta}{2\pi bh}\frac{dP_p(z)}{dz}\Lambda_l\right].v_g}.\sqrt{a^2+b^2}\,. \tag{3-16}$$

Thus it can be seen that when a LCFBG is pumped from its red end, the absolute value of the slope of the group delay response is decreased, as given by (3-16), and thus the achieved time delay of an optical signal over a specific band is increased. On the other hand, when the LCFBG is optically pumped from the blue end and all the pump power is absorbed before the red end, the temperature at the blue end of the LCFBG is increased and leads to shift the first reflection edge to a longer wavelength while the second edge is fixed. Similarly, the achieved time delay of an optical signal over a specific band is decreased.

An 8 cm-long LCFBG is fabricated by us with UV scanning beam technique using a linearly chirped phase mask with a chirp rate of 0.09 nm/cm. The fiber used to fabricate the LCFBG is a hydrogen-loaded Er/Yb co-doped fiber. The central wavelength of the LCFBG is 1558.38 nm and the reflection bandwidth is 0.45 nm. The group delay changing in this bandwidth is 600 ps, thus the group delay slope achieved by this LCFBG is 1350 ps/nm. Fig. 3.2(a) shows the measured reflection spectra of the LCFBG with different pump powers. The power of the pump laser is small and LCFBG is pumped from the red end, thus by increasing the pump power, the second edge of the LCFBG is shifted to a longer wavelength while the first edge is kept fixed. When the injection current of the pump laser is increased from 0 to 200 mA with a step of 40 mA (the amount of the pump power is changed from 0 to 150 mW), the second reflection edge is shifted to the long wavelength with a wavelength shifting of 0.2 nm. Fig. 3.2(b) shows the group delay responses of the LCFBG in the reflection band. As can be seen, by increasing the pump power, the slope of the group delay is decreased and therefore the amount of achieved time delay of an optical signal at a specific wavelength is increased. By changing the pumping power from 0 to 150 mW, the group delay slope is changed from 1350 to 935 ps/nm.

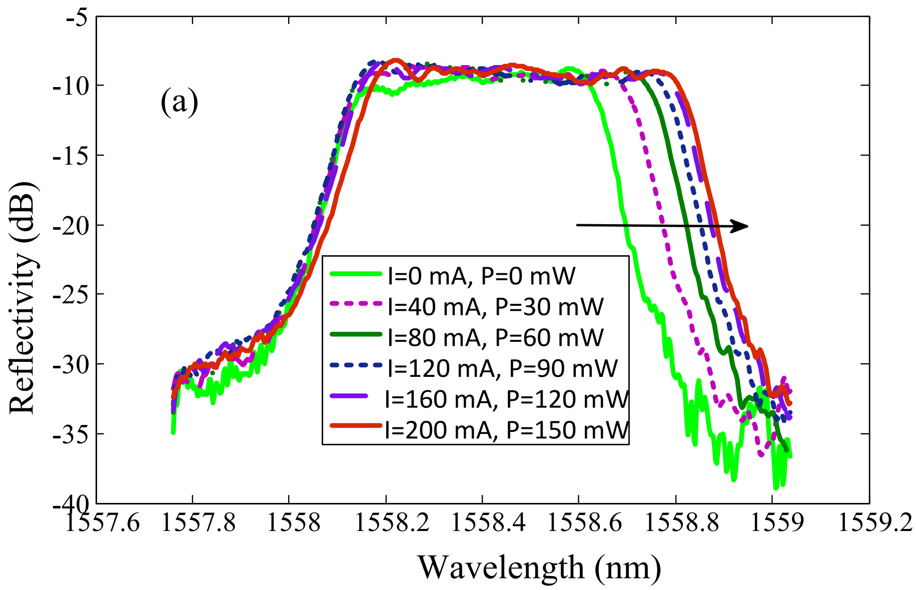

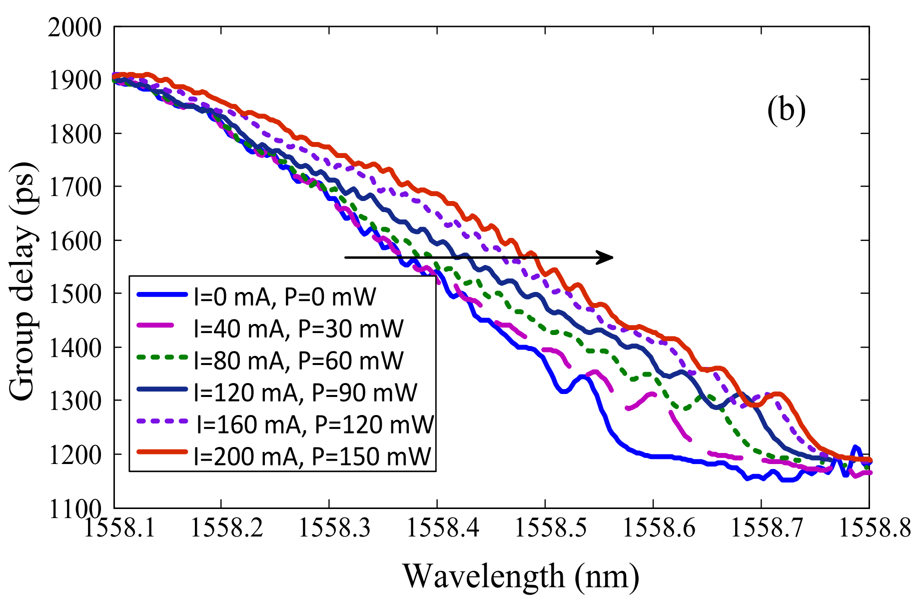

Fig. 3.2. (a) Reflection spectra, and (b) the corresponding group delay response of the LCFBG pumped by a 980-nm laser diode with different pump powers at the reflection band.

As can be seen in Fig. 3.2, there are some ripples in the reflection spectrum and group delay response of the LCFBG. An ideal LCFBG would exhibit a constant reflectivity and linear group delay characteristics over a large bandwidth. However, because of errors in grating periods and refractive index modulation raised in the grating fabrication process, ripples in the reflectivity and group delay spectra would always exist. The impact of the ripples on the delayed signals can be evaluated by modeling the ripples as periodic functions that are superimposed on the reflectivity and time delay responses of an ideal LCFBG. By considering the frequency response of a LCFBG as $R = |R|.e^{-j\theta}$, the reflectivity and its associated time delay can be written as a function of wavelength such as

$$|R(\lambda)| = (1 - r_1) + r_1 \cdot \sin\left(\frac{2\pi}{p} \cdot \lambda\right) \tag{3-17}$$

$$\tau(\lambda) = a_1 \cdot \lambda + a_2 + b_1 \cdot \sin\left(\frac{2\pi}{p} \cdot \lambda\right) \tag{3-18}$$

where r_1 and b_1 are the amplitudes of the reflectivity and the time delay ripples, respectively, p is the period of the ripples, and a_1 and a_2 are constants. The phase response based on (3-4) can be found out by using

$$\theta(\lambda) = -2\pi c \int \left(\frac{\tau(\lambda)}{\lambda^2}\right) d\lambda \tag{3-19}$$

where c is the speed of light in vacuum. Thus, by having the magnitude and phase responses of a non-ideal LCFBG with ripples in the reflectivity and group delay spectra, we can investigate the influence of the ripples on the time-delayed signals. Fig. 3.3 shows the simulated time-delayed signals by an ideal LCFBG with different pump powers. For each case, the frequency response of the ideal LCFBG is modeled by using (3-17) and (3-18). As can be seen from Fig. 3.3(a), by increasing the pump power, the time delay is linearly increasing. Fig. 3.3(b) shows the simulated time-delayed signals based on the measured reflection and group delay spectra of the fabricated LCFBG for different pump powers. The periods and amplitudes of the ripples as well as the constants (i.e., a_1 and a_2) in (3-18) are obtained based on the measured reflection and time delay spectra shown in Fig. 3.2. As can be seen in Fig. 3.3(b), because of the ripples in the reflection and group delay spectra, the time-delayed signals experience some distortions. The amount of distortion depends on the amplitude and the period of the ripples.

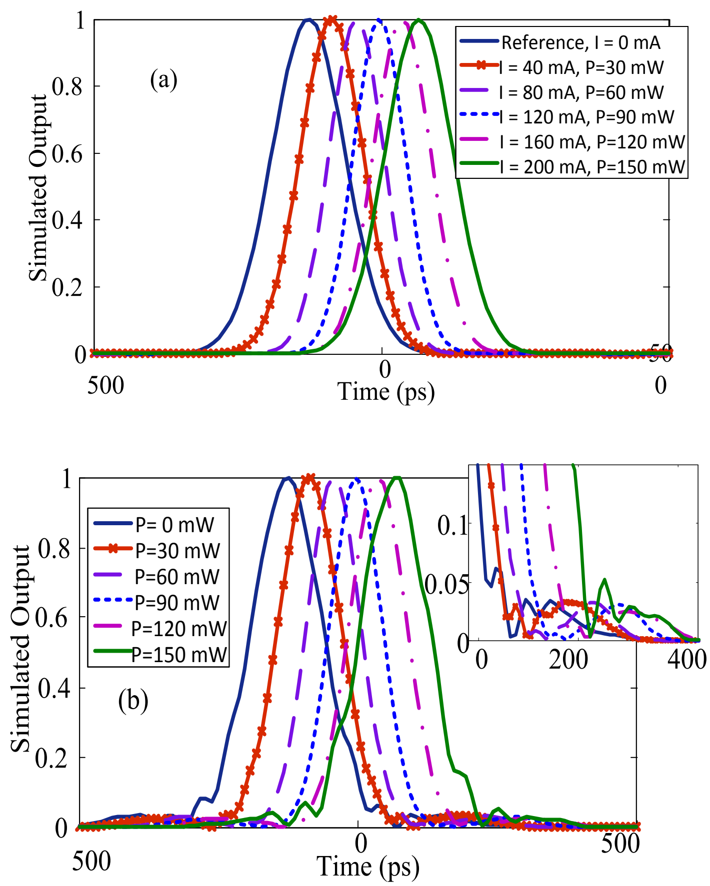

Fig. 3.3. Simulated time-delayed signals reflected from (a) an ideal LCFBG and (b) the experimented non-ideal LCFBG pumped with different powers. The case with no pumping is considered as a reference.

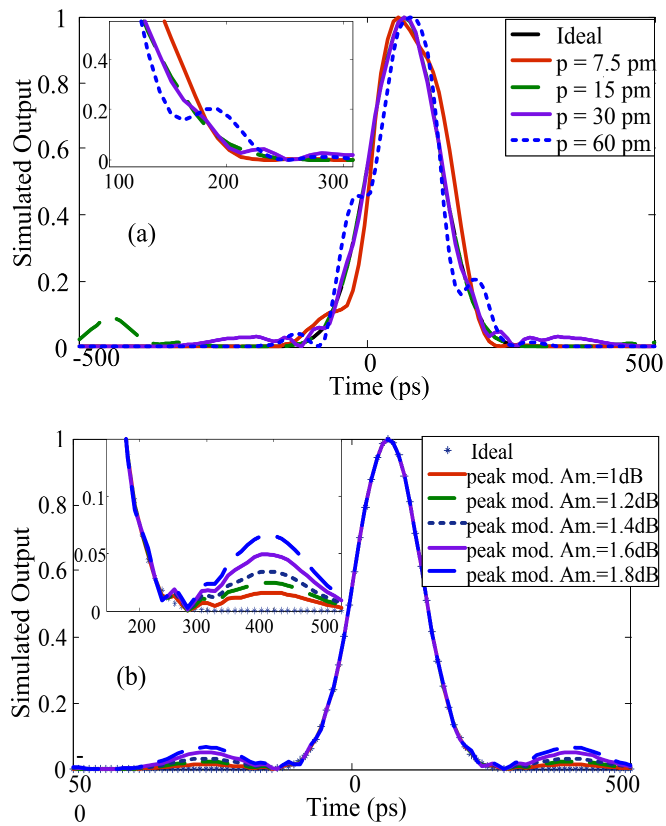

Fig. 3.4. Simulated time-delayed signals reflected from a non-ideal LCFBG with linear time delay but modulated reflection spectra with (a) different ripple period, and (b) different peak to peak ripple amplitude. The insets show the zoom in views of the right edge of the simulated outputs.

To investigate the influence of the reflectivity ripples on the time-delayed signals, a linear group delay is considered. In Fig. 3.4(a), the amplitude of the ripples r_1 is constant (1.2 dB). The period of the ripples of the reflectivity spectrum is increased from 7.5 pm to 60 pm. As can be seen in Fig. 3.4(a), the output does not have a symmetric spectrum. By increasing the period of the ripples, the first left side-lobe gets closer to the main-lobe and its amplitude becomes smaller. In addition to the changing of the amplitude and position of the side-lobe, the simulated signal experiences more distortions. For example, the output gets broader for p = 7.5 ps. In Fig. 3.4(b), the period of the ripples is constant (25 pm) and the peak amplitude of the ripples is increased from 1 to 1.8 dB. By increasing the amplitude of the ripples, the locations of the side-lobes are fixed but the amplitudes become larger. It can be seen that the distortion is predictable when just the amplitude of the ripples in the reflectivity changes, but it is more complicated when its period changes. It is because the maximum and minimum of the ripples fall in different wavelengths by changing the period.

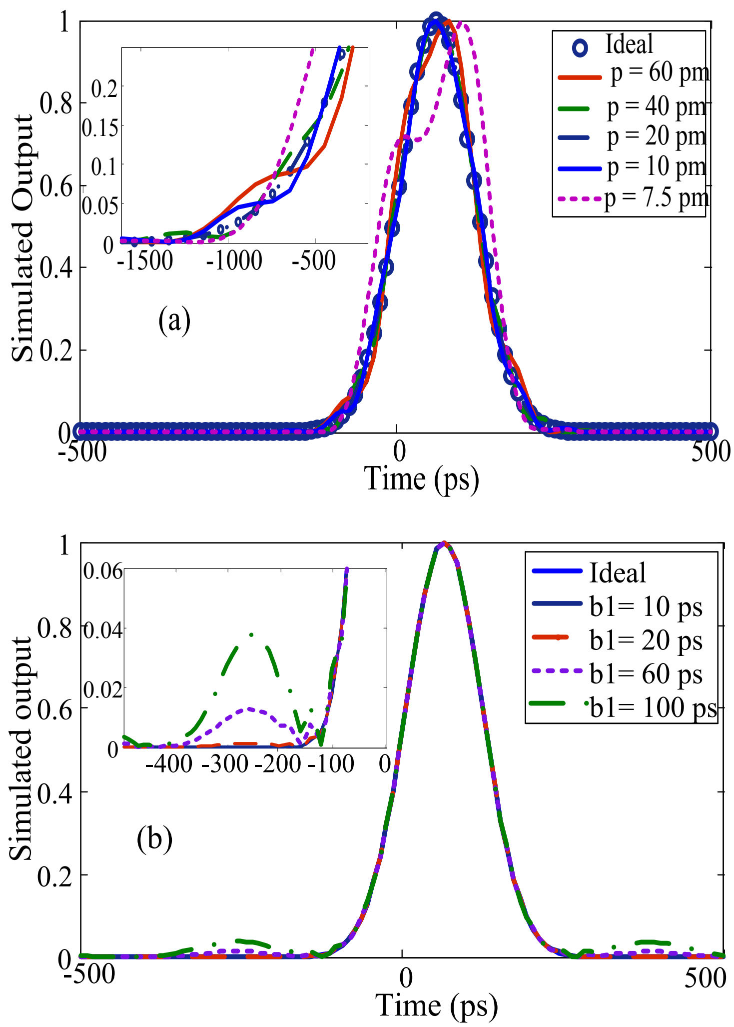

Fig. 3.5. Simulated time–delayed signals for a non-ideal LCFBG with a constant reflectivity but modulated time delay response with (a) different ripples period, and (b) different ripples amplitude. The insets show the zoom views of the simulated outputs.

To study the effect of group delay ripples on the time-delayed signals, a constant reflectivity is considered. In Fig. 3.5(a), the amplitude of the group delay ripples is constant (b_1 = 20 ps) and the period is decreased from 60 to 7.5 pm. As can be seen, we have some distortions in the edge of the signal. The distortion is worst when the period is smallest since time delay changes a lot within a small wavelength band. For p = 7.5 pm, the peak wavelength is shifted and the pulse is distorted significantly near the peak area, also the output pulse gets broader about 31%. Fig. 3.5(b) shows the simulated time-delayed signals for a constant ripple period (25 pm) but different ripple amplitudes in the group delay response. By increasing the ripple amplitude, the locations of the side-lobes are fixed but the amplitudes become lager. It can be seen that the effect of the amplitude ripples in the group delay is not very serious, since for the b_1 = 60 ps, which is a large amount, the side-lobe amplitude is below 0.02. Therefore, depending on the amplitude and period of the ripples in the reflection and time delay spectra, the time-delayed signal would be distorted and the effects of the periods of the ripples are much higher than theirs amplitude.

Another important thing that should be pointed out is the broadening of the time-delayed pulses as a result of passing through a dispersive element (LCFBG). We assume the input Gaussian optical pulse as $g(t) = \exp(-t^2/\tau_0^2)$, where τ_0 is the half bandwidth at $1/e$ maximum. Its Fourier transform is given by $G(\omega) = \sqrt{\pi}\tau_0 \exp(-\tau_0^2\omega^2/4)$, where ω denotes the optical angular frequency. The LCFBG can be modeled as linear time-invariant (LTI) system with a transfer function given by

$$H(\omega) = \exp\left(-j\frac{\ddot{\Phi}\cdot\omega^2}{2}\right) \tag{3-20}$$

where, $\ddot{\Phi}$ donates the second-order dispersion (ps^2/rad) of the LCFBG and $j = \sqrt{-1}$. Here, the higher orders of dispersion are neglected. By increasing the pump power, the slope of the group delay decreases, and thus $\ddot{\Phi}$ decreases. Here, by increasing the pump power from 0 to 150 mW, $\ddot{\Phi}$ decreases from 1739.35 to 1204.66 ps^2/rad. By having the transfer function of the LCFBG for different pump powers (different dispersion amounts) and applying the Gaussian pulse to it, the output pulse can be simulated. Fig. 3.6 shows the simulated outputs of the system for different pump powers. Here, the LCFBG is considered ideal without ripples. It can be seen that the simulated output pulse experience the broadening as the result of the dispersion of the LCFBG. As the dispersion is higher, the broadening is more. It should be noted that the centers of all delayed pulses are shifted to zero in Fig. 3.6, in order to compare the broadening resulted from the dispersion with different values.

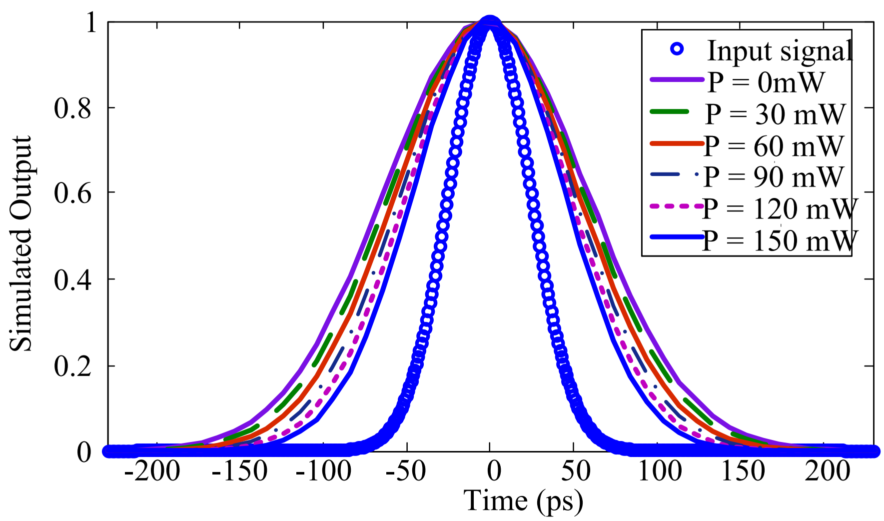

Fig. 3.6. The broadening of the time-delayed signals reflected from an ideal LCFBG pumped with different pump powers, different dispersions.

An experiment has been done to evaluate the proposed scheme experimentally. For this purpose, the setup shown in Fig. 3.7 is used.

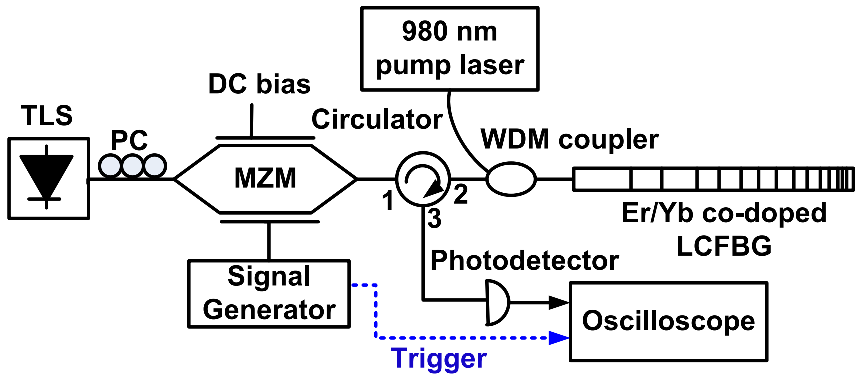

Fig. 3.7. Experimental setup to achieve a continuously tunable time delay. TLS: tunable laser source, MZM: Mach-Zehnder modulator, PC: polarization controller, WDM: 980 nm/ 1550 nm wavelength division multiplexer.

The system consists of a tunable laser source (TLS), a Mach-Zehnder modulator (MZM), a LCFBG, a 980-nm LD, an 3-port optical circulator, a photodetector (PD), a signal generator [Agilent N4901B Serial Bit Error Rate Tester (BERT)], and an oscilloscope (Agilent 86116A). The LCFBG used in the setup is the fabricated LCFBG written in an Er/Yb co-doped fiber shown in Fig. 3.2. The central wavelength of the LCFBG is 1558.38 nm. A lightwave from the TLS is sent to the MZM. The wavelength of the lightwave is tuned at 1558.5 nm. A Gaussian pulse with a full-width at half-maximum (FWHM) of 7.6 GHz generated by the signal generator is applied to the MZM via the RF port to modulate the lightwave. The LCFBG is pumped by the 980-nm LD; by increasing the injection current of the pump laser, the introduced pump power is increased. The Gaussian pulse is reflected back from the LCFBG and applied to the PD via the optical circulator. In the experiment, the LCFBG is fixed on an optical table to minimize the instability caused by the environmental changes. The tunable time delay of the reflected signal is measured by the oscilloscope.

As discussed earlier, in a doped fiber, the core refractive index changes as a consequence of the variation of the pump power. The reflection edge wavelengths of a LCFBG are linearly proportional to the core refractive indices of the shortest and longest periods, as given by (3-8). Fig. 3.8 shows the detected signals reflected back from the LCFBG with different time delays for different pump powers. By increasing the injection current of the pump laser from 0 to 200 mA (the corresponding pump power from 0 to 150 mW), a time delay (slow light) that is continuously tunable up to 200 ps is achieved. The measured intensity of the time-delayed signals shown in Fig. 3.8 is normalized to unity. The time-delayed signals experience some distortions because of the ripples in the magnitude and group delay spectra of the LCFBG as discussed theoretically before.

The stability of the proposed system is also investigated. To do so, the reflection and group delay spectra of the LCFBG are measured every 5 minutes when the injection current of the LD is I = 200 mA or equivalently the pumping power is P = 150 mW. The results are shown in Fig. 3.9. As can be seen, after 25 minutes, the reflectivity and the group delay responses of the LCFBG do not have any visible changes, a high stable operation is confirmed.

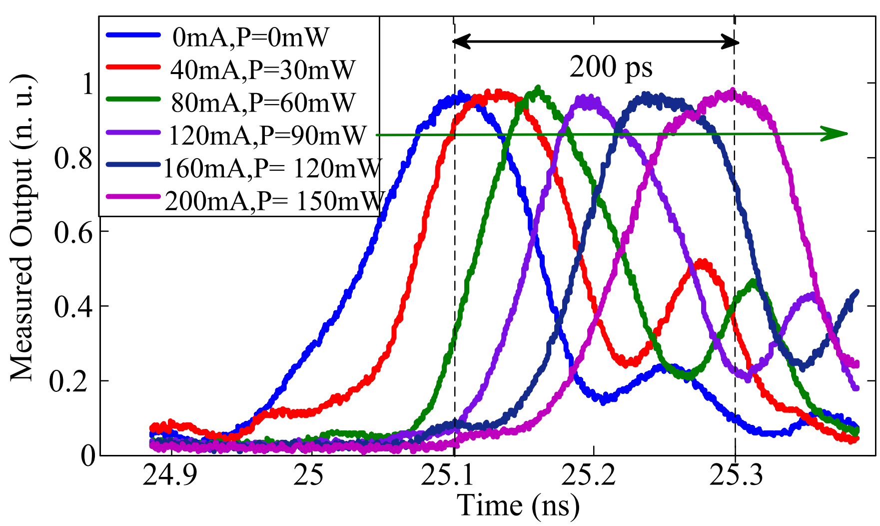

Fig. 3.8. The detected signals reflected from the pumped LCFBG with different pump powers.

The bandwidth of the proposed system is limited by the reflection bandwidth of the LCFBG. In our experiment, since the reflection bandwidth is 0.45 nm, the bandwidth of the system is 56 GHz, and thus the tunable time-bandwidth product which is a figure of merit to evaluate the performance of a time delay system is 11.2, which is a high amount. Also, there is a trade-off between the tunability of the time delay and the broadening of the input pulse. By increasing the dispersion in the LCFBG, time delay has more tunability while the output pulse gets broader. However, by using a dispersion compensating fiber (DCF) the broadening can be compensated.

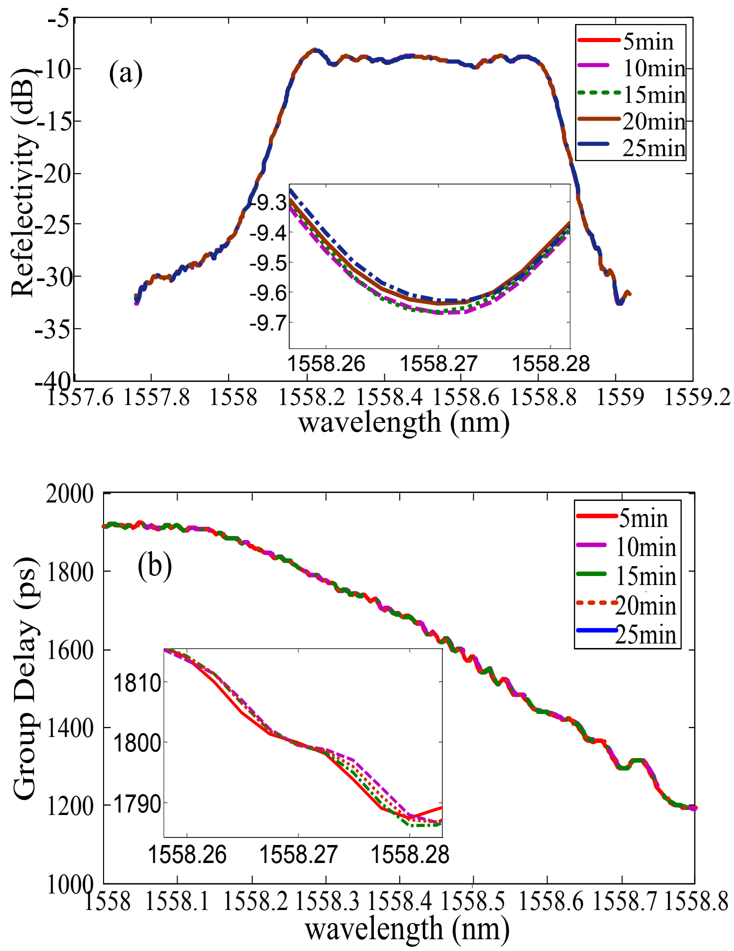

Fig. 3.9. Experimental measurement of the group delay response to evaluate the stability of the system. (a) Reflectivity and (b) Group delay responses of the LCFBG pumped with I = 200 mA at different times. The insets show zoom-in views of the reflectivity and group delay responses.

3.3. Tunable slow and fast light based on a Tilted FBG

In a regular FBG, the variation of the refractive index is along the length of the fiber. In a tilted FBG (TFBG) however, the variation of the refractive index has an angle to the optical axis. The schematic diagram of a TFBG is shown in Fig. 3.10. The tilt angle has an effect on the spectral response. The transmission spectrum of a TFBG consists of two different types of resonances resulted from two different couplings. The first one is the coupling between the forward and backward core modes and the other one is the coupling between the contra-propagating core mode and the cladding modes. The resonance wavelength corresponding to the self-coupling of the core mode and the resonance wavelengths corresponding to contra-propagating cladding modes are given by

$$\lambda_{Bragg} = \frac{2n_{eff,core}\Lambda_g}{\cos\theta} \tag{3-21}$$

$$\lambda_{Bragg} = (n_{eff,cladding} + n_{eff,core})\frac{\Lambda_g}{\cos\theta} \tag{3-22}$$

respectively, where θ is the tilt angle of the TFBG, Λ_g is the nominal grating period shown in Fig. 3.10, $n_{eff,core}$ and $n_{eff,cladding}$ are the effective refractive indices of the core mode and a particular cladding mode, respectively. As discussed in Chapter 2, the group velocity is defined as

$$v_g = c/n_g \tag{3-23}$$

where c is the speed of light in vacuum, and n_g is the group index given by

$$n_g = n + \omega \frac{dn}{d\omega} \tag{3-24}$$

where n is the frequency-dependent refractive index, and $dn/d\omega$ is the first derivative of n with respect to the frequency ω. Since $dn/d\omega$ can be either positive or negative, the group index can be either larger or smaller than unity and a time delay (slow light) or time advance (fast light) can be achieved. Thus, by tuning $dn/d\omega$, the slow and fast light can be tuned.

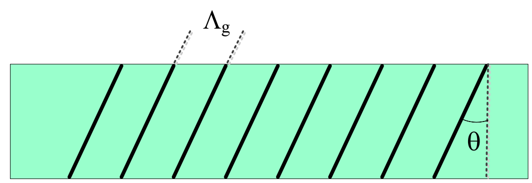

Fig. 3.10. The schematic structure of a TFBG.

For the first time, we have proposed to tune $dn/d\omega$ by optically pumping the TFBG, and thus achieve tunable slow and fast light. Thanks to the high absorption of an Er/Yb co-doped fiber, the refractive index of the fiber is changed by the pumping. In Section 3.2 we have shown that by pumping an FBG written in an Er/Yb co-doped fiber, the refractive index along the FBG changes correspondingly to the pumping profile,

$$\Delta n(z) \propto \frac{dp(z)}{dz}, \tag{3-25}$$

where z is the position along the fiber, $\Delta n(z)$ is the index change along the fiber and $p(z)$ is the pumping power distribution along the fiber. Thus, by pumping the grating with a 980-nm LD with a tunable pump power, the refractive index along the grating is changed which leads to the shift of the resonance wavelengths and the change of the coupling coefficients

[179]. Consequently, the frequency dependency of the refractive index ($dn/d\omega$) is changed, which results in the tuning of the slow and fast light.

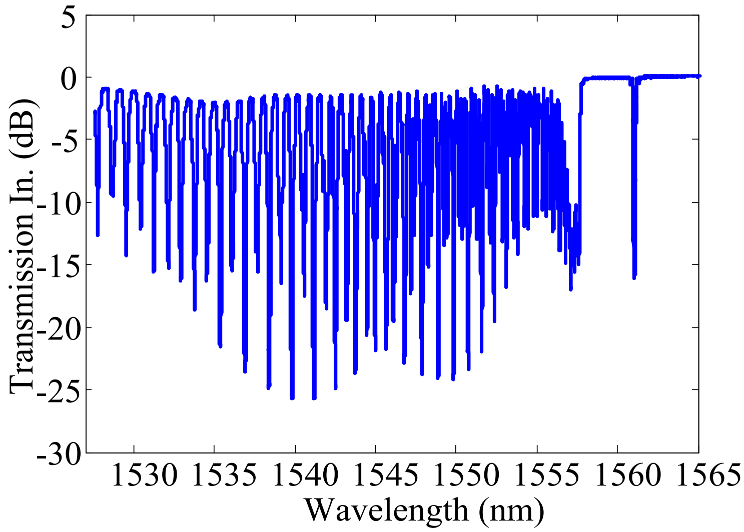

Fig. 3.11. The transmission spectrum of a TFBG with a tilt angle of 6°, and a Bragg wavelength of 1560 nm.

A TFBG with a tilt angle of 6° and Bragg wavelength of 1560 nm is fabricated by using an excimer laser with a uniform phase mask. The tilt angle is introduced by a focal lens. The fiber used to fabricate the LCFBG is a photosensitive Er/Yb co-doped fiber (EY 305, Coractive) which is hydrogen loaded for two weeks to further increase the photosensitivity. Fig. 3.11 shows the transmission spectrum of the fabricated TFBG. The TFBGs used in this research work are fabricated in the Prof. Jacques Albert's lab in the Carleton University. The TFBG is pumped by a 980-nm LD; by increasing the injection current to the LD, the pump power is increased. Fig. 3.12 shows the magnitude and group delay responses of one of the cladding-mode resonances of the fabricated TFBG at the wavelength of 1540.32 nm, which is measured using an optical vector analyzer (LUNA TECHNOLOGIES, Optical vector analyzer CT_e). By pumping the TFBG with a 980-nm LD, the resonance wavelength is shifted to a longer wavelength and the group delay response is shifted correspondingly. As can be seen from Fig. 3.12(b), at the wavelength of 1540.36 nm a tunable group delay from a time advance of -38 ps (fast light) to a time delay of 18 ps (slow light) can be achieved by changing the pumping power from 0 to 150 mW. The FWHM bandwidth of the resonance shown in Fig. 3.12(a) is about 22 GHz. Thus, the time-bandwidth product is 1.23.

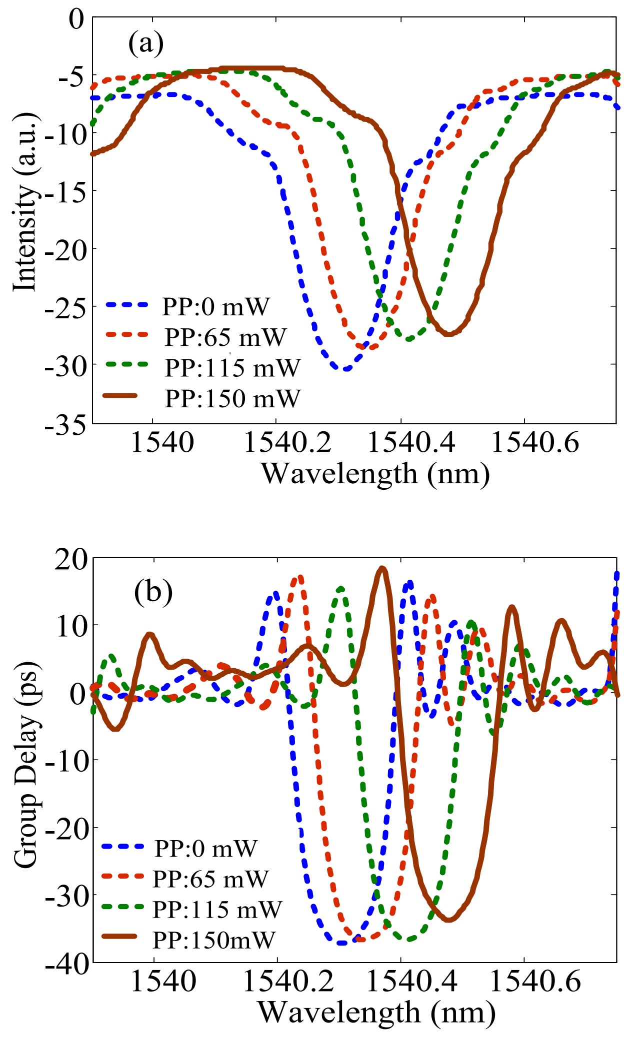

Fig. 3.12. (a) The magnitude response and (b) the group delay response of one channel of a TFBG with a tilt angle of 6^{o}, and a Bragg wavelength of 1560 nm. PP: pumping power.

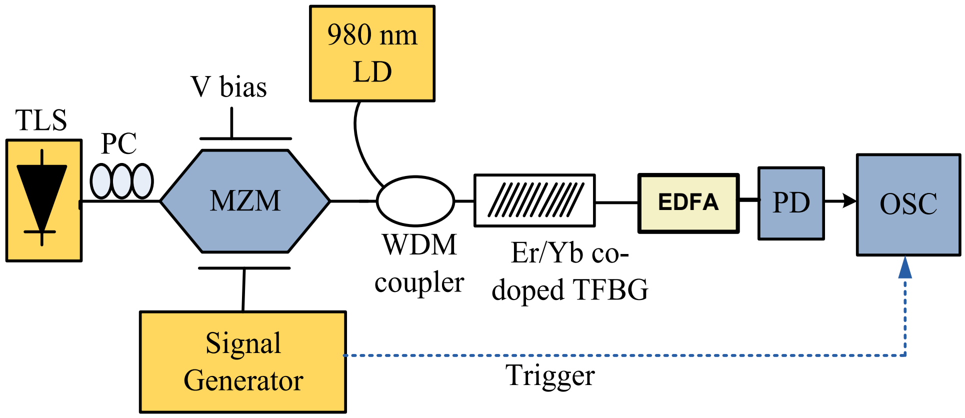

Fig. 3.13. Experimental setup. TLS: tunable laser source, LD: laser diode, MZM: Mach–Zehnder modulator, PC: polarization controller, WDM: 980/1550 nm wavelength division multiplexer, PD: photo-detector, OSC: oscilloscope, EDFA: erbium doped fiber amplifier.

The proposed technique for achieving tunable slow and fast light is experimentally studied. The experimental setup is shown in Fig. 3.13. A lightwave from a tunable laser source (TLS) is sent to a 20 GHz Mach-Zehnder modulator (MZM). A Gaussian pulse with an FWHM bandwidth of 13.5 GHz generated by a signal generator [Agilent N4901B Serial Bit Error Rate Tester (BERT)] is applied to the MZM via the RF port to modulate the lightwave. The modulated lightwave is sent to the fabricated TFBG through a wavelength division multiplexing (WDM) coupler. The TFBG is fabricated by using an excimer laser with a uniform phase mask. The TFBG is pumped by a 980-nm LD. The time-delayed or advanced light signal transmitted through the TFBG is sent to an EDFA to compensate the loss caused by the resonance notch and is detected by a 53-GHz photodetector and the electrical waveform is observed by a sampling oscilloscope (Agilent 86100C). In order to have a reference to measure the time delay or advance of the detected signal, the wavelength of the TLS is first tuned to be out of the resonance spectrum, thus the light signal would not experience a time delay or advance caused by the mode resonance. Then, the wavelength of the lightwave is tuned to 1540.36 nm to be inside one of the cladding mode resonances (as shown in Fig. 3.12, one cladding mode resonance is located at the wavelength of 1540.32 nm). As can be seen in Fig. 3.14, by pumping the TFBG with a power of 60 mW, a time advance of -38 ps is achieved, and when the pumping power is tuned to 140 mW, a time delay of +18 ps is achieved. By continuously tuning the pump power from 60 mW to 140 mW, a continuous tuning from a fast to slow light with a tunable range of 56 ps is achieved. Since the bandwidth of the input pulse is 13.5 GHz, the tunable time-bandwidth product in this experiment is 0.75. To evaluate the performance of the proposed technique, a simulation is performed, in which the time delayed and advanced signals by using the TFBG with a pumping power at 60 mW and 140 mW are calculated. The simulated (dashed) results are shown in Fig. 3.15. The experimental results are also shown for comparison. As can be seen, a good agreement is reached between the simulated and experimentally generated waveforms. A slight mismatch between the simulated and the experimentally generated waveforms is observed, which is caused by the non-ideal Gaussian pulse generated by the BERT.

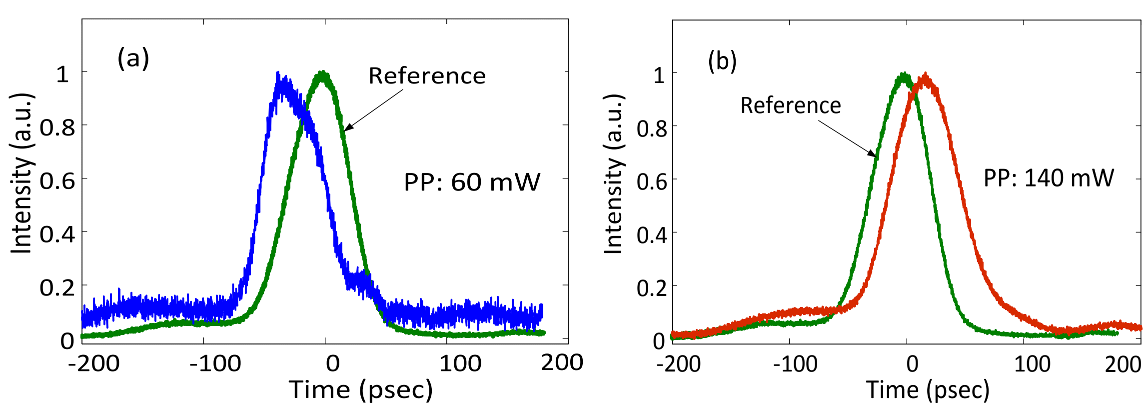

Fig. 3.14. The detected signals at different pump power levels of (a) 60 mW, and (b) 140 mW. PP: pumping power.

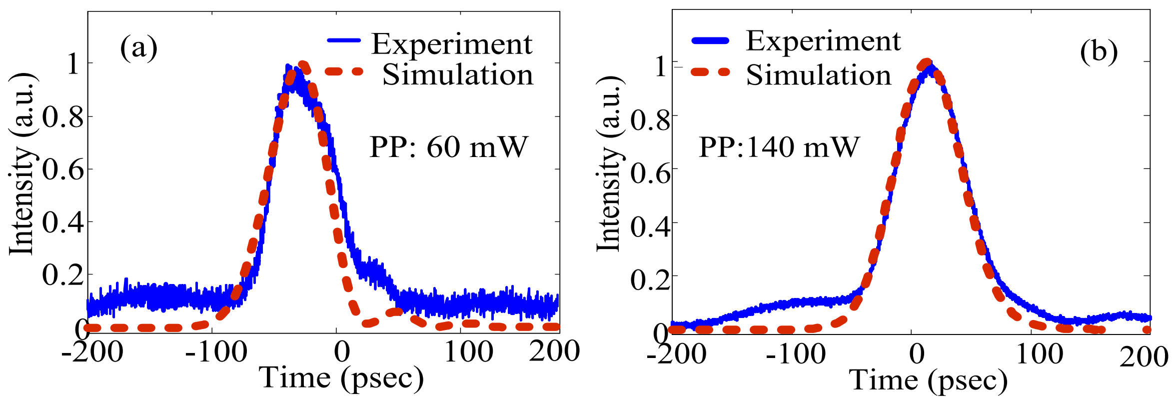

Fig. 3.15. The simulated (dashed) and experimentally generated (solid) signals with a pumping power of (a) 60 mW and (b) 140 mW. PP: pumping power.

CHAPTER 4 APPLICATIONS OF FBG-BASED SLOW AND FAST LIGHT IN MICROWAVE PHOTONICS

4.1. Continuously tunable microwave frequency multiplication

In this section, we propose and experimentally demonstrate an approach to achieving continuously tunable frequency multiplication using the slow and fast light effects in a LCFBG written in an Er/Yb co-doped fiber in an unbalanced temporal pulse shaping (UTPS) system. In Section 3.2, it was demonstrated that as a result of slow and fast light effects by pumping a LCFBG written in an Er/Yb co-doped fiber its dispersion is changed. This tunable dispersion can be used in an UTPS system to obtain all-optical and continuous tuning of the microwave frequency multiplication factor. In [35], also a continuously tunable frequency multiplication was achieved by using an UTPS system. In this approach, two lengths of DCF and SMF were used as the dispersive elements of the UTPS system, and the tunability of the multiplication was achieved by changing the length of the fibers. The key significance of our approach compared with the one in [35] is that the microwave frequency can be continuously tunable. In addition, the Er/Yb co-doped LCFBG has a much shorter length of a few centimeters, which makes the system more compact with better stability.

An UTPS system is different from a typical TPS system where the two dispersive elements have complementary dispersions. Here in the UTPS system, the Er/Yb co-doped LCFBGs are designed to have opposite dispersion, but with different magnitudes. Thus, the entire system can be considered as a typical TPS system with two dispersive elements having complementary dispersion for real-time Fourier transformation (FT) [180] followed by a residual dispersive element to achieve a second real-time FT. The operation of the system is first discussed and is then verified by an experiment. Continuously tunable microwave frequency multiplication with a multiplication factor from 5.14 to 11.9 is experimentally demonstrated. The impact of the ripples in the magnitude and group delay responses of the LCFBGs on the performance of the microwave generation is also studied.

The proposed UTPS system for microwave generation with continuously tunable frequency is shown in Fig. 4.1. The system consists of a mode lock laser (MLL), two LCFBGs written in Er/Yb co-doped fibers pumped by two 980-nm laser diodes (LDs), two optical circulators, a Mach-Zehnder modulator (MZM), and a high-speed photodetector (PD). A microwave drive signal generated by an arbitrary waveform generator (AWG) is applied to the MZM. The generated microwave signal is monitored by a sampling oscilloscope.

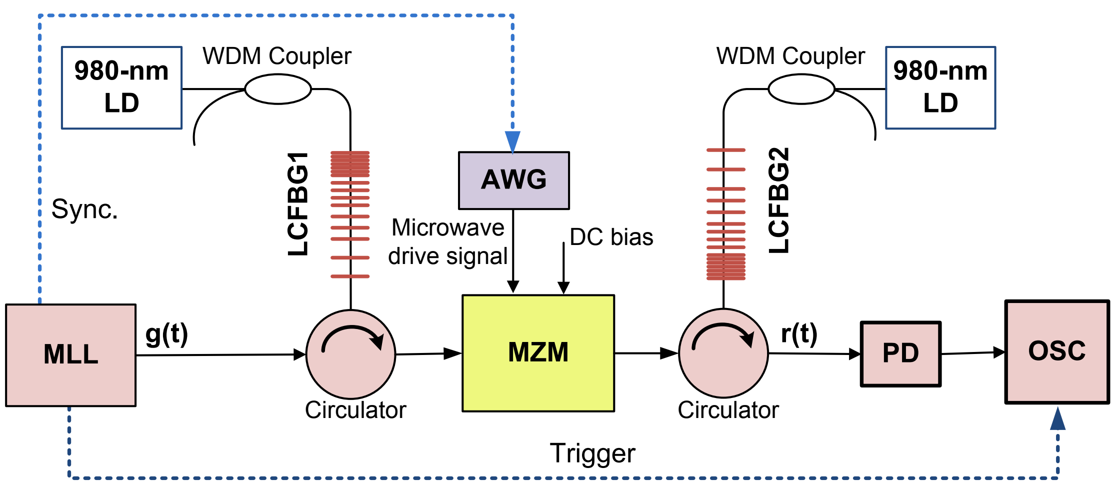

Fig. 4.1. The UTPS system proposed to achieve continuously tunable frequency multiplication. The LCFBGs are optically pumped to change the dispersion.

A LCFBG can be modeled as a linear time-invariant (LTI) system with a transfer function given by

$$H_i(\omega) = \exp\left(-j\frac{\ddot{\Phi}_i \cdot \omega^2}{2}\right), (i = 1, 2) \tag{4-1}$$

where $\ddot{\Phi}_i$ (ps^2/rad) is the dispersion of the ith LCFBG, and $j = \sqrt{-1}$. In the proposed UTPS system the values of dispersion of the two LCFBGs should satisfy $\ddot{\Phi}_1\ddot{\Phi}_2 < 0$, and $|\ddot{\Phi}_1| \neq |\ddot{\Phi}_2|$. In fact, the UTPS system can be seen as a typical balanced TPS system with two complementary dispersive elements followed by a third dispersive element with a residual dispersion of $\Delta\ddot{\Phi} = \ddot{\Phi}_1 - \ddot{\Phi}_2$. The transfer function of the residual dispersive element is given by $H_\Delta(\omega) = \exp(-j\frac{\Delta\ddot{\Phi} \cdot \omega^2}{2})$. It is known that a double-sideband modulated signal will experience power penalty if the signal is traveling in a dispersive element. To eliminate the dispersion-induced power penalty [32], in our proposed system the MZM is dc-biased at the minimum transmission point to suppress the optical carrier. Under the small-signal-modulation condition, the intensity modulation function of the MZM can be written as $e_{IM}(t) = 2 \times J_1(\beta)\cos(\omega_m t)$, where $J_1(\beta)$ is the first-order Bessel function of the first kind, β is the phase modulation index, and ω_m is the angular frequency of the microwave drive signal applied to the MZM [181]. If the complementary dispersion in the typical TPS system is large enough, i.e. $\ddot{\Phi}_1 >> \tau_0^2 / 2\pi$, where τ_0 is the pulse width of the input optical pulse $g(t)$ to LCFBG1, the signal at the output of the typical TPS system is given by [182]

$$s(t) \propto g(t) * E_{IM}(\omega)\big|_{\omega = t/\ddot{\Phi}_1} = J_1(\beta)[g(t - T_1) + g(t + T_1)], \tag{4-2}$$

where $E_{IM}(\omega)$ is the Fourier transform of $e_{IM}(t)$, * denotes the convolution operation, and $T_1 = \omega_m \ddot{\Phi}_1$. Based on (4-2), it can be seen that two time-delayed replicas of the input pulse are generated at the output of the typical TPS system. By propagating the signal $s(t)$ through the residual dispersive element, a frequency multiplied microwave signal is generated. Assume that the dispersion of the residual dispersive element satisfies the condition given by $\Delta\ddot{\Phi} \geq T_1^2 / 2(2\pi)$, then the signal at the output of the residual dispersive element is Fourier-transformed version of $s(t)$, which is given by

$$\begin{aligned} r(t) &\approx S(\omega)\big|_{\omega = t/\Delta\ddot{\Phi}} \\ &= J_1(\beta) G\left(\frac{t}{\Delta\ddot{\Phi}}\right) \cos\left(\frac{T_1}{\Delta\ddot{\Phi}} t\right) \end{aligned} \tag{4-3}$$

where $G(\omega)$ is the Fourier transform of the input pulse $g(t)$. The signal at the output of the PD is

$$I(t) \propto |r(t)|^2 \propto J_1^2(\beta) G^2\left(\frac{t}{\Delta\ddot{\Phi}}\right)\left[1 + \cos\left(\frac{2T_1}{\Delta\ddot{\Phi}} t\right)\right]. \tag{4-4}$$

As can be seen from (4-4), a microwave signal with a frequency of $\omega_{RF} = \left|\frac{2T_1}{\Delta\ddot{\Phi}}\right| = \omega_m \left(\frac{2\ddot{\Phi}_1}{\Delta\ddot{\Phi}}\right)$ is generated at the output of the UTPS system. Thus, the frequency multiplication factor of the proposed system is equal to

$$F = \frac{\omega_{RF}}{\omega_m} = 2\left(\frac{\ddot{\Phi}_1}{\Delta\ddot{\Phi}}\right). \tag{4-5}$$

From (4-5), we can conclude that frequency multiplication factor of the system is determined by the dispersion of the first LCFBG ($\ddot{\Phi}_1$) and the residual dispersion ($\Delta\ddot{\Phi}$).

By optically pumping a LCFBG that is written in an Er/Yb co-doped fiber, the refractive index of the fiber would change. Mathematically, the change of the refractive index as a function of the power change along the fiber is given by,

$$\Delta n = \frac{\partial n}{\partial T} \times \frac{-\eta}{2\pi bh} \times \frac{dP_P(z)}{dz} \tag{4-6}$$

where n is the refractive index and T is the temperature, $\frac{\partial n}{\partial T}$ is the index temperature coefficient, b is the outer radius of the fiber, h is the heat transfer coefficient between the fiber and the surrounding medium, η is the fraction of the absorbed pumping power turned to heat, and $P_P(z)$ is the pump distribution along the fiber. It can be understood from (4-6) that the refractive index of the fiber would change along the fiber depending on the pumping power distribution which results in dispersion changing ($dn/d\omega$). If the pumping power has a high power decay rate such that the power is zero at the other end, the refractive index near the pumping port is changed while the refractive index at the other port is kept unchanged. If the refractive index along the fiber is changed due to the non-uniform distribution of the pumping power, the dispersion profile of the LCFBG is changed. For example, if a LCFBG is pumped from the long-period end, the second reflection edge of the LCFBG is shifted to a longer wavelength, and the total reflection bandwidth is increased. On the other hand, if a LCFBG is pumped from the short-period end, the first reflection edge is shifted to a longer wavelength and the total reflection bandwidth is decreased. By considering the relationship between the dispersion and the group-delay slope given by

$$\ddot{\Phi} = \frac{-\lambda_0^2}{2\pi c} \times \frac{d\tau}{d\lambda} \tag{4-7}$$

where λ_0 is the central wavelength of the reflection spectrum, c is the speed of light in vacuum, and $\frac{d\tau}{d\lambda}$ is the group-delay slope in the reflection bandwidth, we can see that by increasing the reflection bandwidth, the group-delay slope is reduced, thus leading to a decreased dispersion.

The proposed technique based on the setup shown in Fig. 4.1 is experimentally demonstrated. Two LCFBGs are fabricated and are connected before and after the MZM. In the experiment, since only a 980-nm pump source is available, only one LCFBG is written in an Er/Yb co-doped fiber and is optically pumped, which is LCFBG2, and LCFBG1 is written in a regular photosensitive fiber and is not pumped. Thus, the frequency tuning is done by pumping LCFBG2 only. A 3 GHz sinusoidal signal generated by the AWG is applied to the MZM via the RF port. The temporally stretched optical pulse from LCFBG1 is then modulated by the 3 GHz sinusoidal microwave signal at the MZM. To avoid dispersion-induced power penalty, the MZM is biased at the minimum transmission point. The modulated signal is then sent to LCFBG2, and the reflected optical signal is detected by a high-speed PD, and the electrical waveform is monitored by a sampling oscilloscope. Note that the MLL, the AWG and the sampling oscilloscope are synchronized. The bandwidth of LCFBG1 is 0.8 nm and its value of dispersion is $\ddot{\Phi}_1 = 1831.21$ ps^2/rad. The bandwidth of LCFBG2 is 0.5 nm and its value of dispersion is $\ddot{\Phi}_2 = 1932.32$ ps^2/rad when it is not pumped.

An ultra-short Gaussian pulse with an FWHM bandwidth of 8 nm and central frequency of 1558 nm is generated by the MLL and is sent to LCFBG1 via the first optical circulator. After reflecting from LCFBG1, the optical pulse is temporally stretched and the time duration of the pulse is increased to $\Delta t = \Delta\omega \times \ddot{\Phi}_1 = 1150$ ps, where $\Delta\omega$ is the 3-dB bandwidth of LCFBG1 which is 0.8 nm or equivalently 100 GHz. The temporally stretched pulse is modulated at the MZM by the 3 GHz microwave drive signal. Since the MZM is biased at the minimum transmission point, the output signal from the MZM is frequency doubled. Considering the duration of the input optical pulse to the MZM (1150 ps) and the frequency doubling operation at the MZM, the signal at the output of the MZM should contain 7 microwave cycles. Fig. 4.2 shows the experimentally generated signal with photodetection from the output of the MZM, observed by the sampling oscilloscope. As can be seen, the time duration of the modulated signal is 1150 ps and the number of microwave cycles is 7.

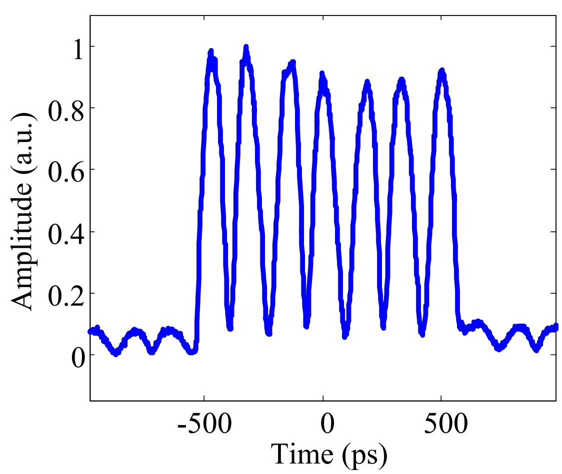

Fig. 4.2. The modulated signal at the output of the MZM observed by the sampling oscilloscope.

The optical pulse at the output of the MZM is then sent to LCFBG2 via the second optical circulator. LCFBG2 is written in an Er/Yb co-doped fiber and is pumped by a 980-nm LD from the long-period end. Fig. 4.3(a) and (b) shows the reflection spectra and the group delay responses of the LCFBG2 pumped by the 980-nm LD at different pumping powers. Since LCFBG2 is pumped from the long-period end, by increasing the pump power, the reflection bandwidth is increased, the group-delay slope is decreased, and thus based on (4-7) the dispersion is decreased. On the other hand, if LCFBG2 is pumped from the short-period end, the dispersion would be increased by increasing the pumping power. By continuously tuning the pumping power, the dispersion of LCFBG2 is changed as a result of slow and fast light effects. Therefore, the residual dispersion ($\Delta\ddot{\Phi}$) is changed and based on (4-5) the frequency multiplication factor is changed continuously. In the experiment, since the dispersion of LCFBG1 is constant, and the dispersion of LCFBG2 is decreased, the residual dispersion is increased and consequently the multiplication factor F is decreased. In the demonstration, by increasing the pumping power from 29 to 139 mW, the dispersion of the LCFBG2 is reduced from 1545.22 to 1207.6 ps^2/rad, as shown in Fig. 4.3(b), and consequently the multiplication factor is reduced from 12.8 to 5.88. Note that the bandwidth of LCFBG2 is changed when is pumped, as can be seen from Fig. 4.3(a), the bandwidth is increased from 0.5 to 0.78 nm when the pumping power is increased from 0 to 139 mW. The number of microwave cycles within the pulse is determined by the overall bandwidths of LCFBG1 and LCFBG2. If the overall bandwidth is 0.5 nm, the number of cycles in the modulated signal would be 5. Note that the bandwidth of LCFBG1 is 0.8 nm and the effective bandwidth of LCFBG2 is increased if pumped, the number of cycles in the modulated signal will also be increased.

Fig. 4.4 shows the experimentally generated microwave waveforms by pumping LCFBG2 at different pumping power levels. In the experiment, the pumping power is increased from 29 to 139 mW, the microwave frequency is reduced from 35.71 to 15.43 GHz, and the multiplication factor F is reduced from 11.9 to 5.14. Note that the number of microwave cycles in the pulse is increased because of the increase of LCFBG2 bandwidth as a result of pumping.

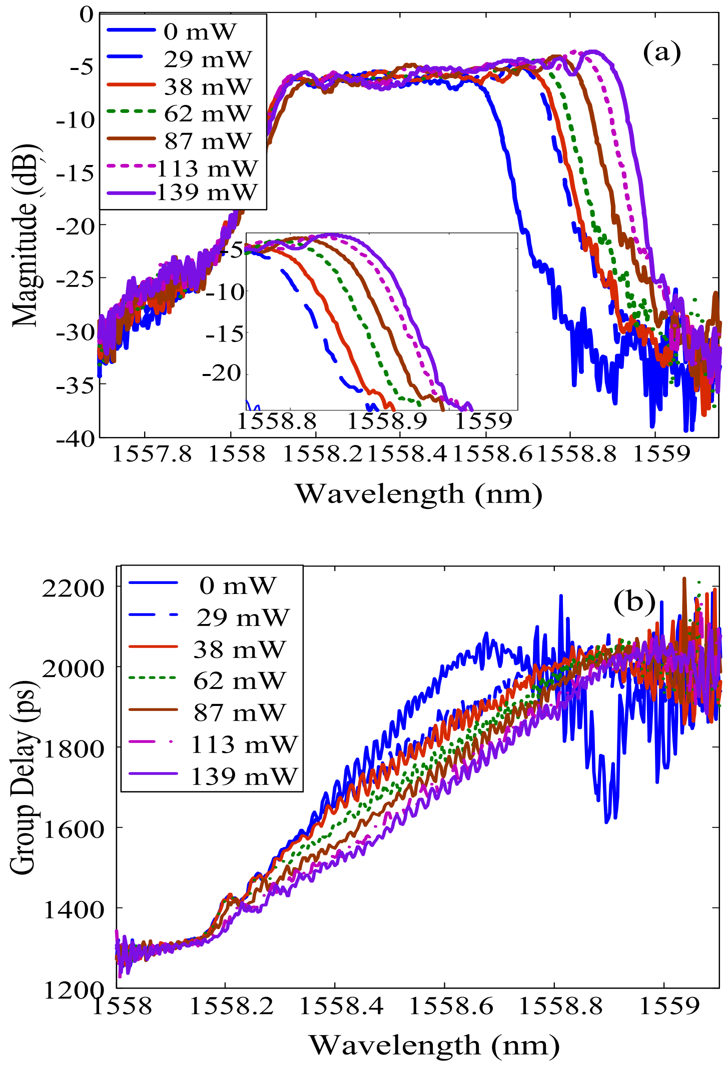

Fig. 4.3. (a) The magnitude and (b) the group delay responses of the Er/Yb co-doped LCFBG pumped with a 980-nm LD with different powers. The inset gives a zoom-in view of the magnitude response near the long reflection edge.

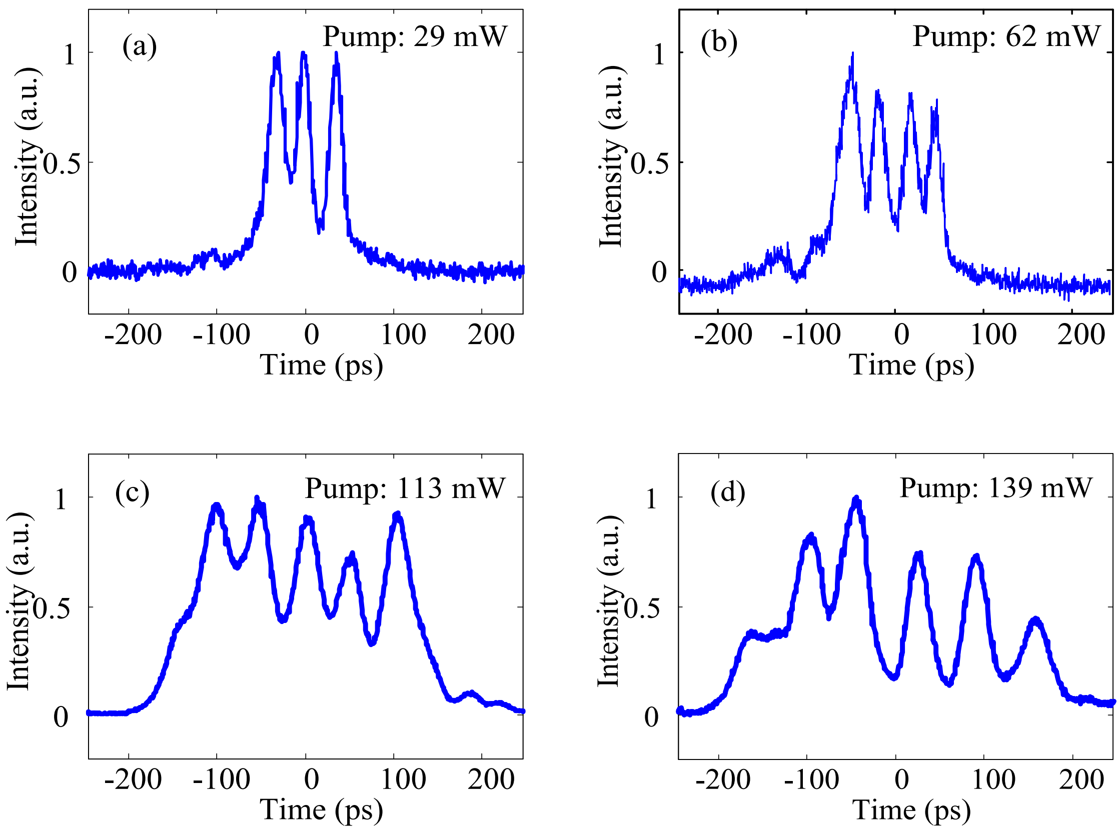

Fig. 4.4. Generated microwave waveforms when LCFBG2 is pumped with pumping powers of 29, 62, 113, and 139 mW with the corresponding frequencies of (a) 35.71, (b) 28.57, (d) 19.23, and (e) 15.43 GHz.

To avoid the change of the pulse width, we stretch LCFBG2 to make its long reflection edge aligned with the long reflection edge of LCFBG1. Then, when it is pumped, the overall bandwidth is fixed at 0.5 nm with no change. The generated microwave waveforms are shown in Fig. 4.5. By increasing the pumping power from 38 to 139 mW, the generated microwave frequency is decreased from 35 to 15.38 GHz, and the multiplication factor F is reduced from 11.66 to 5.13. A summary is provided in Table IV-I; both theoretical and experimental values are provided.

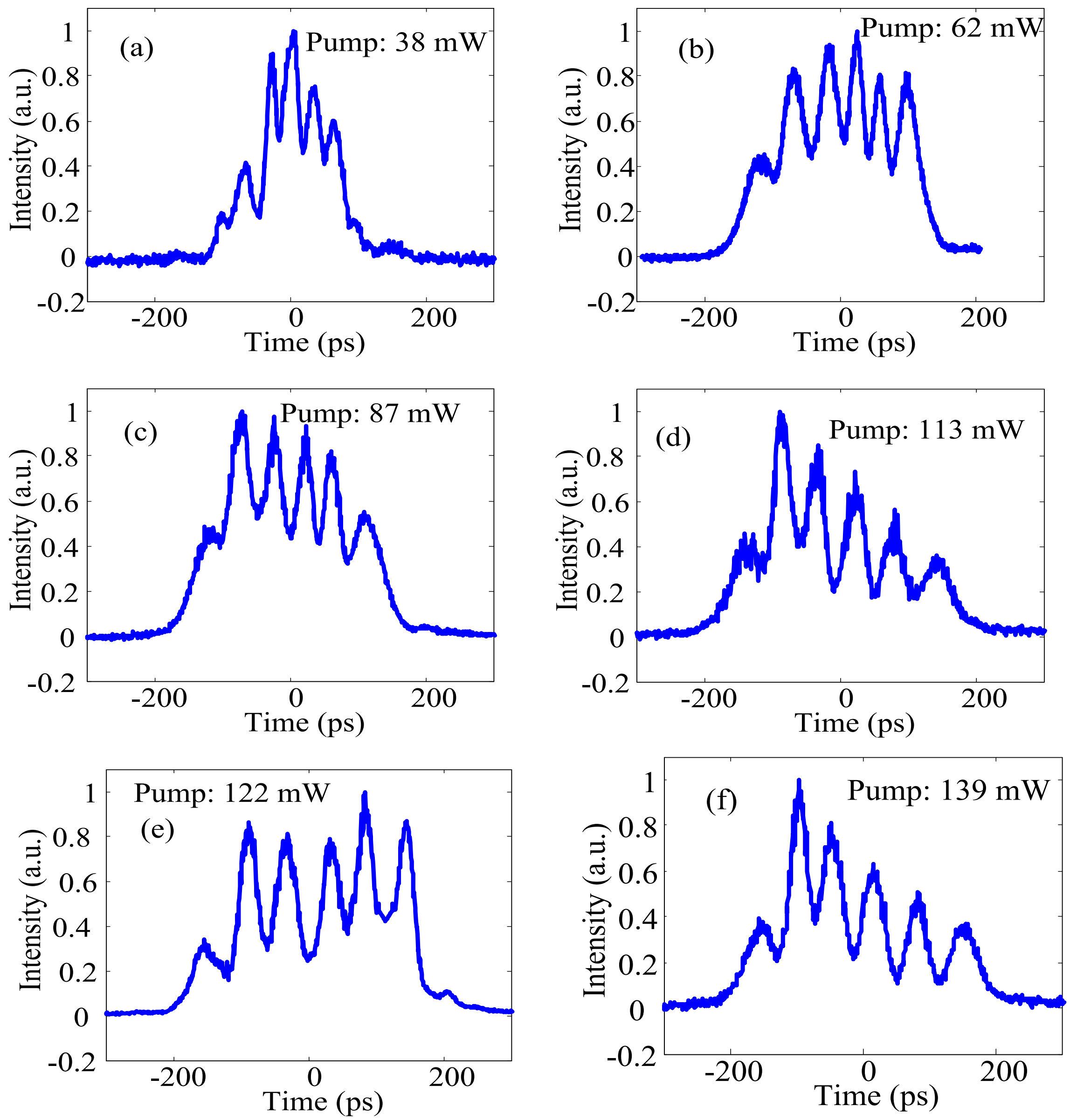

Fig. 4.5. Generated microwave waveforms when LCFBG2 is pumped with pumping powers of 38, 62, 87, 113, 122, and 139 mW with the corresponding frequencies of (a) 35, (b) 27.27, (c) 22.22, (d) 18.51, (e) 17.24, and (f) 15.38. GHz.

The frequency tunable range in the proposed system depends on the dispersion of LCFBG1 and LCFBG2, which can be increased if four pumping LDs are employed. In this case, two pumping LDs are employed to pump one LCFBG from the two ends. For example, if the dispersions of LCFBG1 and LCFBG2 are 2101.91 and 1681.53 ps^2/rad, and if LCFBG2 is pumped from the two ends, its dispersion can be tuned from 1285.87 to 2185.98 ps^2/rad, and consequently the multiplication factor can be tuned continuously from 5 to 44.

Table 4.1. A summary of the key parameters for the theoretical waveform and the waveforms generated experimentally.

Pumping power	$\ddot{\Phi}$ (ps^2/rad)	F Experimental / Theoretical	f_{RF} (GHz) Experimental / Theoretical
38 mW	1520.44	11.66/11.78	35.00/35.34
62 mW	1438.24	9.06/9.32	27.27/27.96
87 mW	1366.19	7.40/7.78	22.22/23.34
113 mW	1266.02	6.17/6.48	18.51/19.44
139 mW	1177.20	5.13/5.60	15.38/16.80

To evaluate how the generated waveforms are close to the theoretical waveforms given by (4-4), a simulation is performed, to compare the simulated waveforms with the waveforms generated in the experiment. Fig. 4.6 shows the simulated and experimentally generated microwave waveforms for LCFBG2 being pumped at two power levels of 62 and 113 mW. In the simulation, the reflection spectra of the two LCFBGs are the actual spectra of the LCFBGs used in the experiment. As can be seen, the simulated and the experimentally generated waveforms match quite well. The small discrepancy between the simulated and the experimentally generated waveforms is mainly resulted from the limited bandwidths of the MZM and the PD.

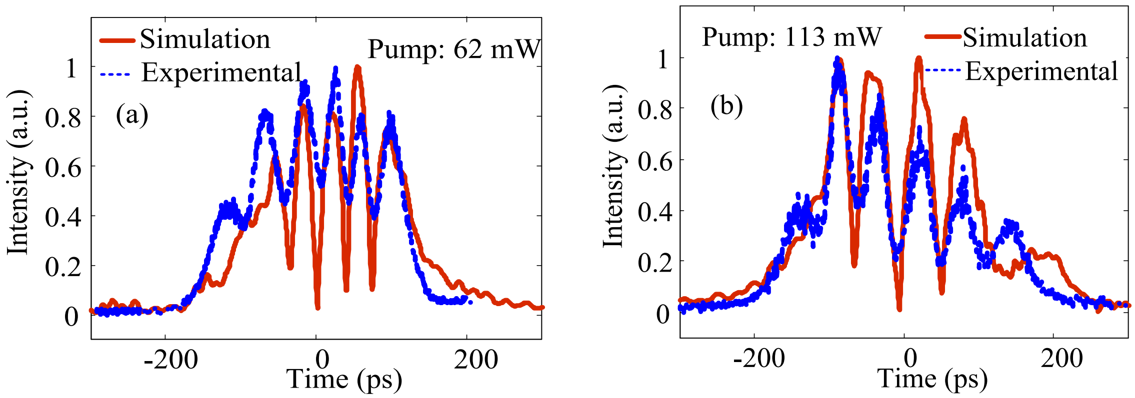

Fig. 4.6. The comparison of the waveforms generated experimentally and the waveforms obtained based on simulation for LCFBG2 being pumped at (a) 62 and (b) 113 mW.

The key components in our proposed system for microwave waveform generation are the two LCFBGs. An ideal LCFBG would exhibit a constant magnitude response and a linear group delay response with no ripples. In a practical LCFBG, however, ripples in the magnitude and group delay responses would always exist, which may affect the performance for microwave waveform generation. To evaluate the impact due to the magnitude and group delay ripples on the generated waveforms, a second simulation is performed. Since the period of the ripples depends on the phase mask used for writing the LCFBGs, for a specific phase mask the period of the ripples is constant, but the amplitudes of the magnitude and group delay ripples may change depending on the writing technique. A usual way to reduce the ripples is to apply apodization and back scanning during the fabrication process. In this simulation, the period of the ripples is considered constant and the amplitudes of the magnitude and group delay ripples are set at different values.

First, we assume the LCFBGs have an ideal group delay response and the ripples only exist in the magnitude response. Fig 4.7(a) and (b) shows the simulated waveforms for the magnitude ripples having a period of 60 pm and an amplitude of 0.4 dB and 0.8 dB, respectively. As can be seen the ripples' magnitude of the LCFBGs would cause distortions to the generated waveforms, and the distortions are increased when the magnitude of the ripples is increased.

Then, the impact of group delay ripples on the generated waveforms is studied. In the simulation, a constant magnitude response is considered. Again, the period of the ripples is set at a fixed value, which is 20 pm. Fig. 4.8(a) and (b) shows waveforms for the group delay ripples with amplitude of 30 and 60 ps, respectively. As can be seen the group delay ripples would also cause distortions to the generated waveforms, and the distortions become stronger when the amplitude of the ripples is increased. In reality, we have both ripples in the magnitude and group delay (KK relations) which makes the situation worse. To reduce both the magnitude and group delay ripples, we may apply apodization during the fabrication of the LCFBGs.

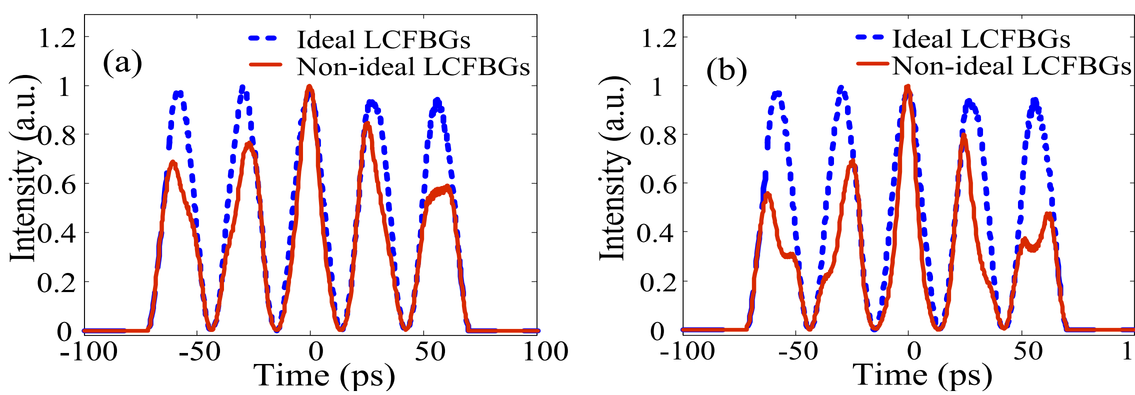

Fig. 4.7. Simulation of the generated microwave waveforms by ideal LCFBGs (dashed lines) and by non-ideal LCFBGs with magnitude ripples only (solid lines). The period of the magnitude ripples is set at 60 pm and the amplitude of the ripples is (a) 0.4 dB and (b) 0.8 dB.

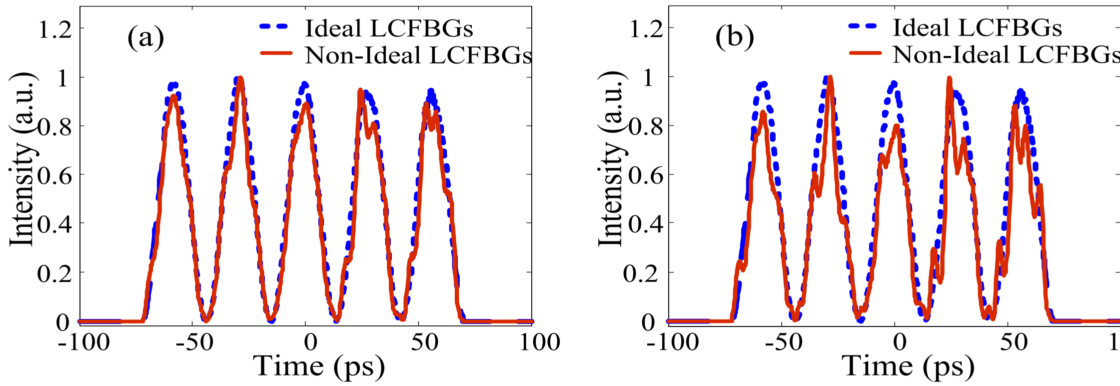

Fig. 4.8. Simulation of the generated microwave waveforms by ideal LCFBGs (dashed lines) and by non-ideal LCFBGs with group delay ripples only. The period of the group delay ripples is set to 20 pm and the amplitude of the ripples is (a) 30 ps and (b) 60 ps.

In conclusion, a novel method for achieving tunable microwave frequency multiplication based on an UTPS system using two LCFBGs written in Er/Yb co-doped fibers was proposed and demonstrated. The key significance of the proposed technique is the tuning of the frequency multiplication factor through slow and fast light effects in an optically pumped LCFBG. A theoretical analysis was provided which was verified by an experiment. Microwave waveform generation with a tunable frequency multiplication factor of 5.13 to 11.9 was experimentally demonstrated. The impact of the ripples of the LCFBG on the performance of the system was also studied. The results showed that both the magnitude and group delay ripples would lead to distortions to the generated waveforms. A solution to reduce the ripples is to apply apodization. The proposed technique has potential applications in radar and microwave tomography where high frequency and frequency-tunable microwave waveforms are needed.

4.2. Continuously tunable chirped microwave waveform generation

In this section, we propose a new technique to generate continuously tunable chirped microwave waveforms using laser sources with fixed wavelengths. The entire system is a photonic microwave delay-line filter with nonuniformly spaced taps. When an ultra-short pulse is applied to the input of the photonic microwave delay-line filter, a pulse burst with nonuniform temporal spacing is generated. The nonuniform time delays are achieved using a TFBG, which is written in an Er/Yb co-doped fiber. Due to the strong absorption, the refractive index of the Er/Yb co-doped fiber is changed when the TFBG is optically pumped. In the proposed system, the wavelengths of the laser sources are located at the different cladding-mode resonance notches of the TFBG, and the tuning of the time delays is realized by optically pumping the TFBG. Thus, simple but fast tuning is ensured. An experiment is performed. A chirped microwave pulse with a tunable chirp rate from 1.8 to 7 GHz/ns is experimentally demonstrated.

A chirped microwave waveform can be generated using a photonic microwave delay-line filter with nonuniformly spaced taps [45]. When an ultra-short pulse is applied to the input of the photonic microwave delay-line filter, at the output a pulse burst with a temporal spacing depending on the time delays is obtained. By applying the pulse burst to a photodetector (PD), due to the limited bandwidth of the PD a chirped microwave waveform is generated [183]. The operation of a photonic microwave delay-line filter for chirped microwave waveform generation is shown in Fig. 4.9.

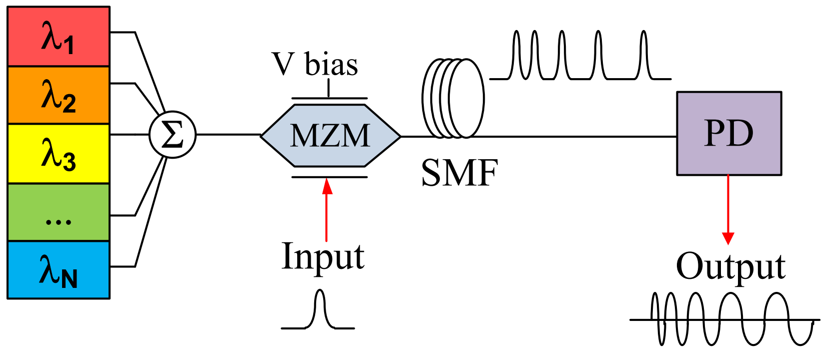

Fig. 4.9. Chirped microwave waveform generation using a nonuniformly spaced photonic microwave delay-line filter.

The nonuniform time delays can be generated by incorporating a TFBG into the photonic microwave delay-line filter. There are multiple resonances at the transmission spectrum of a TFBG. The resonance wavelengths are given by (3-21) and (3-22). Based on KK relations, a change in the amplitude results in a change in the phase ($d\varphi / d\omega$), and consequently a change in the group-delay. Thus, within the bandwidth of each resonance, a tunable time delay can be achieved for slightly tuning the wavelength. Since the coupling coefficient is different for different resonances in a TFBG, the range and rate of time tunability are different at different resonances. To achieve tunable time delays, the TFBG is written in an Er/Yb co-doped fiber and is optically pumped. Thanks to the high absorption of an Er/Yb co-doped fiber, by pumping the TFBG with a 980-nm LD having a tunable pumping power, the refractive index along the TFBG is changed which leads to the shift of the resonance wavelengths and thus the change of the time delays. By locating the wavelengths at the cladding-mode resonance notches, nonuniform time delays are achieved, which lead to the generation of a chirped microwave waveform.

A TFBG with the tilt angle of 6^o is fabricated using an excimer laser with a uniform phase mask. The tilt angle is introduced by using a focal lens. The fiber used to fabricate the TFBG is a photosensitive Er/Yb co-doped fiber (EY 305, Coractive) which is hydrogen loaded for two weeks to further increase the photosensitivity. Fig. 3.11 shows the transmission spectrum of the fabricated TFBG. Fig. 3.12 shows the magnitude and group delay responses of one of the cladding-mode resonances at 1540.32 nm, which is measured using an optical vector analyzer (LUNA Optical vector analyzer CT_e). By pumping the TFBG, the resonance wavelength is shifted to a longer wavelength and the group delay response is also shifted accordingly. As can be seen in Fig. 3.11, the coupling coefficients of the resonances within the wavelength range of 1530-1540 nm are linearly changing, and consequently the time delays achieved at different resonances are also linearly changing which provides linear chirping.

The proposed technique for generating a tunable chirped microwave waveform is experimentally studied. The experimental setup is shown in Fig. 4.10. Four lightwaves from four tunable laser sources are sent to a 20 GHz Mach-Zehnder modulator (MZM). A Gaussian pulse with an FWHM bandwidth of 6.7 GHz generated by a signal generator [Agilent N4901B Serial Bit Error Rate Tester (BERT)] is applied to the MZM via the RF port to modulate the lightwaves. The modulated lightwaves are sent to a length of SMF of a length of 4.3 km with a total dispersion of 74 ps/nm to introduce a constant time delay between adjacent channels and then are sent to the fabricated TFBG to introduce tunable time delays. A pulse burst with the time delays determined by the length of the SMF and the TFBG is generated at the output of the TFBG, which is then applied to a 53 GHz photodetector. The generated chirped waveform is observed by a sampling oscilloscope (Agilent 86100C).

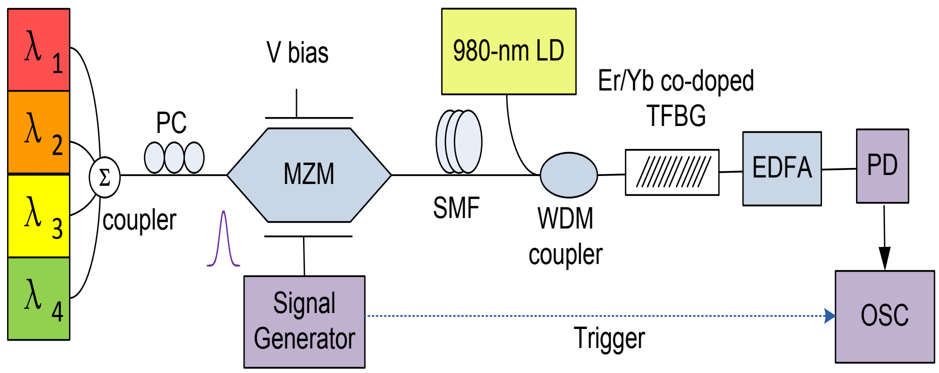

Fig. 4.10. Experimental setup. LD: laser diode, MZM: Mach–Zehnder modulator, PC: polarization controller, WDM: 980/1550 nm wavelength division multiplexer, PD: photo-detector, OSC: oscilloscope.

The generated chirped microwave waveforms are shown in Fig. 4.11. By increasing the pump power (PP), a chirped microwave waveform with an increasing chirp rate is generated which are shown in Fig. 4.11(a-c). The microwave frequency versus time for the chirped waveform with three different chirp rates is shown in Fig. 4.12. As can be seen by increasing the pump power from 0 to 100 mW, the chirp rate is increased from 1.8 to 7 GHz/ns. The experimentally generated waveforms are compared with the simulated ideally chirped waveforms, a good agreement is achieved. The root mean square error ($RMSE = \sqrt{\frac{\sum_{i=1}^{n}(x_i - y_i)^2}{n}}$) is calculated to be 14% between the waveforms shown in Fig. 4.11(c), which is the largest error for the three generated waveforms. The slight difference in amplitude between the experimentally generated and the simulated waveforms is due to the non-flat frequency response of the MZM and the PD, and the non-uniform powers of the tunable laser sources.

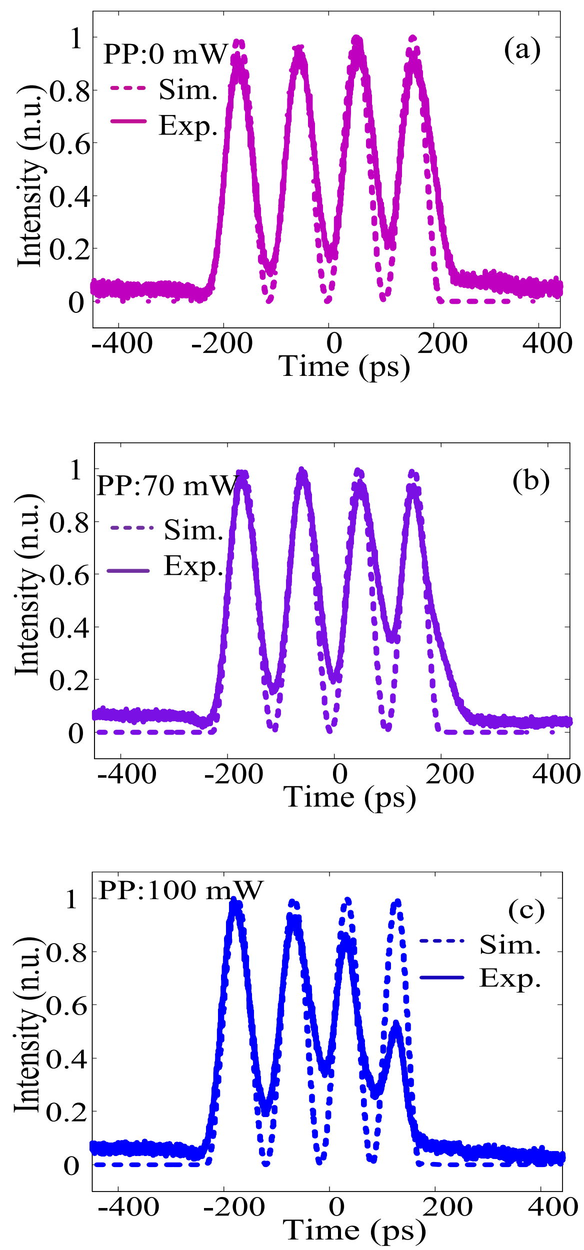

Fig. 4.11. The experimentally generated (solid) and simulated (dashed) chirped microwave waveforms with a pumping power of (a) 0 mW, (b) 70 mW, and (c) 100 mW.

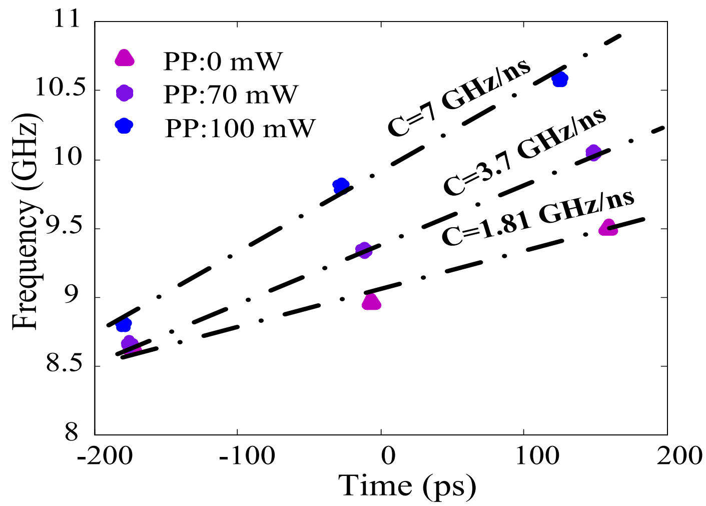

Fig. 4.12. The frequency versus time for the generated chirped microwave waveforms at different pumping power levels. PP: pumping power.

To demonstrate the waveform compression performance, we calculate the auto-correlation of the experimentally generated chirped microwave waveforms, shown as the solid line in Fig. 4.11(a) and (c). The results are shown in Fig. 4.13(a) and (b). It is clearly seen that the microwave waveforms are compressed, which confirms that the generated microwave waveform is frequency chirped. The FWHM temporal width of the correlation peak in Fig. 4.13(a) is 67 ps while it is 57 ps in Fig. 4.13(b). This shows that the compression ratio is larger for a pumping power of 100 mW since the corresponding chirp rate is higher. The noise performance is also evaluated. To do so, we add an additive white Gaussian noise (AWGN) to the chirped microwave waveforms. Fig. 4.14 shows the correlation between the chirped microwave waveforms at different signal-to-noise ratio (SNR) levels of 0 dB, -5 dB, -10 dB, and -12 dB and the reference waveforms. As can be seen, even for an SNR as low as -12 dB, the correlation peak is still detectable. Thus, it is confirmed that the use of the generated chirped microwave waveform would increase the robustness of the system to noise.

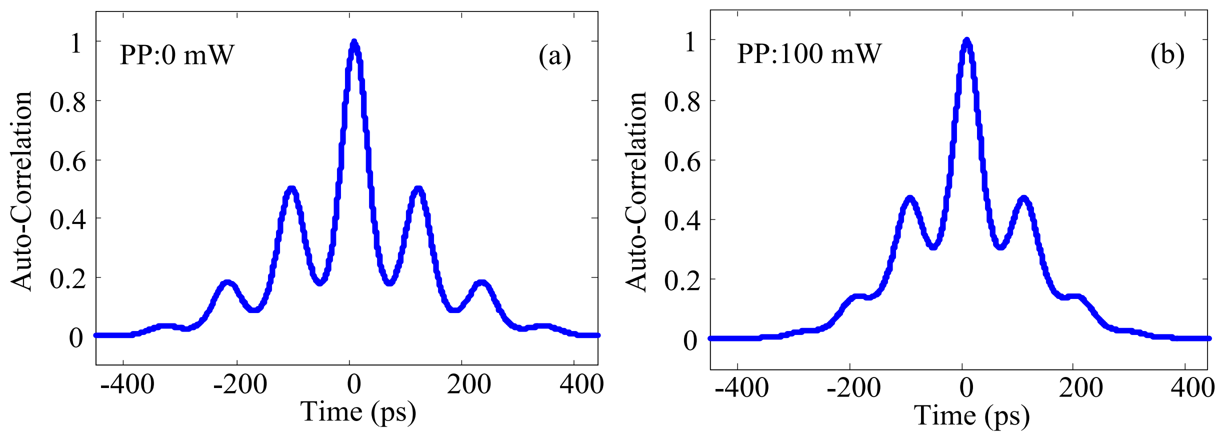

Fig. 4.13. Auto-correlation of the experimentally generated waveforms with a pumping power of (a) 0 mW, and (b) 100 mW.

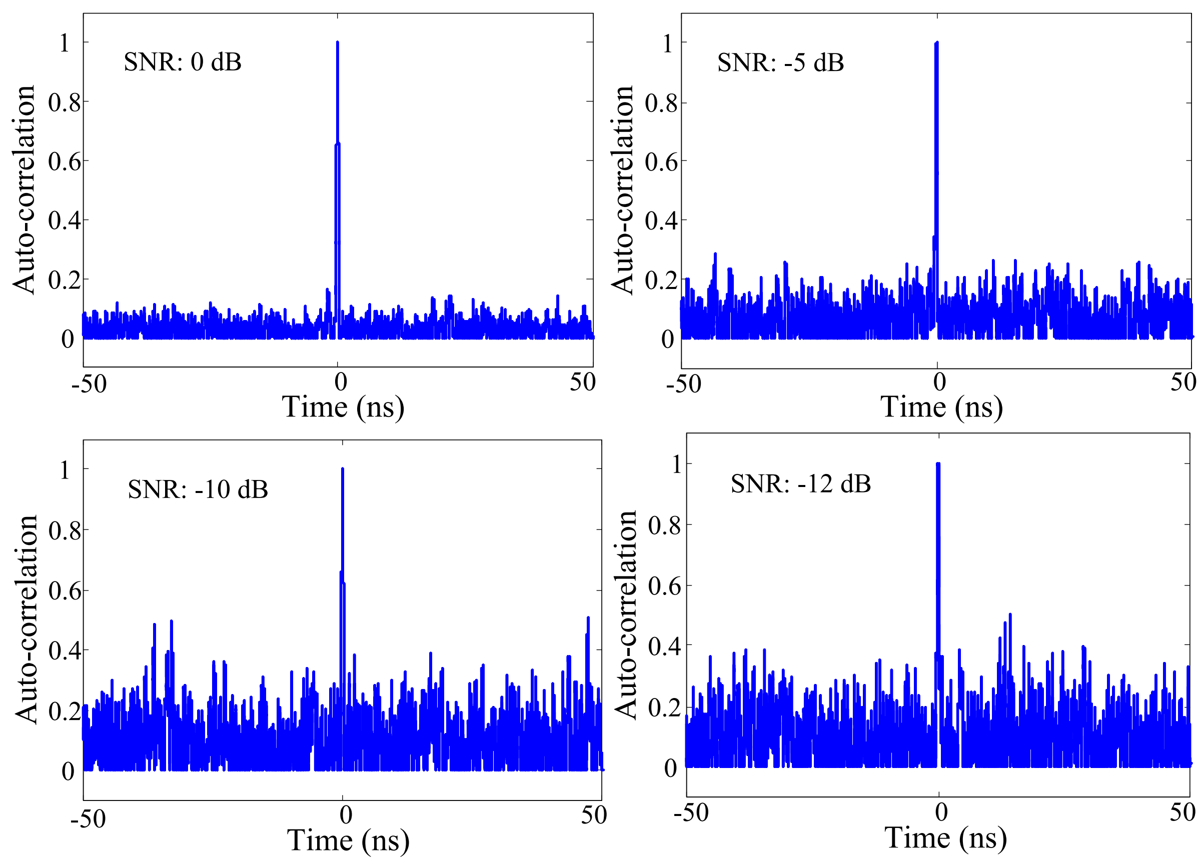

Fig. 4.14. Correlation between the reference waveforms and the chirped microwave waveforms added with an AWGN with an SNR of (a) 0 dB, (b) -5 dB, (c) -10 dB, and (d) -12 dB.

In conclusion, a novel and simple method to generate continuously tunable chirped microwave waveform was proposed and experimentally demonstrated. The entire system is considered to be a photonic microwave delay-line filter with nonuniformly spaced taps. When an ultra-short pulse was applied to the input of the photonic microwave delay-line filter, a pulse burst with nonuniform temporal spacing was generated. The key device to achieve nonuniform time delays was the TFBG, which was written in an Er/Yb co-doped fiber. TFBG has multiple resonances with linearly changing depths in its transmission spectrum enabling multi-wavelength linearly changing slow and fast light. By optically pumping the TFBG, the cladding mode resonance wavelengths were changed, leading to the change of the time delays. The proposed approach was experimentally demonstrated. By pumping the TFBG with a pumping power from 0 to 100 mW, a chirped microwave waveform with the continuously tunable chirp rate of 1.8 to 7 GHz/ns was demonstrated experimentally. In the experiment, the bandwidth of the generated chirped microwave pulses was about 2 GHz, which could be increased by increasing the maximum time advancement. In addition, the bandwidth of the MZM and the PD must be sufficiently large to support the generation of the waveforms with the required bandwidth.

4.3. Continuously tunable microwave photonic phase shifting

In this section, we propose and demonstrate a novel and simple microwave phase shifter based on slow and fast light effects in a TFBG. In the proposed system, the microwave signal to be phase shifted is modulated on an optical carrier at an optical single-sideband (OSSB) modulator. Two phase shifts are introduced to the optical carrier and the sideband of the OSSB-modulated signal by placing the optical carrier within the bandwidth of one of TFBG cladding-mode resonances, and placing the sideband outside of the resonance bandwidth. These phase shifts are tunable by optically pumping the TFBG by a 980-nm laser diode (LD). After beating the carrier and the sideband at a photodetector, the phase difference between these two is transferred to the phase shift of the generated microwave signal. A continually tunable phase shift of 280^{o} at a microwave frequency from 24 to 36 GHz is experimentally demonstrated.

There are multi resonances in the transmission spectrum of a TFBG. The theoretical study of the coupling between the core mode and the cladding modes can be found in [184]. Although it is possible to obtain multi-cladding resonances by cascading a strong FBG and long period gratings (LPGs) [185], using a single TFBG can be simpler and more effective. Based on KK relations, a change in the amplitude results in a change in the phase (φ), and consequently a change in the group delay ($\frac{d\varphi}{d\omega}$). Thus, within the bandwidth of each cladding-mode resonance, a tunable phase shift and consequently a tunable time delay can be achieved by slightly tuning the wavelength. To achieve a tunable phase shift at a fixed wavelength, the TFBG is written in an Er/Yb co-doped fiber and is optically pumped. Thanks to the high absorption of the Er/Yb co-doped fiber, the refractive index of the fiber is changed. Thus, by pumping the TFBG with a 980-nm LD having a tunable pumping power, the refractive index along the TFBG is changed which leads to the shift of the resonance wavelengths and thus the change of the phase shift at the fixed wavelength.

Fig. 4.15 shows the schematic block diagram of the proposed phase shifter. First, a microwave signal to be phase shifted is modulated on an optical carrier at an OSSB modulator, the OSSB-modulated signal is then sent to a TFBG in a way that the optical carrier falls within one cladding mode resonance and the sideband falls outside of the resonance. Phase shifts are introduced to the optical carrier and the sideband. The phase shifted optical carrier and the sideband are applied to a photodetector (PD). The beating between these two will generate a microwave signal with a phase shift directly transferred from the phase difference between the optical carrier and the sideband.

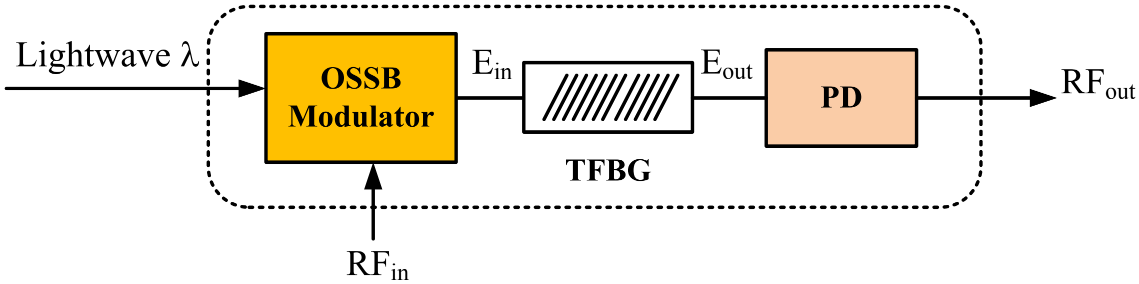

Fig. 4.15. Schematic block diagram of the proposed phase shifter. OSSB: optical single-sideband, PD: photodetector.

Mathematically, under small-signal modulation condition, the optical field at the output of the OSSB modulator, when it is driven by a microwave tone $\exp(2\pi f_{RF} t)$, is given by

$$E_{in}(t) = A_0 \exp(j2\pi v_0 t) + A_1 \exp[j2\pi(v_0 + f_{RF})t] \quad (4\text{-}9)$$

where A_0 and v_0 are the amplitude and frequency of the optical carrier, and A_1 and $v_0 + f_{RF}$ are the amplitude and frequency of the first-order sideband, respectively. If the optical carrier is tuned to be located at one of the cladding mode resonances of the TFBG and sideband is located outside of the resonance, the optical carrier and the sideband are modified by $A\exp(j\varphi)$ and $A'\exp(j\varphi')$, respectively, where A and A' are the amplitude modification factors and φ and φ' are the optical phase shifts introduced by the TFBG. Thus the optical filed at the output of the TFBG is given by

$$E_{out}(t) = A_0 A \exp(j\varphi)\exp(j2\pi v_0 t) + A_1 A' \exp(j\varphi')\exp[j2\pi(v_0 + f_{RF})t]. \quad (4\text{-}10)$$

By detecting the optical signal at the PD, a phase shifted microwave signal is obtained, which is given by

$$I(t) = R|E_{out}|^2 = RAA'A_0 \cos(2\pi f_{RF} t + \varphi' - \varphi) \quad (4\text{-}11)$$

where R is the responsivity of the PD. As can be seen from (4-11), the phase shift difference between the optical carrier and the sideband is directly translated to the microwave signal. The amount of the phase shift is optically tunable by pumping the TFBG which causes a continuous shift of the resonance spectrum, and consequently continues phase shifts are applied to the optical carrier and the sideband. In this scheme, since the sideband is located outside of the resonance, the amount of the phase shift applied to it is independent of the microwave frequency and therefore this phase shifter is independent of the microwave frequency. The bandwidth of the phase shifter can be very broad, which is just limited by the resonance spacing in the TFBG spectrum, and the bandwidths of the MZM and the PD.

The proposed optically tunable phase shifter is experimentally studied. For the experiment, a TFBG with a tilt angle of 6^o and a Bragg wavelength of 1560 nm is fabricated. The TFBG is fabricated by using an excimer laser with a uniform phase mask. The tilt angle is introduced by a focal lens. The fiber used to fabricate the LCFBG is a photosensitive Er/Yb co-doped fiber (EY-305, Coractive) which is hydrogen loaded for two weeks to further increase the photosensitivity. Fig. 4.16(a) and (b) shows the magnitude and phase responses of one of the cladding-mode resonances of the fabricated TFBG at the wavelength of 1538.38 nm, which is measured using an optical vector analyzer (LUNA Optical vector analyzer CTe). As can be seen, by pumping the TFBG, the resonance wavelength is shifted to a longer wavelength and the phase response is also shifted accordingly. This tunable phase shift can be used to introduce a tunable phase shift to the optical carrier of an OSSB-modulated signal to obtain a phase shifted microwave signal.

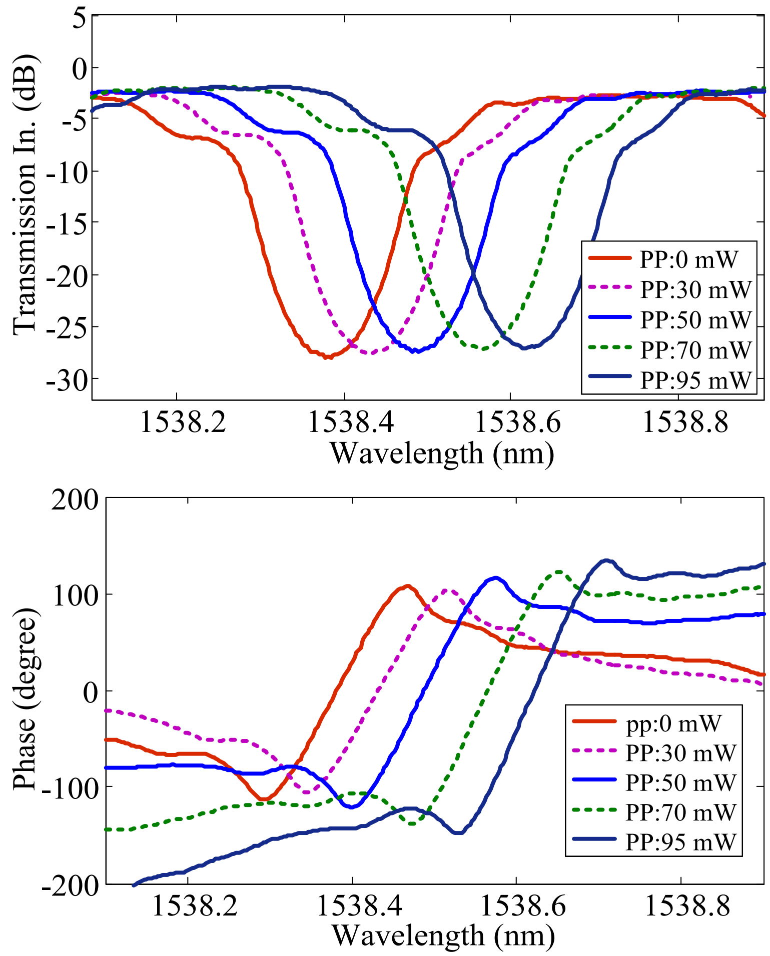

Fig. 4.16. (a) The magnitude response, and (b) phase response of one cladding-mode resonance channel of the TFBG at different pumping power levels. PP: pumping power.

The experimental setup is shown in Fig. 4.17. A lightwave from a tunable laser source (TLS) is sent to a 40 GHz MZM. The wavelength of the lightwave is selected to be in the bandwidth of one of the TFBG's cladding mode resonances. A microwave tone generated by a signal generator (Agilent E8254A) is applied to the MZM via the RF port to modulate the lightwave. The MZM is biased at the quadrature point. Then, an optical double-sideband

(ODSB) with carrier signal is obtained at the output of the MZM. To suppress one of the two sidebands, a wave shaper (Finisar WaveShaper 4000S) is serving an optical notch filter to suppress one sideband, and is connected to the output of the MZM. The OSSB-modulated optical signal is sent to the fabricated TFBG through a wavelength division multiplexing (WDM) coupler. The TFBG is pumped by a 980-nm LD. The optical signal at the output of the TFBG is sent to an erbium-doped fiber amplifier (EDFA) to compensate for the loss caused by the resonance notch, and is detected by a PD, and the electrical waveform is observed by a sampling oscilloscope (Agilent 86100C). Assuming that the bandwidths of the MZM and the PD are sufficiently large, the bandwidth of the phase shifter is limited by the resonance bandwidth and resonance spacing of the TFBG. The wavelength of the optical carrier is selected to be in the bandwidth of the resonance shown in Fig. 4.16. The magnitude response of this resonance shows that this phase shifter has a bandwidth of 24-60 GHz. As can be seen in Fig. 4.16(b), the phase shift is changing from about -140^o to 140^o by tuning the pumping power from 30 to 95 mW. Therefore, this TFBG resonance with these properties has the potential to be a phase shifter with a continuously tunable range of 280^o and a bandwidth of 24-60 GHz. However, the experiment is done for the frequencies from 24-36 GHz because of the limited bandwidths of the MZM and the PD.

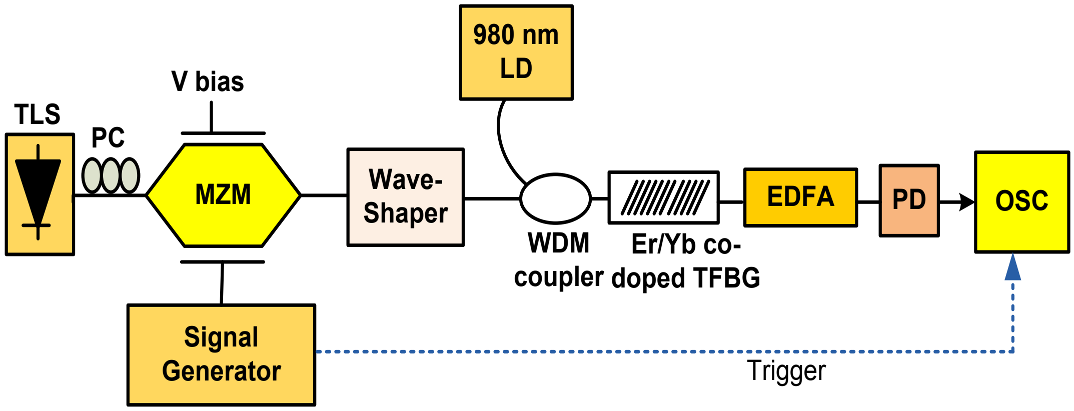

Fig. 4.17. Experimental setup. TLS: tunable laser source, PC: polarization controller, MZM: Mach–Zehnder modulator, LD: laser diode, WDM: 980/1550 nm wavelength division multiplexer, EDFA: erbium-doped fiber amplifier, PD: photo-detector, OSC: oscilloscope.

Fig. 4.18(a) and (b) shows the phase shifted microwave signals at 28 and 34 GHz. The phase shifted microwave signal obtained at a pumping power of 60 mW is chosen as a reference, and by tuning the pump power from 30 to 95 mW, a tunable phase shift from +140^o to -140^o is achieved. As expected, the phase shift is independent of the microwave frequency. Fig. 4.19 shows the phase shift of the recovered microwave signal at different frequencies. As can be seen a tunable phase shift from +140^o to -140^o is achieved by tuning the pumping power from 30 to 95 mW for a microwave frequency tunable from 24 to 36 GHz. The pumping powers corresponding to the different phase shifts in Fig. 4.19 are 30, 40, 50, 60, 70, 80, and 95 mW from top to bottom.

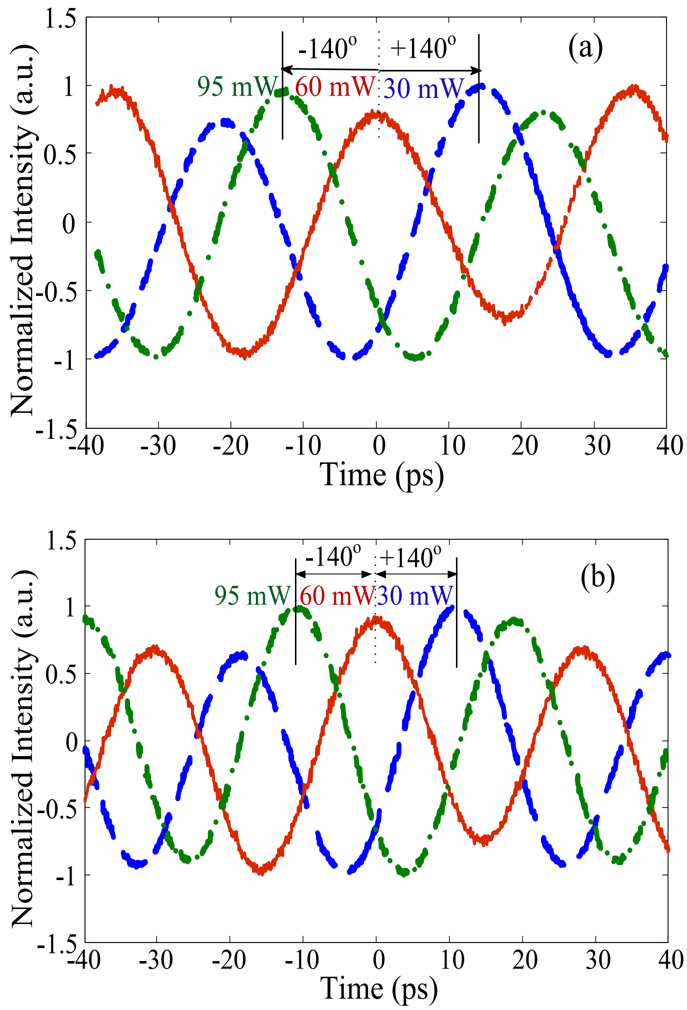

Fig. 4.18. The detected signals at pump power levels of 30, 60 and 95 mW for the RF frequency of 28 GHz and (b) 34 GHz. PP: pumping power.

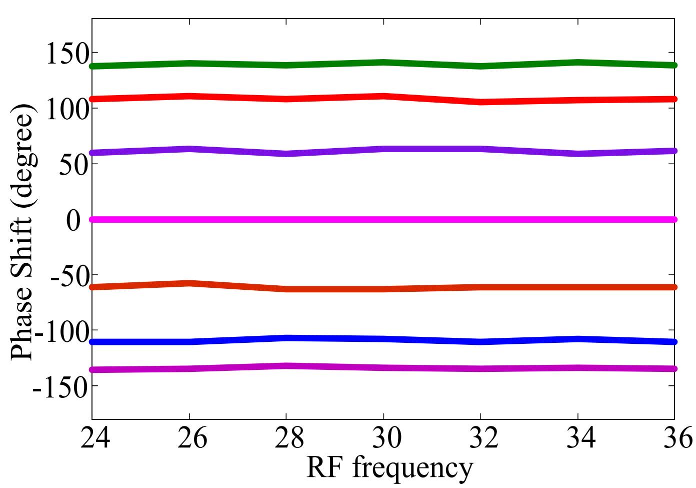

Fig. 4.19. Measured phase shifts at different pumping power levels. The phase shifts are independent of the microwave frequency.

In conclusion, a novel and simple approach to implementing a photonic phase shifter with a continuously tunable phase shift based on a TFBG written in an Er/Yb co-doped fiber was proposed and demonstrated. This method is based on the optically pumping of a TFBG written in an Er/Yb co-doped fiber. The magnitude and phase responses of the cladding mode resonances of the TFBG were tuned by tuning the pumping power to the TFBG, which led to the tuning of the phase shift introduced to the optical carrier and the sideband of an OSSB-modulated signal. A 280^{o} continuously tunable phase shifter at a microwave frequency tunable from 24 to 32 GHz was demonstrated experimentally.

4.4. Optically tunable fractional order temporal differentiation

In this section, we propose and demonstrate a continuously tunable fractional differentiator using a TFBG written in an Er/Yb co-doped fiber. By optically pumping the TFBG, the phase of a cladding mode resonant wavelength is changed. By locating the wavelength of the input lightwave at the location of the cladding mode resonant wavelength, a temporal differentiator with a tunable fractional order is achieved. An experiment is performed. A differentiator with a tunable fractional order is demonstrated. The use of the fractional order differentiator to implement temporal differentiation of a Gaussian pulse with a bandwidth of 28 GHz and 75 GHz is also demonstrated.

For a signal $x(t)$, the Fourier transform of its *n*th order differentiation, $dx^n(t)/dt^n$, is expressed as $[j(\omega-\omega_0)]^n X(\omega-\omega_0)$, where ω is the optical frequency, ω_0 is the carrier frequency, and $X(\omega)$ is the Fourier transform of $x(t)$. Therefore, the differentiator can be considered as an ideal filter with a frequency response such as,

$$H_n(\omega) = [j(\omega-\omega_0)]^n = \begin{cases} e^{jn(\frac{\pi}{2})}\left|(\omega-\omega_0)\right|^n & \omega > \omega_0 \\ e^{jn(-\frac{\pi}{2})}\left|(\omega-\omega_0)\right|^n & \omega < \omega_0 \end{cases}. \quad (4\text{-}12)$$

As was discussed earlier, by pumping an Er/Yb co-doped fiber with a 980-nm laser diode (LD), due to the high absorption of the Er/Yb co-doped fiber, the refractive index is changed. Based on (3-21) and (3-22), the resonance wavelengths are tuned. In addition, the coupling coefficient of each coupling mode depends on $n_{eff,core}$ [179], thus different coupling coefficients are achieved, leading to the tuning of the phase jump at the resonant wavelength. By locating the wavelength of the input lightwave at the location of a specific cladding mode resonant wavelength, a temporal differentiator with a tunable fractional order is achieved.

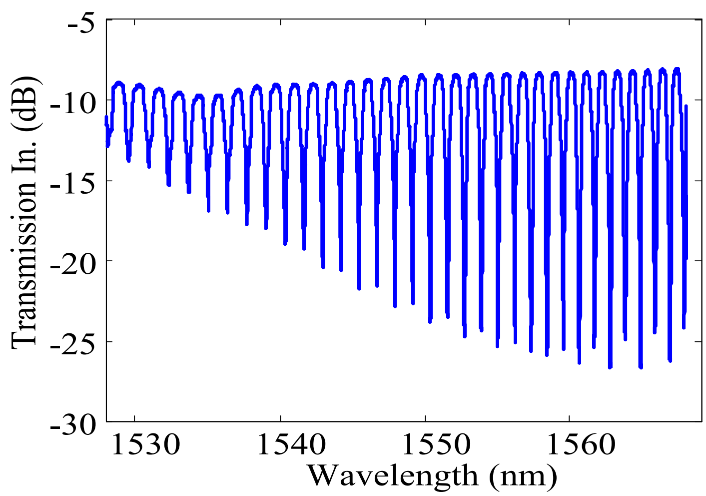

Fig. 4.20. Transmission spectrum of a TFBG with a tilt angle of 10°, Bragg wavelength of 1600 nm, and chirp rate of 4.8 nm/cm.

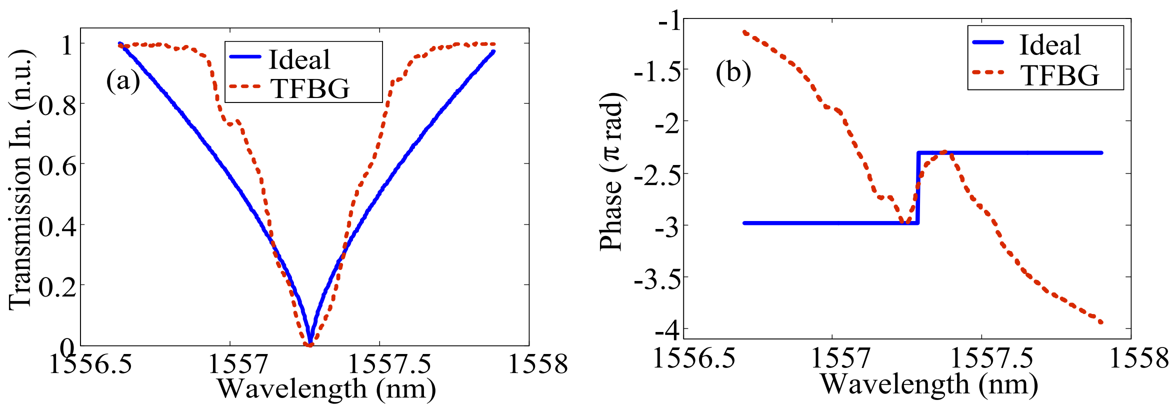

Fig. 4.21. (a) The magnitude response and (b) phase response of one channel of the TFBG. The solid lines show the magnitude and phase responses of an ideal differentiator.

The bandwidth of the proposed differentiator is limited by the bandwidth of the cladding mode resonances, therefore in order to increase the bandwidth a chirp is introduced to the TFBG. Fig. 4.20 shows the transmission intensity spectrum of a fabricated TFBG with a tilt angle of 10^o, Bragg wavelength of 1600 nm, and chirp rate of 4.8 nm/cm. Fig. 4.21(a) and (b) shows the magnitude and phase responses of one of the cladding-mode resonances with the resonance wavelength of 1557.27 nm measured by a LUNA optical vector analyzer. As can be seen, the phase jump at this resonance wavelength is 0.67π, thus a differentiator with a fractional order of 0.67 can be achieved by introducing an input signal with the carrier wavelength of 1557.27 nm to this TFBG. The bandwidth of this differentiator is 0.8 nm or equivalently 100 GHz. Fig. 4.21(a) and (b) shows the magnitude and phase responses of an ideal fractional differentiator with an order of 0.67π. As can be seen the magnitude and phase responses of the TFBG are close to those of an ideal fractional differentiator. The use of the TFBG and the ideal differentiator to perform wideband differentiation of a Gaussian pulse is then simulated. The temporal FWHM of the input pulse is 8 ps. The input pulse and output results are shown in Fig. 4.22. A good agreement between the output pulse of the

TFBG-based differentiator and that of an ideal differentiator is reached. The RMSE is also calculated, which is 7.1%.

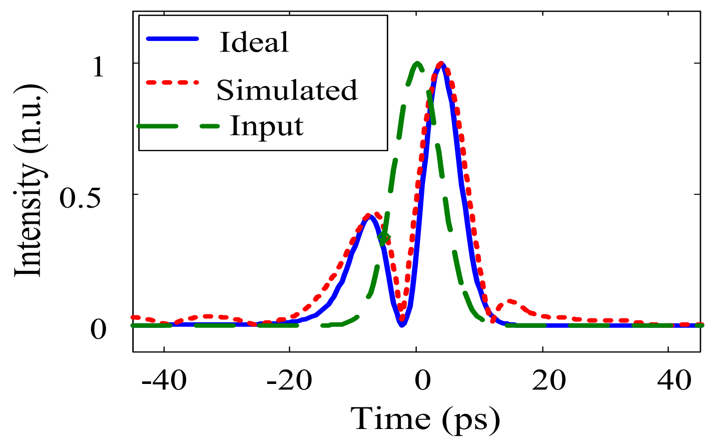

Fig. 4.22. Simulated output pulse from the TFBG. The dotted line shows the output pulse from an ideal differentiator. The fractional order is 0.67.

Then, the tunability is investigated. To do so, the TFBG is pumped by a 980-nm LD. By changing the pumping power, the magnitude and phase responses of the TFBG at different cladding mode resonances are changed. Fig. 4.23 (a) and (b) shows the change of the magnitude and phase responses for a cladding mode resonance at 1550.3 nm of the TFBG. As can be seen in Fig. 4.23, by changing the pumping power from 0 to 135 mW, the resonance wavelength is shifted to higher wavelengths, and the introduced phase jump at the resonance wavelength is changed from 1.25π to 1.72π, thus the order of the differentiator can be tuned from 1.25 to 1.72.

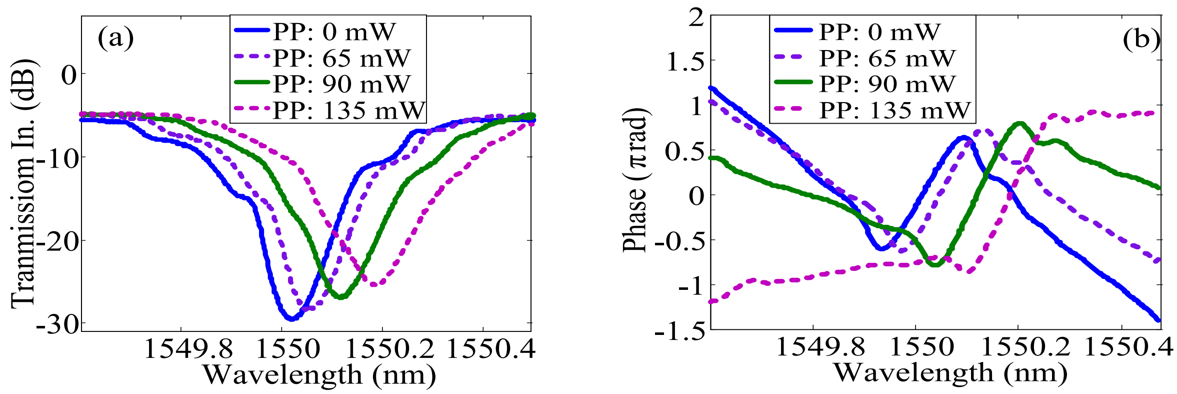

Fig. 4.23. (a) The magnitude responses and (b) phase responses of a cladding mode resonance with a pumping power from 0 to 135 mW. PP: pumping power. In.: Intensity.

The proposed optical tunable temporal differentiator is also experimentally evaluated. Fig. 4.24 shows the experimental setup. A mode-lock laser (MLL) is used to generate a short pulse with a temporal width of 550 fs. A TFBG with a tilt angle of 10°, Bragg wavelength of 1600 nm, chirp rate of 4.8 nm/cm which has a length of 1 cm is used as a differentiator. The TFBG is fabricated by using an excimer laser with a uniform phase mask. The tilt angle is introduced by using a focal lens. A 980-nm LD is used to pump the TFBG via a WDM coupler. The differentiated optical pulse is detected by a 53 GHz photodetector and its waveform is observed by a sampling oscilloscope.

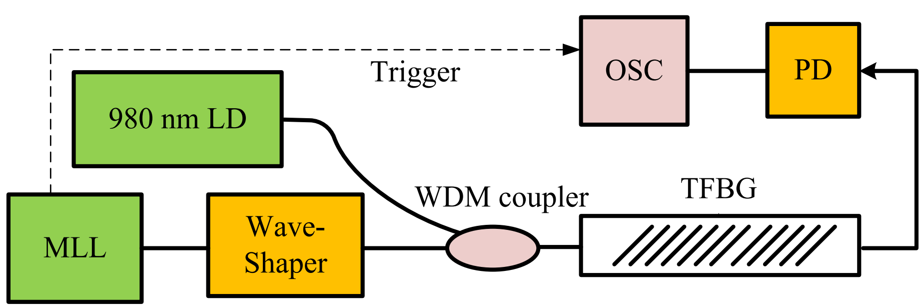

Fig. 4.24. Experimental setup of a fractional order differentiator. MLL: mode-locked laser; LD: laser diode, WDM: 980/1550 nm wavelength division multiplexer, PD: photo-detector, OSC: oscilloscope.

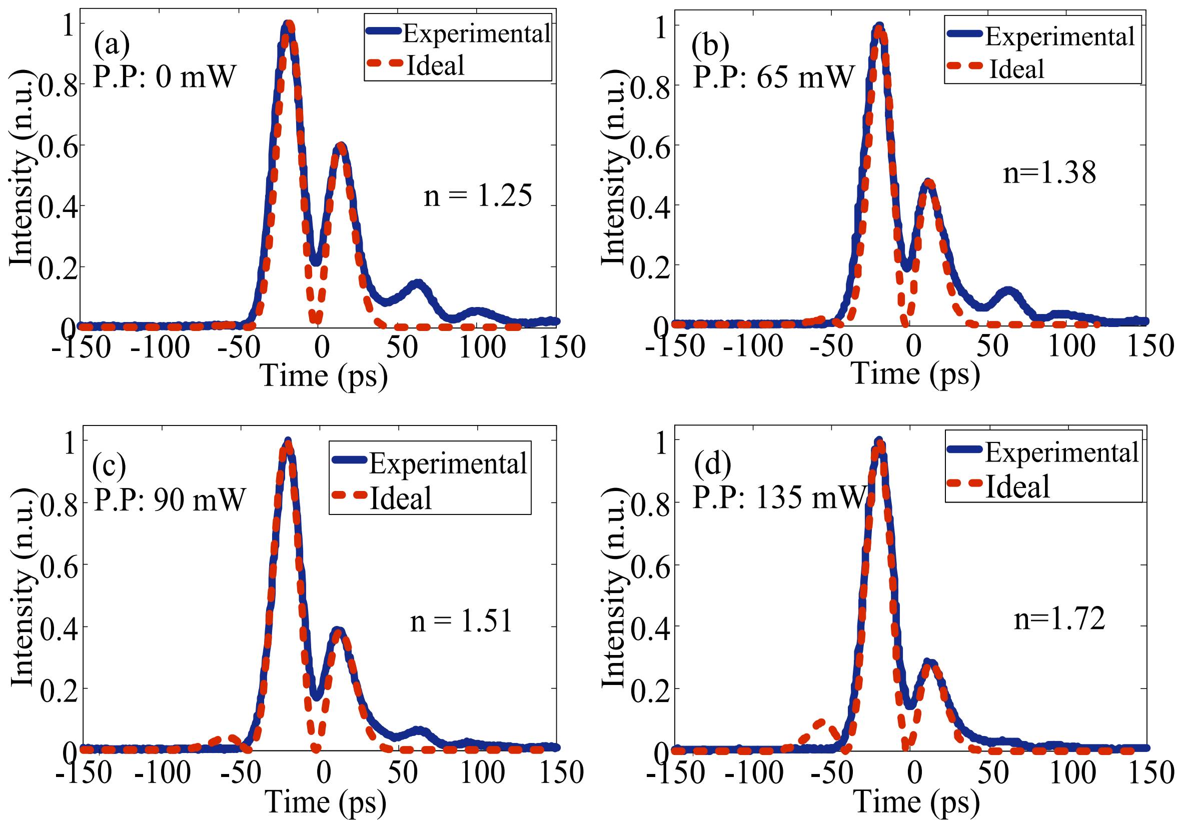

Fig. 4.25. Differentiation of a Gaussian pulse with the bandwidth of 28 GHz achieved at the output of the TFBG pumped with a pumping power tuned from 0 to 135 mW.

First, we show the tuning of the fractional order and the differentiation of a Gaussian pulse at different differentiation orders. In the experiment, a Gaussian pulse with a bandwidth of 28 GHz obtained by filtering an ultra-short optical pulse from the MLL using a WaveShaper is applied to the TFBG. A cladding mode resonance at 1550.04 nm is selected. As can be seen by increasing the pumping power from 0 to 135 mW (or the injection current to the LD from 0 to 175 mA), the differentiation order is changed from 1.25 to 1.72. It should be mentioned that by increasing the pumping power from 0 to 135 mW, the resonance wavelength is shifted from 1550.04 to 1550.24 nm. Thus the carrier wavelength of the Gaussian pulse is adjusted by changing the central wavelength of the WaveShaper. Fig. 4.25 shows the differentiated pulses at different fractional orders. The pulses by an ideal differentiator are also shown in Fig. 4.25 for comparison. As can be seen a good agreement between the ideally differentiated pulses and the experimentally differentiated pulses is reached. The RMSE for n = 1.25 is 8%, which is the largest error.

Then, a Gaussian pulse with a bandwidth of 75 GHz is generated by reconfiguring the WaveShaper and is applied to the TFBG. Since the bandwidth of the differentiator is 100 GHz, the input Gaussian pulse can be effectively differentiated. A different cladding mode resonance at 1559 nm is selected. The pumping power is tuned at 122 mW and 140 mW corresponding to a fractional order of 0.95 and 1, respectively. The generated waveforms are shown in Fig. 4.26(a) and (b). The errors compared with the ideal waveforms are larger; especially at the notch. The large errors are caused mainly due to the limited bandwidth of the photodetector (53 GHz). Again, the RMSE is also calculated, which is 16%.

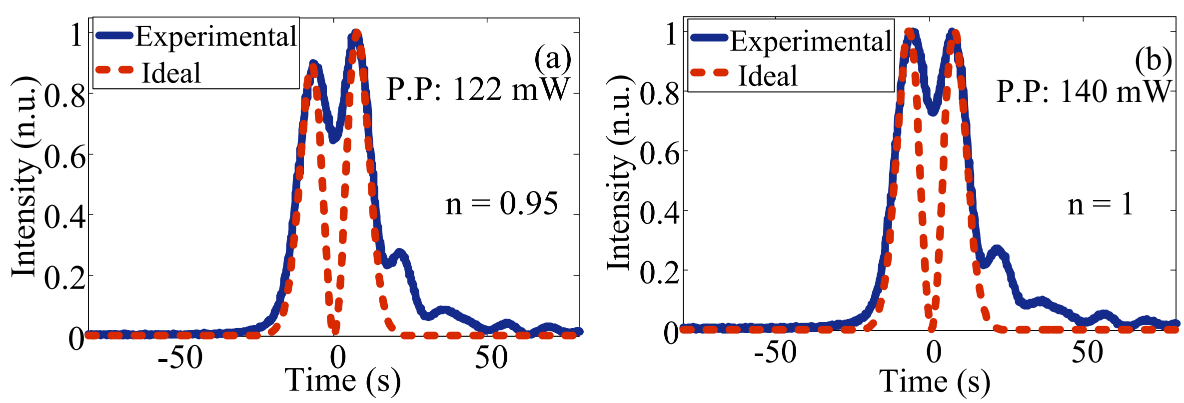

Fig. 4.26. Differentiation of a Gaussian pulse with the bandwidth of 75 GHz achieved at the output of the TFBG pumped with a power at 122 mW and 140 mW. The carrier wavelength is tuned at 1559 nm.

Note that when the TFBG was pumped, both the magnitude and phase responses were changed. The magnitude response of an ideal fractional differentiator is given by $|(\omega-\omega_0)|^n$ which was not exactly satisfied when using a TFBG, as can be seen from Fig. 4.23(a).

However, for the implementation of a differentiator, the phase response plays a much more important role [186]. This explains the generated waveforms were close to the waveforms based on an ideal differentiator with small errors.

The key significance of the approach is that a TFBG written in an Er/Yb co-doped fiber was employed. When pumped, the phase responses of the cladding mode resonances were tuned and led to the tuning of the fractional order differentiation. The proposed approach was evaluated by an experiment. A differentiator with a continuously tunable fractional order was demonstrated. The differentiation of a wideband Gaussian pulse with a bandwidth of 28 and 75 GHz was also performed.

4.5. Continuously tunable microwave photonic filtering

4.5.1. Two-tap photonic microwave filter

We propose and demonstrate a two-tap photonic microwave FIR filter with a complex coefficient using a novel microwave photonic phase shifter based on slow and fast light effects in a TFBG. The demonstrated TFBG-based phase shifter in section 4.3 is incorporated into a two-tap microwave photonic delay-line filter to produce one tunable complex coefficient. The FIR filter is tuned by optically pumping the TFBG by the 980-nm LD. A microwave photonic filter with a spectral response tunable over a frequency range of 1.72 GHz while maintaining a fixed spectral shape is experimentally demonstrated.

As was seen in Fig. 4.16, by pumping a TFBG with the tilt angle of 6^{o}, the resonance wavelength is shifted to a longer wavelength and the phase response is also shifted accordingly. This tunable phase shift can be used to implement a tunable phase shifter and obtain a complex-valued tap. By incorporating the TFBG-based phase shifter into a delay-line filter, a two-tap photonic microwave delay-line filter with a complex coefficient is achieved. The block diagram of the proposed two-tap photonic microwave filter with a complex coefficient is shown in Fig. 4.27. If the input signal to this filter is $x(t)$, the output signal $y(t)$ is

$$y(t) = a_1 x(t) - a_2 \exp(-j\varphi) x(t-\tau) \tag{4-13}$$

where, a_1 and $-a_2$ are the coefficients of tap 1 and tap 2, respectively, φ is the phase shift to the microwave signal introduced by the phase shifter, and τ is the time delay between the two taps. The frequency response of the filter, by getting the Fourier transom of (4-13), is given by

$$H(j\omega) = a_1 - a_2 \exp(-j\varphi)\exp(-j\omega\tau)\,. \tag{4-14}$$

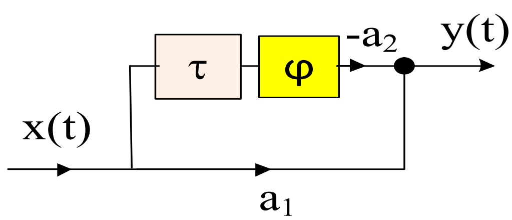

Fig. 4.27. A two-tap photonic microwave delay-line filter with one complex coefficient.

Fig. 4.28 shows the simulated frequency response of a microwave photonic delay-line filter with $a_1 = a_2 = 0.5$, $\tau = 470$ ps, and different phase shifts of $\varphi = 0^0$, 140^0 and -140^0. As can be seen for $\varphi = -140^0$, the frequency response experiences a shift of 0.86 GHz toward the higher frequencies, and for $\varphi = +140^0$, a shift of 0.86 GHz toward the lower frequencies.

A photonic microwave filter with a spectral response tunable over a frequency range of 1.72 GHz is achieved by changing the phase shift from -140^0 to $+140^0$.

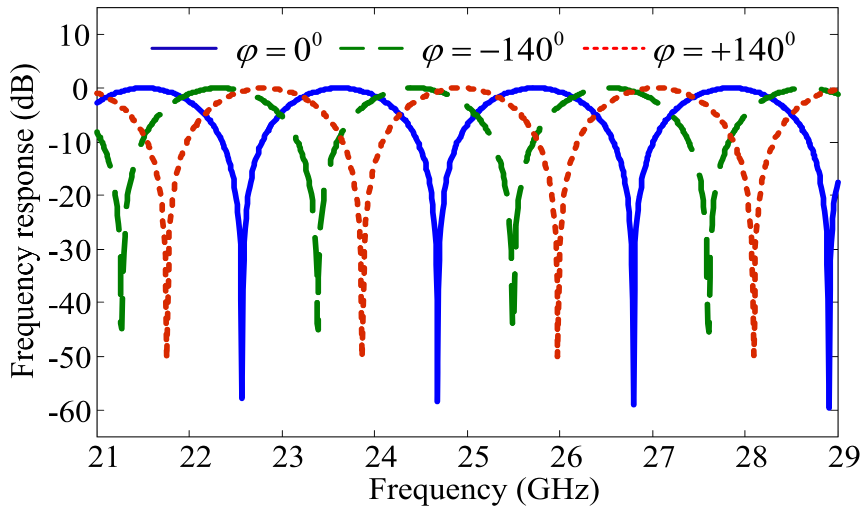

Fig. 4.28. Simulated frequency response of a photonic microwave delay-line filter with a complex coefficient.

An experiment is performed to verify the proposed two-tap photonic microwave filter. Fig. 4.29 shows the experimental setup of the two-tap photonic microwave delay-line filter. The upper channel has a microwave phase shifter, shown in the dotted-line box, which is an optically pumped TFBG, and the lower channel consists of a length of the single-mode fiber (SMF) to introduce a time delay between two arms.

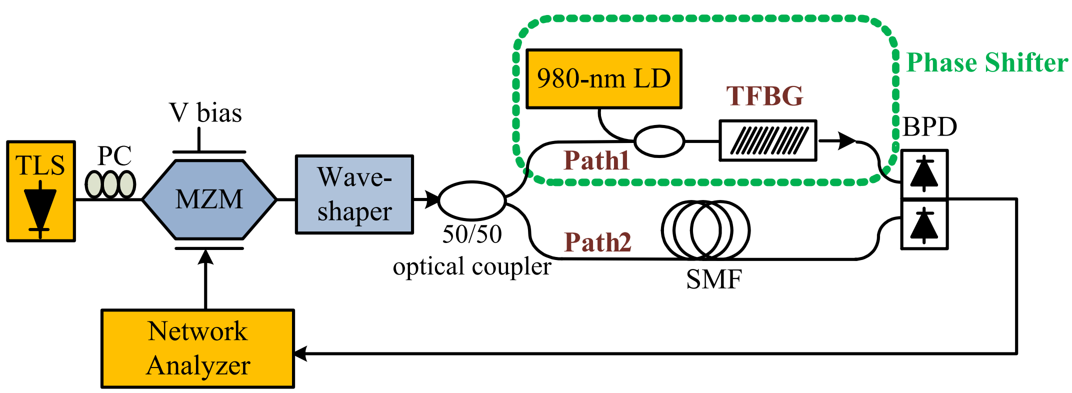

Fig. 4.29. Experimental setup of the proposed filter. TLS: tunable laser source, PC: polarization controller, MZM: Mach–Zehnder modulator, LD: laser diode, SMF: single mode fiber, PD: photo-detector.

The lightwave from the TLS at a wavelength of 1538.5 nm (centered at one of the TFBG's resonances) is injected to the MZM through a PC. A microwave signal generated by a vector network analyzer (VNA, Agilent E8364A) is applied to the MZM via the RF port to modulate the lightwave. The MZM is biased at the quadrature point; a double-sideband with carrier signal is obtained at the output of the MZM. A WaveShaper is used to suppress one of two sidebands and thus an OSSB modulated signal is generated. The OSSB-modulated signal is divided into two paths by a 50/50 optical coupler. The length of path 1 is 10 cm longer than that of path 2, thus the time delay due to the length difference is 470 ps, corresponding to an FSR of 2 GHz. The modulated signal traveling along the upper channel would experience a phase shift due to the TFBG. Fig. 4.30 shows the phase shift of the recovered microwave signal of the upper line for different microwave frequencies. As can be seen a tunable phase shift from -140^o to +140^o is achieved by tuning the pump power from 30 to 95 mW for a microwave frequency from 24 to 36 GHz. The pumping powers corresponding to the different phase shifts in Fig. 4.30 are 30, 40, 50, 60, 70, 80, and 95 mW from top to bottom. To avoid optical interference, which is extremely sensitive to environmental perturbations, the detection of the two time-delayed signals is performed using a 40-GHz balanced PD (BPD), thus the two signals will not interfere in the optical domain. The detected signal is sent back to the VNA to measure the frequency response of the filter. The experimental results for the operating bandwidth of 21-29 GHz are shown in Fig. 4.31. The Frequency response of the filter at the pumping power of 60 mW is considered as the reference. By changing the pumping power from 60 to 30 mW, the frequency response is 0.86 GHz shifted to the lower frequencies since the phase shift in path 1 is changed from 0^o to +140^o. Similarly, by changing the pumping power from 60 to 95 mW, the frequency response is 0.86 GHz shifted to the higher frequencies since the phase shift in path1 is changed from 0^o to -140^o. Also, the frequency responses of the filter at the pumping powers of 50 mW and 70 mW, which correspond to a phase shift of about $+60^o$ and -60^o, respectively, are shown in Fig. 4.31. As can be seen the frequency response is shifted by 0.36 GHz to a lower and 0.36 GHz to a higher frequencies at the pumping power of 50 and 70 mW, respectively. The maximum shift of the frequency response is 1.72 GHz, corresponding to a change of the pumping power from 30 to 95 mW. As expected, for the frequency response, although the central frequency is shifted, the overall shape is maintained unchanged. This is the key feature of a photonic microwave filter with complex coefficients. A slight decrease in the frequency response for higher frequencies is due to the limited bandwidths of the MZM and the BPD used in the experiment.

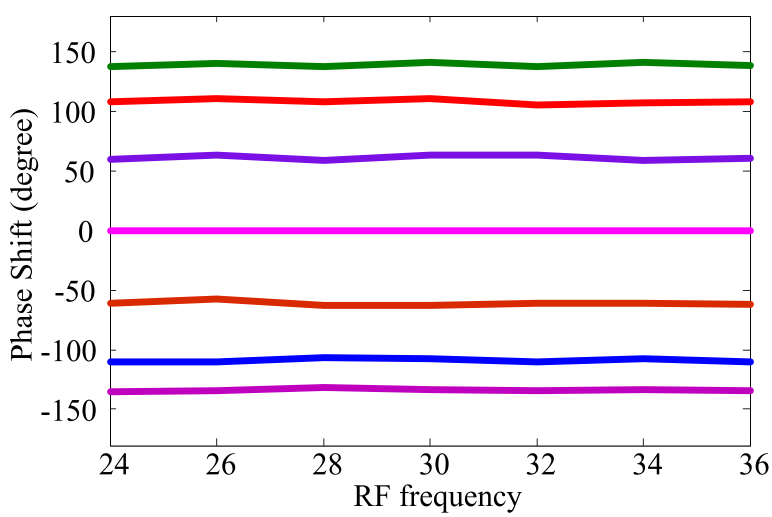

Fig. 4.30. Measured phase shift at different pumping power levels. The phase shift is independent of microwave frequency.

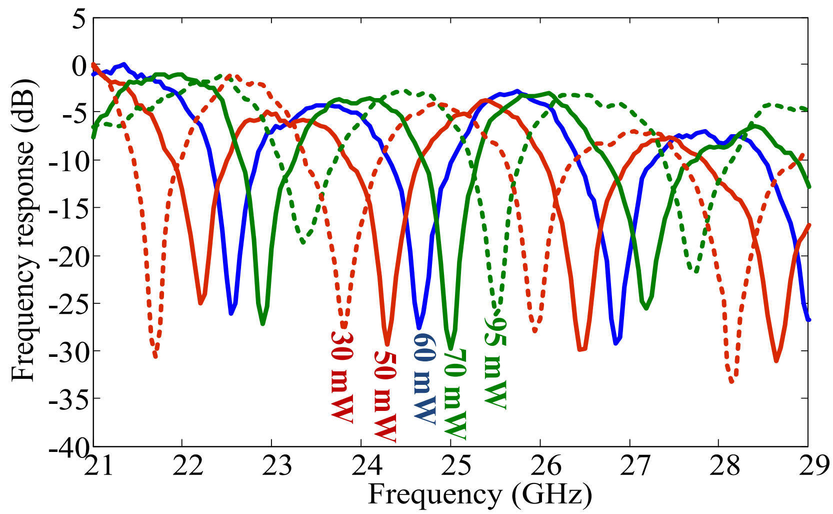

Fig. 4.31. Tunable frequency response of a microwave photonic filter with a tunable complex coefficient.

In conclusion, a photonic microwave filter with a complex coefficient achieved by using an optical phase shifter based on a pumped TFBG was proposed and experimentally demonstrated. The magnitude and phase responses of a cladding-mode resonance of the TFBG were tuned by optically pumping the TFBG which was written in an Er/Yb co-doped fiber, which led to the tuning of the phase shifter. A two-tap photonic microwave filter with a tunable frequency response of the range of 1.72 GHz, while maintain the shape of the frequency response unchanged, was demonstrated.

4.5.2. Multi-tap photonic microwave filter

In this section, we propose and demonstrate a multi-tap photonic microwave FIR filter with complex coefficients using a single TFBG. The frequency tunability is achieved by optically pumping the TFBG, thus the wavelengths of the laser sources are maintained fixed. To ensure effective tuning, the TFGB is written in an Er/Yb co-doped fiber. A TFBG has multiple resonances due to the coupling between the core mode and the cladding modes. One interesting feature of a TFBG is that the depths of the cladding-mode resonances of a TFBG are linearly changing in a wavelength region, and thus based on KK relations, the phase shifts are linearly changing. This feature can be perfectly employed to implement a multi-tap complex-valued microwave photonic filter in which the phase shifts of the tap coefficients are linearly changing. This is the first time, to the best of our knowledge, that this feature is discovered and employed to demonstrate a microwave photonic filter with complex coefficients.

For an *N* tap microwave photonic filter, *N* optical phase shifts that are linearly increasing are introduced to *N* optical carriers of *N* OSSB modulated signals by placing the optical carriers within the bandwidths of the cladding-mode resonances of the TFBG. The phase shifts are tunable by optically pumping the TFBG by a 980-nm LD. The proposed microwave photonic filter is experimentally demonstrated. A three- and four-tap filter with a tunable frequency range of 150 and 120 MHz, respectively, are demonstrated. The key significance of the approach is that the frequency tuning is done by simply pumping the TFBG, thus the wavelengths of the laser sources are maintained fixed. In addition, since the phase shifts are tuned, the spectral response of the filter is tuned without changing the shape of the spectral response.

The depths of the cladding mode resonances are linearly increasing and decreasing along the transmission spectrum of a TFBG [179]. Fig. 4.32 shows the transmission spectrum of a TFBG with a tilt angle of 6^{o} and a Bragg wavelength of 1560 nm. As can be seen, the resonance depths are linearly increasing in a wavelength range from 1528 to 1540 nm and based on KK relations, the resulted phase shifts are linearly changing. This area is shown in a red ellipse in Fig. 4.32.

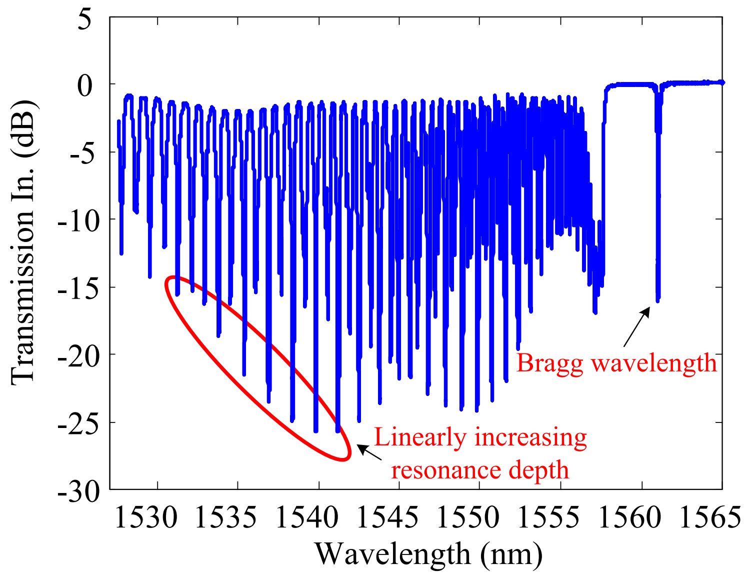

Fig. 4.32. The transmission spectrum of the fabricated TFBG with a tilt angle of 6° and a Bragg wavelength of 1560 nm. The red ellipse shows the area in which the resonance depths are linearly changing.

The tunability of a microwave photonic delay-line filter is usually achieved by adjusting the time-delay difference between samples. However, the change of the time-delay difference would lead to the change of the free spectral range (FSR), which would further result in the change of the 3-dB bandwidth as well as the entire shape of the frequency response. For many applications, however, it is highly desirable that only the center frequency of the pass-band or stop-band be changed while maintaining the shape of the frequency response unchanged during the tuning. A solution to this problem is to implement a microwave photonic delay-line filter with complex coefficients. An N-tap microwave photonic delay-line filter with complex coefficients should have a transfer function given by

$$\begin{aligned} H(j\omega) &= a_0 + a_1 e^{-j\theta} \cdot e^{-j\omega T} + \ldots + a_{N-1} e^{-j(N-1)\theta} \cdot e^{-j\omega(N-1)T} \\ &= \sum_{n=0}^{N-1} a_n e^{-jn\theta} e^{-j\omega nT} \end{aligned} \quad (4\text{-}15)$$

where ω is the microwave frequency, a_n is the coefficient of the nth tap, T is the time-delay difference between two adjacent taps, and θ is the basic phase shift. To tune the filter while maintaining the shape of the frequency response unchanged, the phase shifts of all the taps should maintain a fixed relationship given by $[0, \theta, 2\theta, 3\theta, ..., (N-1)\theta]$ during tuning. The inherent spectral response of a TFBG enables a simple implementation of a multi-tap microwave photonic filter with complex coefficients.

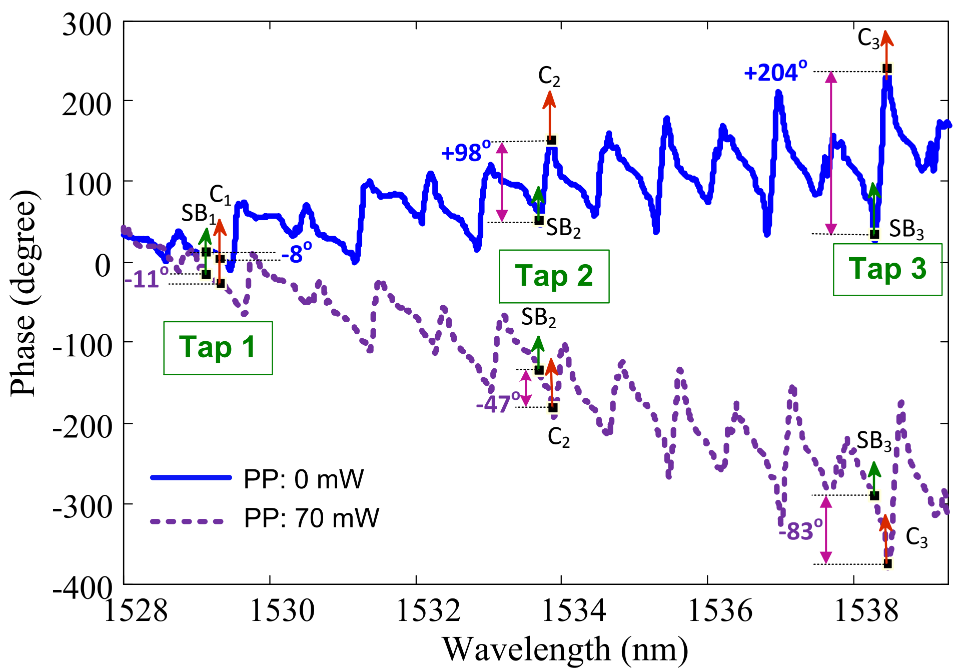

Fig. 4.33. The phase responses of the TFBG and the placement of the wavelengths of the optical carriers for a three-tap filter at two pumping powers of 0 and 70 mW. C1, C2 and C3 represent the three carriers, and SB1, SB2 and SB3 represent the three sidebands.

Fig. 4.33 shows the TFBG's phase responses in the wavelength range of 1528-1540 nm. The placement of the wavelengths of the optical carriers for a three-tap filter at a pumping power of 0 and 70 mW is shown. As can be seen at the pumping power of 0 mW, the phase shifts of +204°, +98°, and -11° are introduced to tap 3, 2, and 1, respectively, which corresponds to a basic phase shift of $\theta = +109^0$ in (4-15). By changing the pumping power to 70 mW, the phase shifts of -83°, -47°, and -11° are introduced to tap 3, 2, and 1, respectively, which corresponds to a basic phase shift of $\theta = -36^0$. Thus, by placing the tap wavelengths in the TFBG resonances as Fig. 4.33, the filter spectral response can be shifted by tuning the pumping power from 0 to 70 mW.

Fig. 4.34 shows the experimental setup of the proposed tunable microwave photonic delay-line filter. For an *N*-tap filter, *N* wavelengths are generated, which are sent to Mach-Zehnder modulator (MZM). The wavelengths of the lightwaves are selected to be in the bandwidths of the TFBG cladding-mode resonances with linearly increasing depths such that the phase shifts satisfy the relationship given in (4-15). A microwave signal generated by a vector network analyzer (VNA, Agilent E8364A) is applied to the MZM via the RF port to modulate the lightwaves. The MZM is biased at the quadrature point and a WaveShaper (Finisar 4000S Multiport Optical Processor) is used to suppress one of the two sidebands to obtain OSSB-modulated signals. The OSSB-modulated signals are sent to the TFBG through a wavelength division multiplexing (WDM) coupler. The fiber used to fabricate the TFBG is a photosensitive Er/Yb co-doped fiber (EY 305, Coractive). The TFBG is pumped by a 980-nm LD. The optical signals at the output of the TFBG are sent to a length of dispersive fiber (a single-mode fiber in the experiment) to introduce time delays. An EDFA is used to compensate the introduced losses. The time-delayed optical signals are detected by a 45-GHz photodetector. The detected signals are sent back to the VNA to measure the frequency response of the filter.

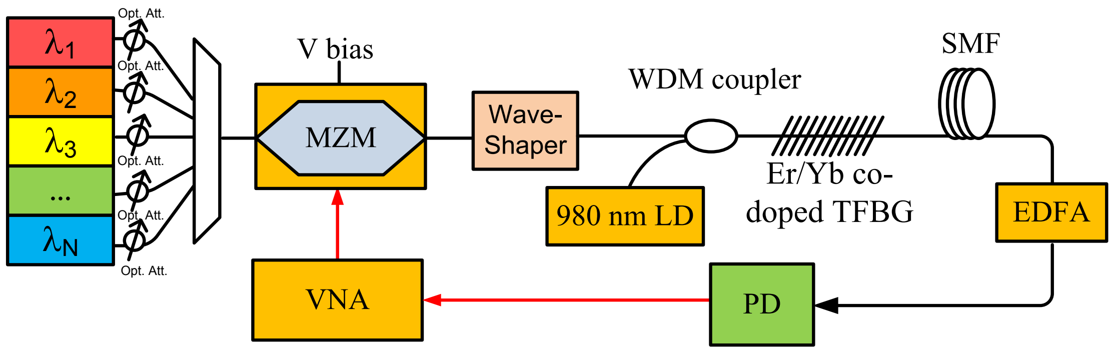

Fig. 4.34. Experimental setup of the proposed multi-tap microwave photonic filter with complex coefficients. Opt. Att.: optical attenuator, MZM: Mach–Zehnder modulator, LD: laser diode, WDM: 980/1550 nm wavelength division multiplexer, SMF: single mode fiber, EDFA: Erbium doped fiber amplifier, PD: photodetector, VNA: vector network analyzer.

In the experiment, the magnitudes of the tap coefficients a_n, are controlled by adjusting the optical attenuators in each tap. The FSR of the filter is controlled by the length of the single-mode fiber and the wavelength spacing. Fig. 4.35 shows the frequency response of a three-tap filter with different pumping powers changing from 0 to 70 mW (solid lines). The length of the SMF is 35 km, and the time delay difference between two adjacent taps is 2700 ps, corresponding to an FSR of 370 MHz. As mentioned above, the FSR can be tuned independently by changing the length of the dispersive fiber. For comparison, the simulated frequency responses are also shown in Fig. 4.35 as dashed lines. A good agreement is observed. As can be seen in Fig. 4.35, by changing the pumping power from 0 to 70 mW, the spectral response is shifted by 150 MHz, corresponding to a tunability of 40%. Note that since the phase relationship is always maintained during the pumping, the spectral shape of the spectral response is maintained unchanged.

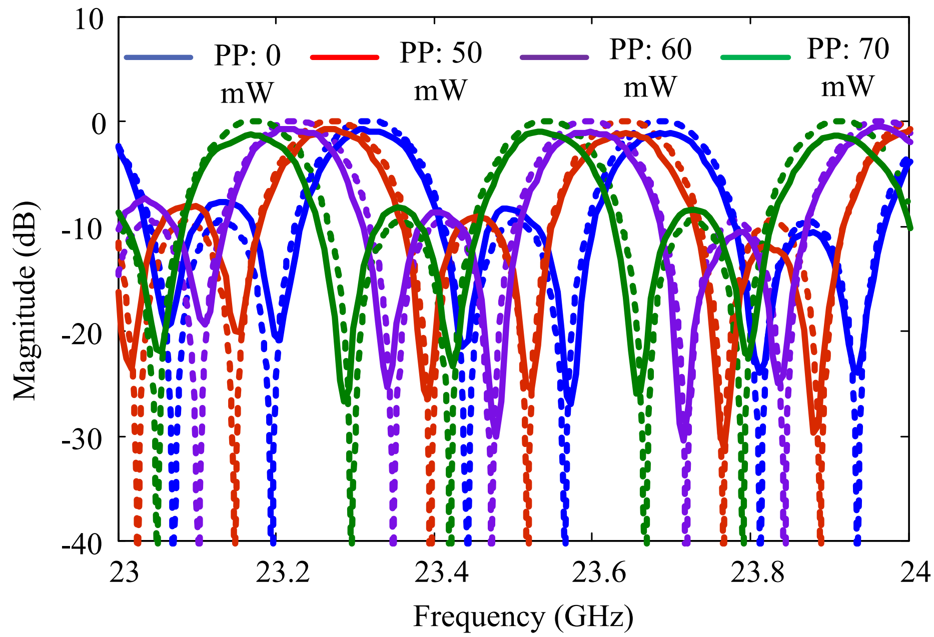

Fig. 4.35. Frequency response of the three-tap microwave photonic filter with complex coefficients at different pumping powers (solid lines). The dashed lines show the simulated frequency response corresponding to a basic phase shift of +105°, +58° , +10° and -36°. PP: pumping power.

A four-tap microwave photonic filter with four complex coefficients is then demonstrated. The spectral response is shown as solid lines in Fig. 4.36. The length of the SMF is 53 km, and the time delay difference between two adjacent taps is 2700 ps, corresponding to an FSR of 370 MHz. By changing the pumping power from 0 to 70 mW, the basic phase shift θ in (4-15) is changed from -30° to +90°, the spectral response is shifted by 120 MHz, corresponding to a tunability of 33%. For comparison, the simulated frequency responses are also shown in Fig. 4.36 as dashed lines. Again, a good agreement is reached between the experimental and the simulated results. Since the phase relationship is always maintained during the pumping, the spectral shape is maintained unchanged during the tuning process. It should be noted that since the Er/Yb co-doped fiber is pumped by the 980-nm LD, it works like an optical amplifier. The gain provided by the pumped Er/Yb co-doped fiber is about 2 dB at a pumping power of 90 mW.

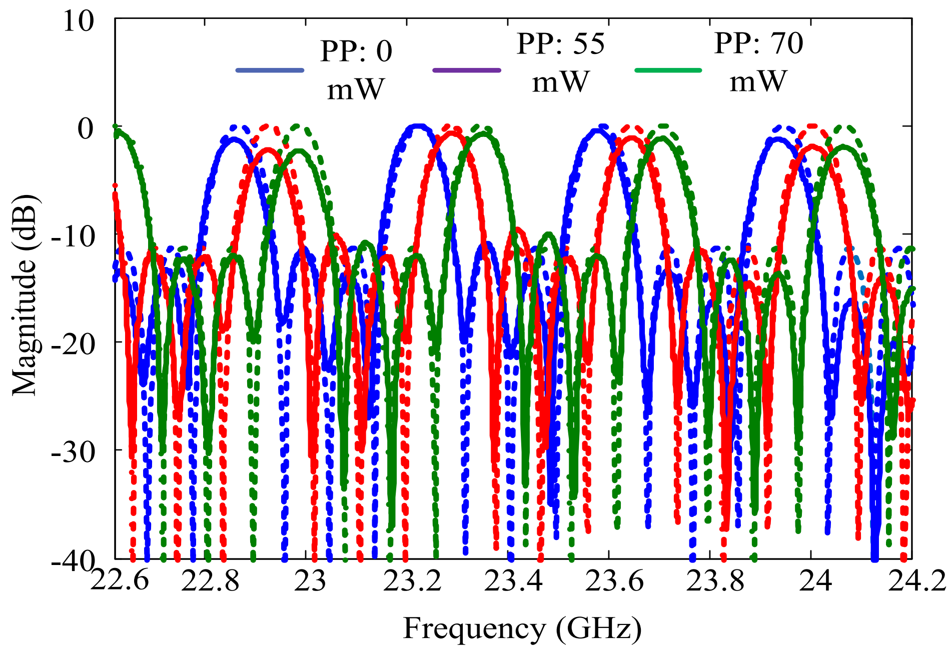

Fig. 4.36. Frequency response of the four-tap microwave photonic filter with complex coefficients at different pumping powers (solid lines). The dashed lines show the simulated frequency response corresponding to a basic phase shift of -30^o, +36^o, and +90^o. PP: pumping power.

In conclusion, a frequency-tunable multi-tap microwave photonic filter with complex coefficients based on a single TFBG in an Er/Yb co-doped fiber was proposed and experimentally demonstrated. It was discovered that resonance depths in the transmission spectrum of a TFBG are linearly changing and consequently the phase shifts are linearly changing. This feature ensures that the phase relationship in the tap coefficients is met if the optical carriers are placed in these resonances. The tunability of the filter was achieved by pumping the TFBG which was written in an Er/Yb co-doped fiber. An experiment was performed, and a three- and four-tap photonic microwave filter with a tuning range of 40% and 33% was achieved, respectively, by optically pumping the TFBG with a pumping power of 0 and 70 mW. During the tuning, the shape of the spectral response was maintained unchanged. By designing a TFBG with stronger coupling coefficients and a larger wavelength region with increasing or decreasing coupling coefficients, a microwave filter with more taps and lager tunable range could be implemented.

CHAPTER 5 SLOW AND FAST LIGHT BASED ON INTEGRATED RING RESONATORS

5.1. Mathematical model of ring resonators

An optical ring resonator consists of a loop waveguide and directional couplers or multi-mode interferometer (MMI) couplers to couple the light from the loop waveguide to the bus waveguides and inverse. Fig. 5.1 shows the schematic structures of two double-port microring resonators with a directional coupler and a MMI coupler.

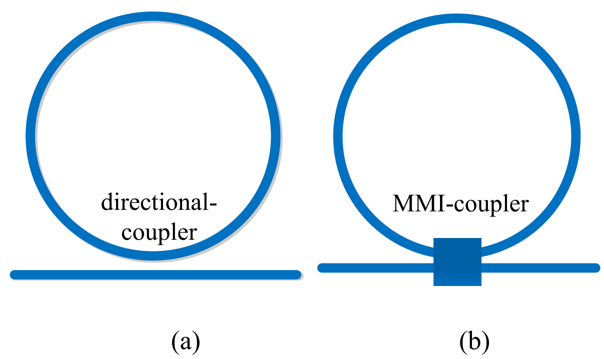

Fig. 5.1. The schematic structure of a two port microring resonator with a (a) directional coupler and (b) MMI-coupler.

The concepts behind optical ring resonators obey the rules behind the constructive interference and total internal reflection. The transfer of power between two port waveguides of a four port microring resonator is only possible at a specific wavelength at which constructive interference is satisfied. As can be seen in Fig. 5.2, an incoming light I_{in} propagates along one of the port waveguides of the ring resonator. In coupler 1, a small fraction of light ($\kappa_1^2 I_{in}$) is coupled into the resonator. However, most of the light continues its path to the through port as $I_{through}$. The light in the resonator (I_{cav1}) propagates along the resonator until it reaches coupler 2. Here a small fraction of light ($\kappa_2^2 I_{cav1}$) is coupled out of the resonator as I_{drop}. However, the large fraction of light (I_{cav2}) continues its round-trip to coupler1. If the phase of I_{cav2} as it interferes with the light I_{in} at coupler1 satisfies the resonance condition, constructive interference will occur at the resonator side of the first coupler, resulting in a net increase of I_{cav1}. At the same time destructive interference at the port waveguide side results in a decrease of the power $I_{through}$. Transferring power from I_{in} will repeat many times as I_{cav2} has constructive interference with I_{in}. At a certain power level, power cannot be transferred from I_{in} any more, and the ring resonator is working in a steady state condition. In this condition, the power in the through port $I_{through}$ is at the lowest level while the power in the drop port is at the highest level. Thus, the power has been transformed from the input to the drop port.

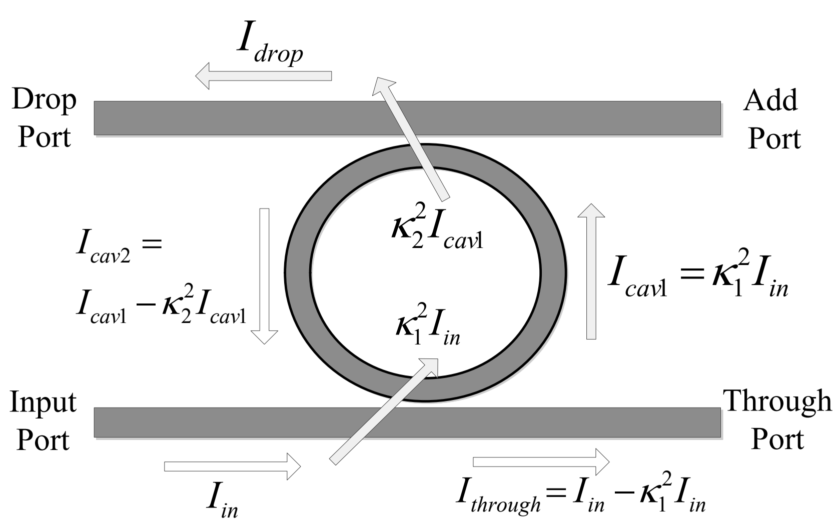

Fig. 5.2. Light coupling in a four-port microring resonator.

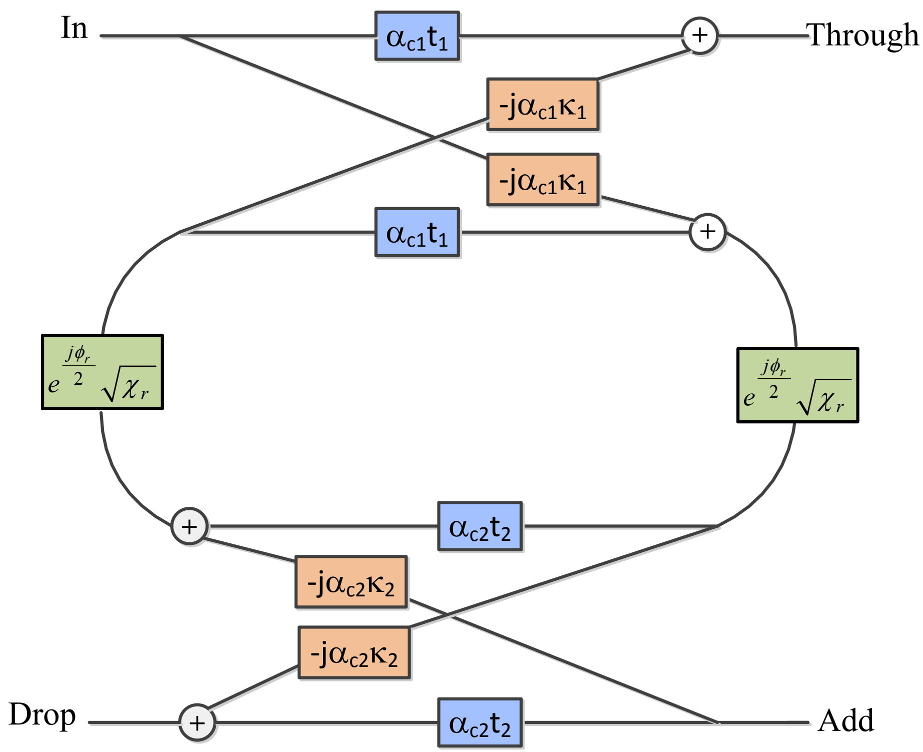

Fig. 5.3. The mathematical model of a four-port ring resonator.

The mathematical model of a four-port ring resonator is shown in Fig. 5.3 [187, 188]. The transfer matrix for symmetric couplers can be described as

$$M = \alpha_c \begin{bmatrix} t & -j\kappa \\ -j\kappa & t \end{bmatrix}, \tag{5-1}$$

where κ^2 and t^2 describes the power splitting of the couplers, which satisfy $\kappa^2 + t^2 = 1$. In fig. 5.3, φ_r is the round-trip phase, and α_r is the round-trip loss factor inside the ring. The round-trip phase of a ring resonator with radius R and group index of n_g can be defined as

$$\varphi_r = \frac{(2\pi)^2}{\lambda_0} \cdot R \cdot n_g\,. \tag{5-2}$$

Since the resonance condition is $\varphi_r = 2m\pi$, the resonance wavelength can be derived out such as,

$$\lambda_m = \frac{2\pi}{m} \cdot R \cdot n_g \tag{5-3}$$

where m is the mode number of the ring resonator.

The mathematical model can be used to find the spectral behavior of the microring resonator and serves as the basis model to find out the behavior of the complicated structures. As an example, the through response of the microring is derived in this section by using this mathematical model. By using Fig. 5.3 and identifying the direct path from the In port to the Through port, the model in Fig. 5.3 is simplified to the model shown in Fig. 5.4.

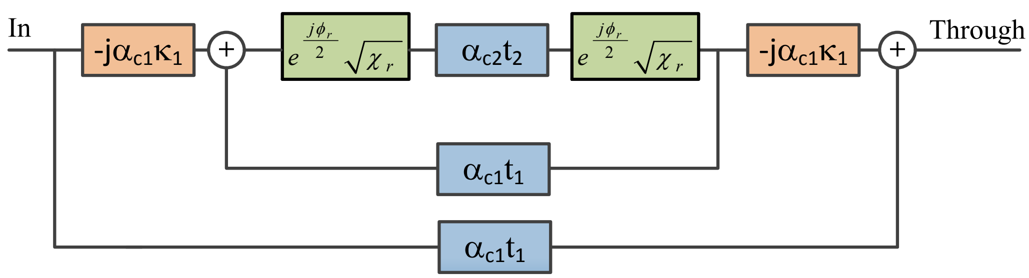

Fig. 5.4. Simplified ring resonator model used to obtain the through response.

By using the Mason's rule, the transfer function is

$$\frac{E_{Through}}{E_{In}} = \alpha_{c1} \frac{t_1 - t_2 \cdot \alpha \cdot e^{j\phi_r}}{1 - t_1 t_2 \cdot \alpha \cdot e^{j\phi_r}} \tag{5-4}$$

where, $\alpha = \alpha_{c1} \cdot \alpha_{c2} \cdot \alpha_r$. By using (5-4) the power in the through port is given by

$$\frac{P_{Through}}{P_{In}} = \alpha_{c1}^2 \frac{t_1^2 - 2\alpha \cdot t_1 \cdot t_2 \cdot \cos(\varphi_r) + \alpha^2 \cdot t_2^2}{1 - 2\alpha \cdot t_1 t_2 \cdot \cos(\varphi_r) + \alpha^2 \cdot t_1^2 t_2^2}. \tag{5-5}$$

The through response of a microring resonator with $R = 40\mu m$, $t_1 = t_2 = 0.8$, $\alpha_r = 0.95$, $\alpha_{c1} = 1$, and $n_g = 3.59$ is calculated based on (5-5) and is shown in Fig. 5.5.

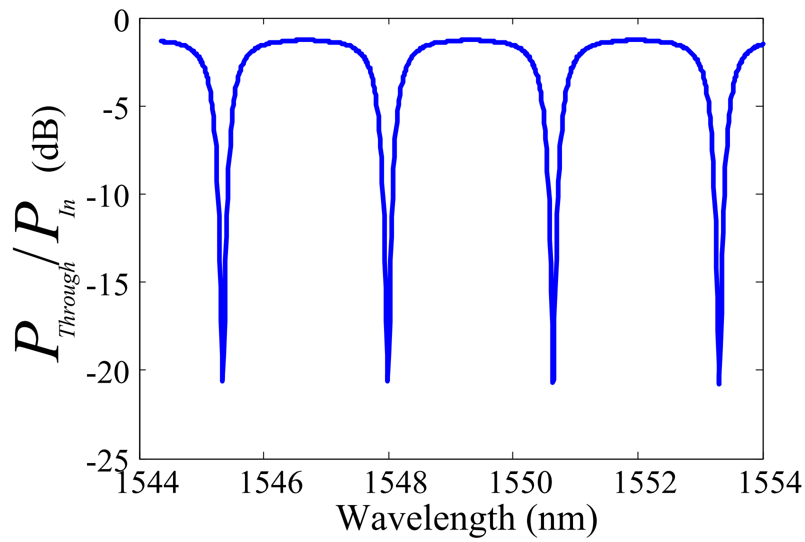

Fig. 5.5. The through response of a microring resonator.

5.2. Continuously tunable slow and fast light in a MRR with MMI couplers

In this section, we propose a technique to generate all-optically tunable slow and fast light based on a silicon-on-insulator (SOI) MRR incorporating multi-mode interference (MMI) couplers. The tuning is achieved by controlling the polarization of the input light wave. The key feature of an SOI MRR is that the self-coupling coefficient and the loss factor are polarization dependent which are used to tune the time delay or time advance. In the MRR, the MMI couplers are optimized for the TM (transverse-magnetic) mode. The self-coupling coefficient of the MRR is reduced if the input polarization state is tuned away from the direction that is aligned with the TM mode. Moreover, the loss factor of the MRR is intrinsically polarization dependent. By changing the self-coupling coefficient and the loss factor, the characteristics of the resonance notch, including its depth and width, are changed, which leads to the change of the phase (φ) inside the resonance. The group delay ($d\varphi/d\omega$) is correspondingly changed inside the resonance. In addition to the possibility of designing a MMI coupler to be optimized for the TM mode to achieve polarization-dependent time delay or advance tuning, another reason of using a MMI-coupler MRR in this proposal is that it has a larger resonance bandwidth compared with a directional coupler MRR [189].

5.2.1 Double-MMI coupler ring resonator

The schematic diagram of a double-MMI coupler MRR is shown in Fig. 5.6(a) and a picture of a fabricated double-MMI coupler MRR is shown in Fig. 5.6(b). The transmission power spectra at the through port of the MRR is expressed as,

$$|T|^2 = \alpha_{MMI1}^2 \left[\frac{t_1^2 - 2\alpha t_1 t_2 \cos\theta + \alpha^2 t_2^2}{1 - 2\alpha t_1 t_2 \cos\theta + \alpha^2 t_1^2 t_2^2} \right] \tag{5-6}$$

where t_1 and t_2 are the self-coupling coefficients of the through port coupler (coupler 1) and the drop port coupler (coupler 2), respectively, L is the length of the ring cavity, $\theta = 2\pi n_{eff} L / \lambda$ is the total round trip phase accumulation, $\alpha = \alpha_{MMI1} \cdot \alpha_{MMI2} \cdot \alpha_{ring}$ is the combined loss factor including the ring propagation loss factor (α_{ring}) and the two coupler loss factors ($\alpha_{MMI1}, \alpha_{MMI2}$), n_{eff} is the waveguide effective index, and λ is the wavelength in vacuum.

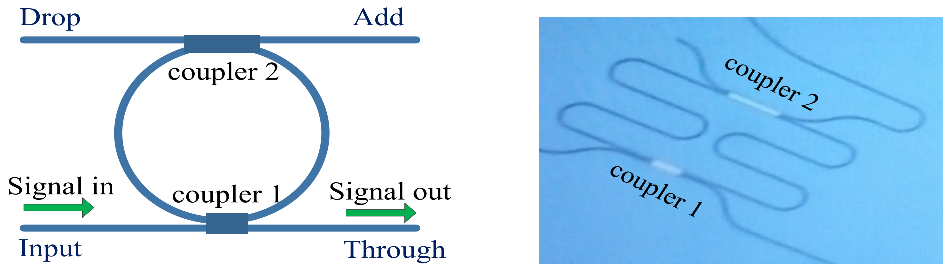

(a) (b)

Fig. 5.6. (a) The schematic diagram of a double-MMI coupler MRR. (b) The picture of the fabricated double-MMI coupler MRR.

An MRR has multiple resonances. If a light wave is located in the bandwidth of a resonance, a time delay ($d\phi/d\omega > 0$) or time advance ($d\phi/d\omega < 0$) would be produced depending on the slope of the phase response. The group delay can be expressed as

$$\tau = \frac{d\phi}{d\omega}. \tag{5-7}$$

By designing the MMI coupler to be optimized for the TM mode coupling, the self-coupling coefficient would be strongly polarization dependent and would decrease by changing the polarization state from a TM to a TE mode. In our designed double-MMI coupler MRR, coupler 1 has a 50:50 splitting ratio while coupler 2 has an 85:15 splitting ratio. The MMI couplers are optimized for the TM mode coupling. By changing the polarization state from a TM to TE mode, the self-coupling coefficients are changed significantly, and the loss factor α is also changed. At the designed central wavelength of the MMI coupler (1550 nm), the coupling coefficients and the loss factor are expected to decrease when the input polarization is rotated from TM to TE. Based on our calculation, at an operating wavelength of 1542.5 nm, t_1, t_2 and α are also decreased by changing the polarization state from a TM to TE mode. Fig. 5.7 shows the transmission, phase, and group delay spectra of an MRR with the ring cavity having a length of 350 μm, when the input polarization is changed from a TM to TE mode. In this case, self-coupling coefficient t_1 is decreased from 0.56 to 0.48, t_2 is decreased from 0.92 to 0.72, and the loss factor α is decreased from 0.83 to 0.74. As can be seen from Fig. 5.7(a), the depth and the bandwidth of the resonance are changed, which lead to the change in the slope of the phase response, as shown in Fig. 5.7(b), and correspondingly the group delay is changed, as shown in Fig. 5.7(c). It should be noted that the coupling regime for all cases here is the over-coupled regime. Therefore, the phase slope ($d\phi/d\omega$) is positive. Thus, only a tunable slow light is generated with the tuning done by tuning the polarization state of the input light in a double-MMI coupler MRR.

An experiment is done to demonstrate the proposed schemes. The setup of the experiment is shown in Fig. 5.8. A continuous wave (CW) light from a tunable laser source (TLS) is sent to a Mach-Zehnder modulator (MZM) via a polarization controller (PC1). At the MZM the light is modulated by a Gaussian pulse. The Gaussian pulse has a temporal width of 50 ps (13.5 GHz) which is generated by a signal generator. The modulated signal is amplified by an erbium-doped fiber amplifier (EDFA), and its polarization state is tuned by using a second polarization controller (PC2). The light is coupled into and out of the MRR by two tapered fibers. The output light from the MRR is detected at a 53 GHz photodetector (PD) and the waveform is observed by a sampling oscilloscope (OSC, Agilent 86100C). In order to measure the time delay or advance, a reference waveform that is not time delayed or advanced is used as a comparison. In the experiment, the reference waveform is the output pulse when the wavelength of the TLS is placed out of the resonance spectrum, thus the signal would not experience a time delay or advance caused by the resonance.

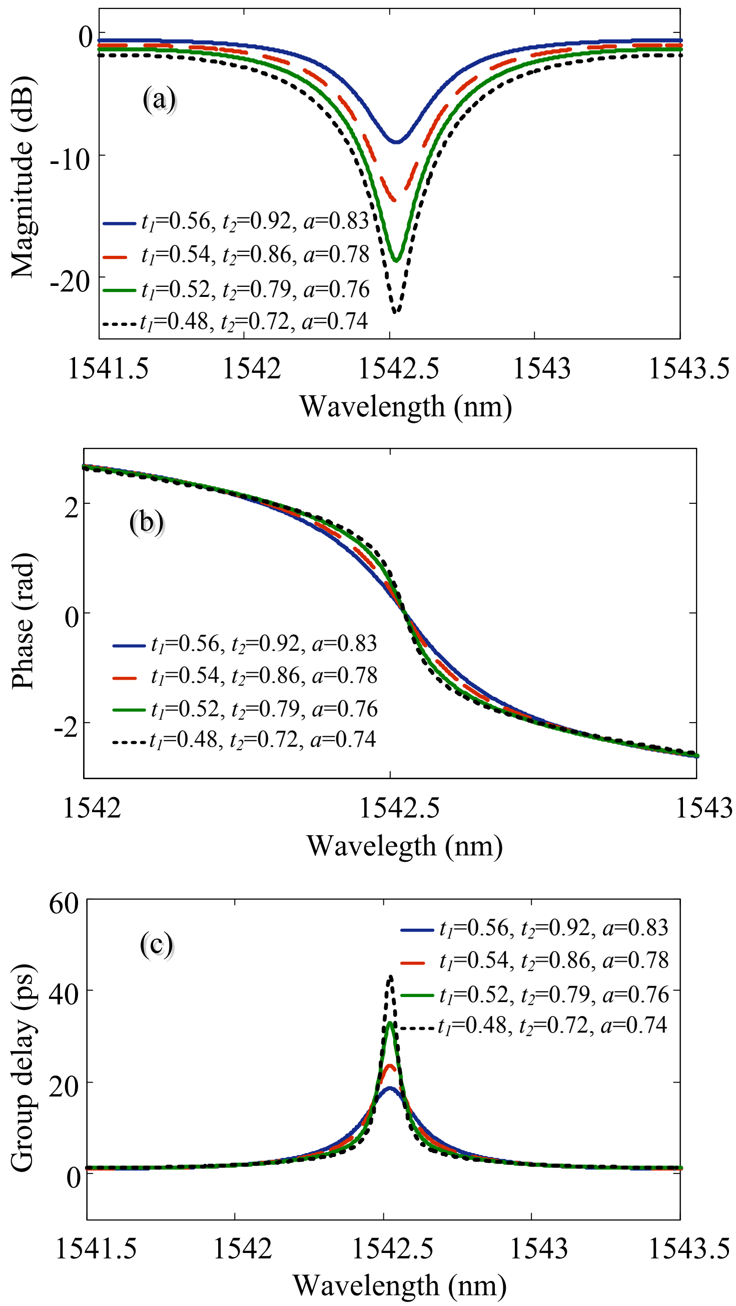

Fig. 5.7. The simulation results for a double-MMI coupler MRR (a) The magnitude (b) phase, and (c) group delay responses when the polarization state of the input light is changed from a TM to a TE mode.

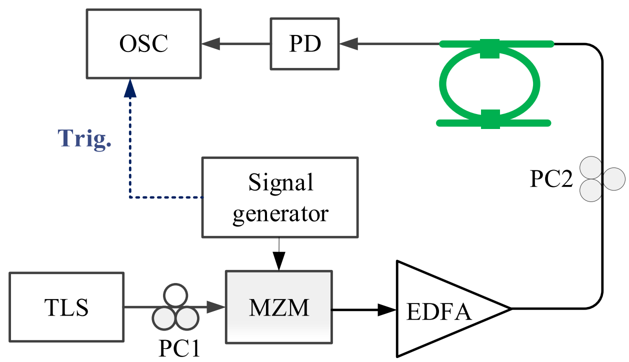

Fig. 5.6. Experimental setup. TLS: tunable laser source, MZM: Mach-Zehnder modulator, EDFA: erbium-doped fiber amplifier, Pol: polarizer, PC: polarization controller, PD: photodetector, OSC: oscilloscope.

A double-MMI coupler MRR is fabricated on a SOI wafer with a 260 nm thick silicon layer on a 2 μm thick BOX layer. Ring and the bus waveguides are patterned on the wafer by e-beam lithography. The cross section of the ring and the bus waveguides is 450 nm (width) × 260 nm (height). The cavity length is 350 μm. The upper cladding of the MRR is a layer of SU8 polymer. The through port and drop port MMI couplers have a length and width of 3 μm × 8.5 μm and 2 μm × 15 μm, respectively. The edge to edge separation of the input/output waveguides in the two MMI couplers is 550 nm. The picture of the fabricated double-MMI coupled MRR is shown in Fig. 5.6(b). Based on our measurements at the wavelength of 1542.5 nm, t_1, t_2 and α are decreased by changing the input pulse from a TM to TE mode. Fig. 5.9(i-a) shows the measured transmission spectrum of the fabricated MRR (solid line) around a resonance centered at 1542.5 nm. The measured phase response of the MRR around the resonance is shown in Fig. 5.9(i-b). The simulated magnitude and phase responses are also shown as dashed lines for comparison. The parameters of the MRR used in the simulations are $t_1 = 0.53$, $t_2 = 0.85$ and $\alpha = 0.81$. Fig. 5.9(ii-a) and (ii-b) shows the measured (solid line) and simulated (dashed line) magnitude and phase responses of the same ring resonator but for an input light at a different input polarization state. The parameters for the MMI coupler used in the simulations are changed to $t_1 = 0.51$ $t_2 = 0.77$ and $\alpha = 0.78$.

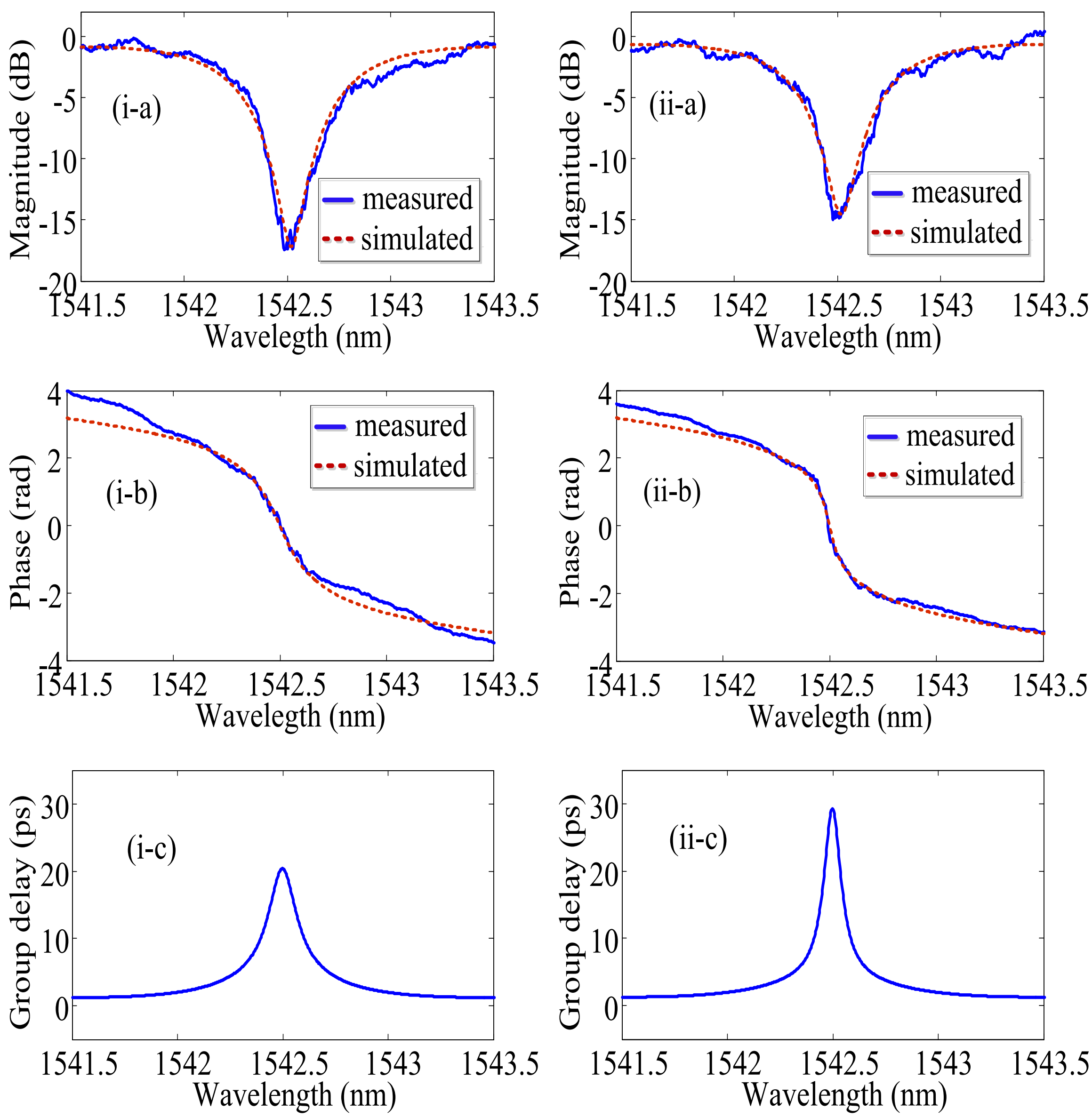

Fig. 5.7. The measured (solid lines) and simulated (dashed lines) (a) magnitude and (b) phase responses of the fabricated double-MMI coupler MRR at two different polarization states of (i) and (ii). (c) The simulated group delay responses at the two polarization sates.

It should be noted that the measured phase responses are achieved by using a vertical network analyzer (VNA). In fact, the VNA measures the phase of the device under test which includes fiber, waveguide, ring and the PC. However, the simulated phase response is in fact, the phase response of a single ring. Therefore, the amount of the phase jump at the resonance wavelength should be considered for the comparison. Fig. 9(c) shows the simulated group delays for these two different input polarization states. It can be seen that by changing the polarization state, the resonance shape is changed, the phase shift at the resonance wavelength is changed and correspondingly different groups delays at the resonance wavelength are achieved which can be used to demonstrate a tunable slow light. By incorporating the fabricated MRR in the experimental setup in Fig. 5.8, and applying a 13.5 GHz Gaussian pulse that is modulated on a light at 1542.5 nm to the MRR, a time delayed Gaussian pulse is generated with the amount of time delay depending on the input polarization. As shown in Fig. 5.10, for three different polarization states, three different time delays are obtained. A maximum time delay of 35 ps is achieved with no visible distortions to the time-delayed pulse.

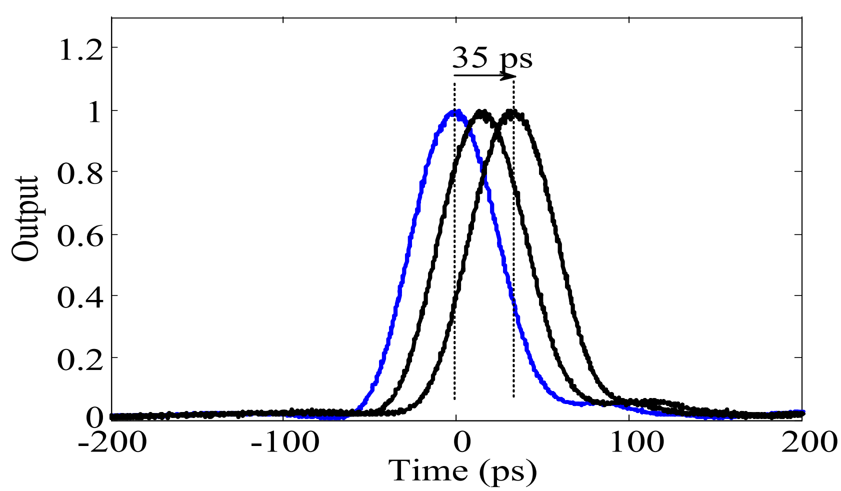

Fig. 5.8. The time delayed (slow light) Gaussian pulses by tuning the input light polarization state in the double-MMI coupler MRR.

5.2.2 Single-MMI coupler ring resonator

The schematic diagram of a single-MMI coupler MRR is shown in Fig. 5.11(a) and a picture of a fabricated single-MMI coupler MRR is shown in Fig. 5.11(b). The transmission spectrum of a single-MMI coupler MRR depends on the self-coupling coefficient (t) of the MMI coupler and also on the loss factor ($\alpha = \alpha_r \cdot \alpha_{MMI}$) which is the combination of the MMI coupler loss factor (α_{MMI}) and the round-trip ring propagation loss factor (α). The transmission spectrum of the MRR can be expressed as,

$$T = \alpha_{MMI}\left[\frac{t-\alpha e^{j\theta}}{1-\alpha t e^{j\theta}}\right]. \tag{5-8}$$

In our designed single-MMI coupler MRR, the MMI coupler has an 85:15 splitting ratio for the TM mode and is optimized for the TM mode coupling. Therefore, it is strongly polarization dependent and would decrease by changing the polarization state from a TM to TE mode. At the designed central wavelength of the MMI coupler (1550 nm), t and α are expected to decrease when the input polarization is rotated from TM to TE. However, in a small selected wavelength range away from the central wavelength, t can be decreased while α is increased which is the case at our selected operating wavelength of 1558.06 nm. Fig. 4 shows the transmission, phase, and group delay spectra of an MRR with the ring cavity having a length of 340 μm, when the input polarization is changed from a TM to TE mode. In this case, the self-coupling t is decreased from 0.87 to 0.63, and the loss factor α is increased from 0.71 to 0.82. As can be seen from Fig. 5.12(a) the depth and bandwidth of the resonance are changed, which leads to the change in the slop of the phase response, as shown in Fig. 5.12(b), and correspondingly the group delay is changed, as shown in Fig. 5.12(c). As can be seen in Fig. 5.12(b), by changing the input polarization from a TM to TE mode, not only the phase is changed but also its slope sign is changed. When $t > \alpha$, $d\phi/d\omega$ is negative thus the group delay is negative and fast light can be achieved, and when $t < \alpha$, $d\phi/d\omega$ is positive thus the group delay is positive and slow light can be achieved. It should be noted that the coupling in this MRR can be in the under-coupled, critically-coupled, and over-couple regimes. Therefore by changing the input light polarization state, continuous slow and fast light can be achieved in a single-MMI coupler MRR.

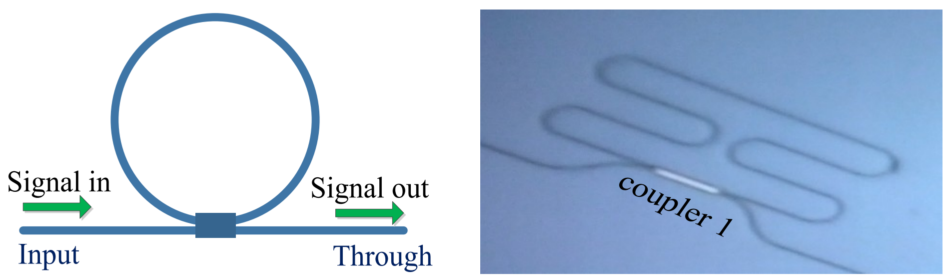

(a) (b)

Fig. 5.9. (a) The schematic diagram of a single-MMI coupler MRR. (b) The picture of the fabricated single-MMI coupler MRR.

It should be noted that there are two differences between the single-MMI coupler MRR and the double-MMI coupler MRR. The first difference is that only a tunable slow light can be achieved in the double-MMI coupler MRR by changing the input polarization state while a tunable slow and fast light can be achieved by using a single-MMI coupler MRR since its coupling regime changes by changing the input polarization. The other difference is that their resonance bandwidths are different. Fig. 5.13 shows the simulation of the magnitude response, and group delay of the two types of MRRs. The loss factors are assumed to be the same in both MRRs and the two MMI couplers optimized for TM mode coupling are assumed to be identical in both MRRs. As can be seen the resonance bandwidth of the single-MMI coupler MRR is 50% narrower than that of the double-MMI coupler. Therefore, the amount of the distortion for a delayed signal with a fixed bandwidth in the double-MMI coupler MRR is less, and a double-MMI coupler MRR is more suitable for achieve a time delay for an optical signal with a wider bandwidth. However, as can be seen in Fig. 5.13(b) the amount of the time advance achieved by the double-MMI coupler MRR is less than that achieved by a single-MMI coupler MRR.

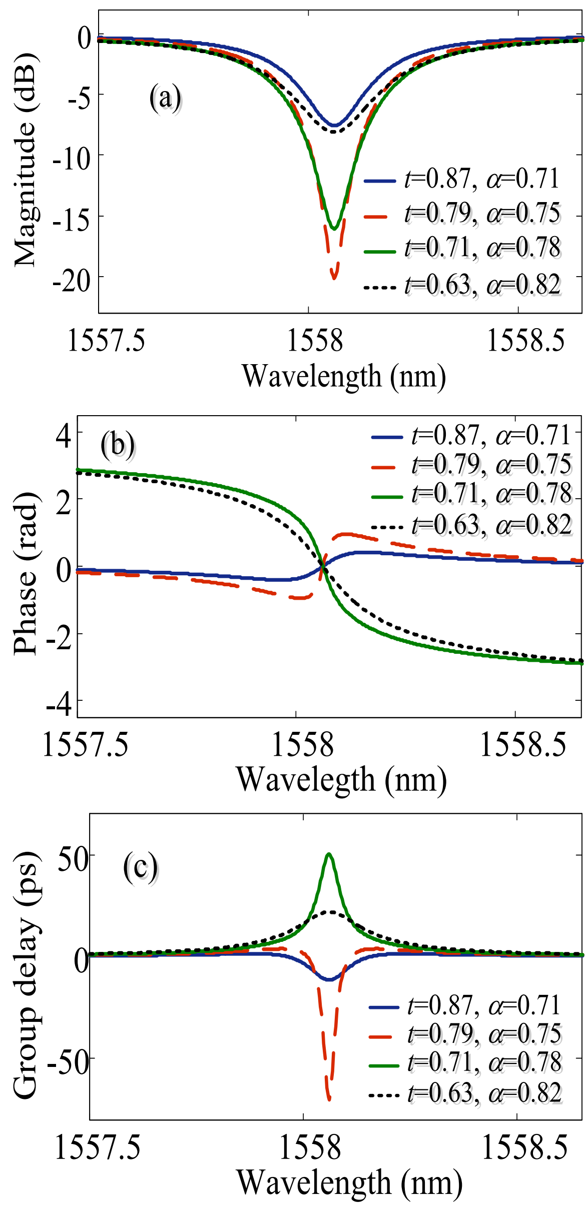

Fig. 5.10. The simulated (a) magnitude, (b) phase, and (c) group delay responses of a single-MMI coupler MRR with α=0.72 and t= 0.82, 0.77, 0.67, and 0.62.

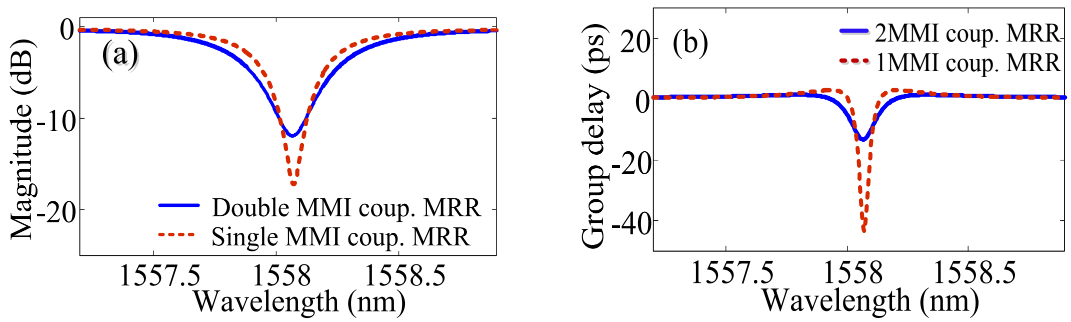

Fig. 5.13 Simulated (a) normalized magnitude and (b) group delay responses of a double-MMI coupler MRR (solid line) and a single MMI coupler MRR (dashed line).

A single-MMI coupler MRR is fabricated on an SOI wafer with a 260 nm thick silicon layer on a 2 μm thick BOX layer. The length and width of the MMI coupler is 2 μm × 15 μm, and the cavity length is 340 μm. The picture of the fabricated single-MMI coupled MRR is shown in Fig. 3(b). Based on our measurements at the wavelength around 1558.06 nm, t is decreased and α is increased by changing the input pulse from a TM to TE mode. Fig. 5.14(i-a) shows the measured transmission spectrum of the fabricated MRR (solid line). The measured phase response of the MRR around the resonance is shown in Fig. 5.14(i-b). The simulated magnitude and phase responses are also shown as dashed lines for comparison. The parameters of the MMI coupler used in the simulations are $t = 0.79$ and $\alpha = 0.745$. Fig. 5.14(ii-a) and (ii-b) shows the measured (solid line) and simulated (dashed line) magnitude and phase responses of the same ring resonator but for an input light at a different input polarization state. The parameters for the MMI coupler used in the simulations are changed to $t = 0.68$ and $\alpha = 0.8$. Fig. 5.14(c) shows the simulated group delays for these two different input polarization states. As can be seen by changing the input light polarization state, the resonance shape is changed and correspondingly the phase shift is changed. Note that in Fig. 5.14(b), not only the phase shift is changed but also the slope sign ($d\phi/d\omega$) is changed from negative to positive. Therefore, the group delay is changed from negative to positive and a tunable slow-to-fast light is generated. By using this MRR in the experimental setup in Fig. 5.8, with a 13.5 GHz Gaussian pulse modulated on an optical carrier at 1558.06 nm, and changing the polarization state continuously, a tunable slow-to-fast light is generated. The delayed and advanced Gaussian pulses for five different polarization states are shown in Fig. 5.15. As can be seen a fast light with a maximum time advance of 54 ps is changed to a slow light with a maximum time delay of 48 ps. Therefore, a 102 ps tunable slow-to-fast light is achieved. As discussed in Section II, the amount of distortion in this MRR is more than the double-MMI coupler MRR which is noticeable by comparing Fig. 5.10 and Fig. 5.15.

In conclusion, an approach to generating a tunable slow and fast light using a MRR incorporating polarization-dependent MMI couplers were proposed and demonstrated experimentally. The tuning was achieved by tuning the input light polarization state since the MMI couplers were designed to be optimized for the TM mode. Two MRRs with one having double MMI couplers and the other having a single MMI coupler were fabricated and the use of the MRRs to generate a slow light and a slow-to-fast light was studied. By changing the input light polarization state from a TM to a TE mode, a tunable slow light with a time delay of 35 ps was achieved experimentally using the double-MMI coupler MRR, and a 102 ps tunable slow-to-fast light was achieved using the single-MMI coupler MRR. Since the bandwidth of a single-MMI coupler MRR is intrinsically narrower than that of a double-MMI coupler MRR, there was a greater distortion in the time delayed pulses by the a single-MMI coupler MRR.

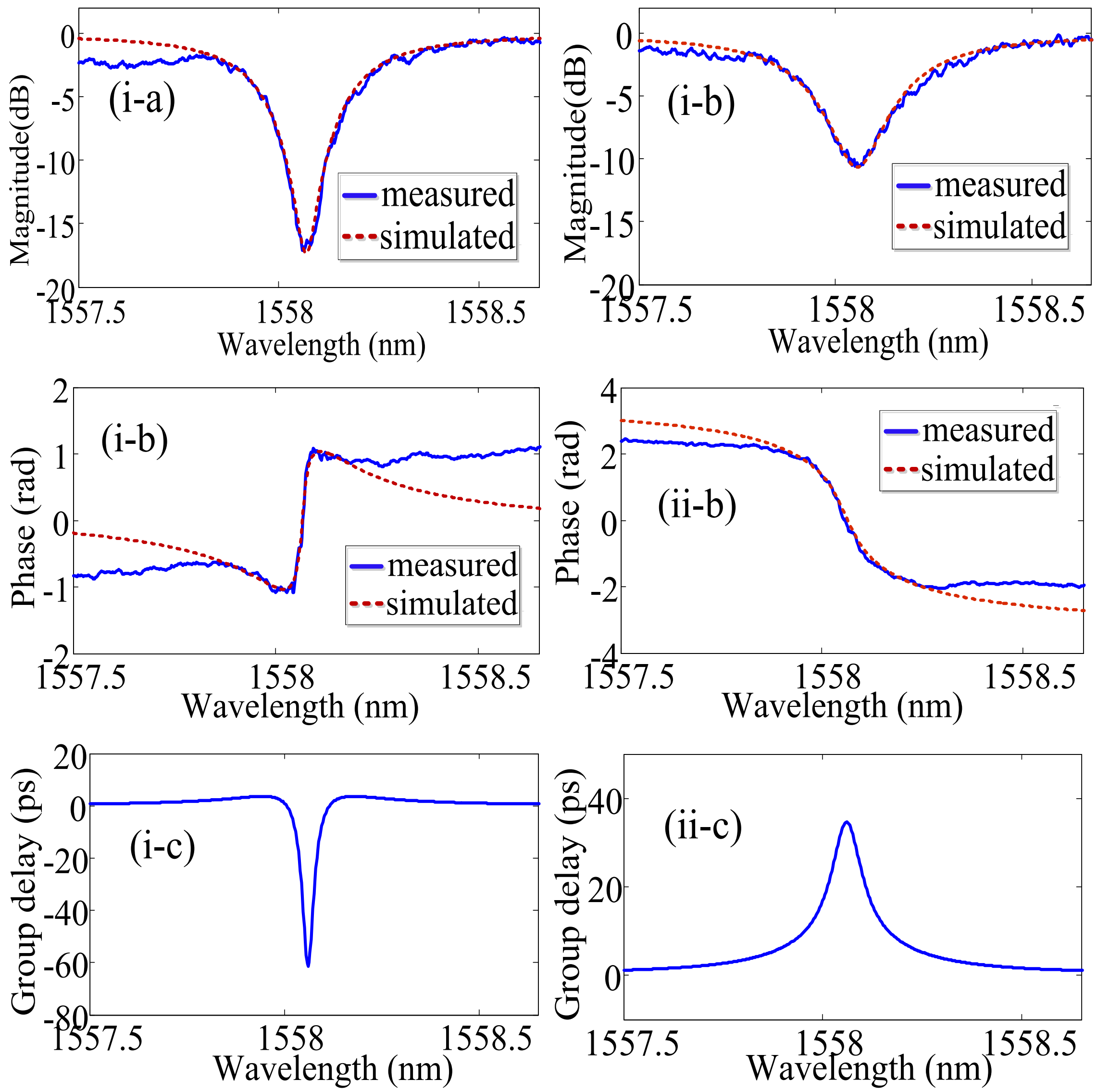

Fig. 5.14. The measured (solid lines) and simulated (dashed lines) (a) magnitude, and (b) phase responses of the fabricated single-MMI coupler MRR at two different polarization states of (i) and (ii). (c) The simulated group delay responses at the two polarization sates.

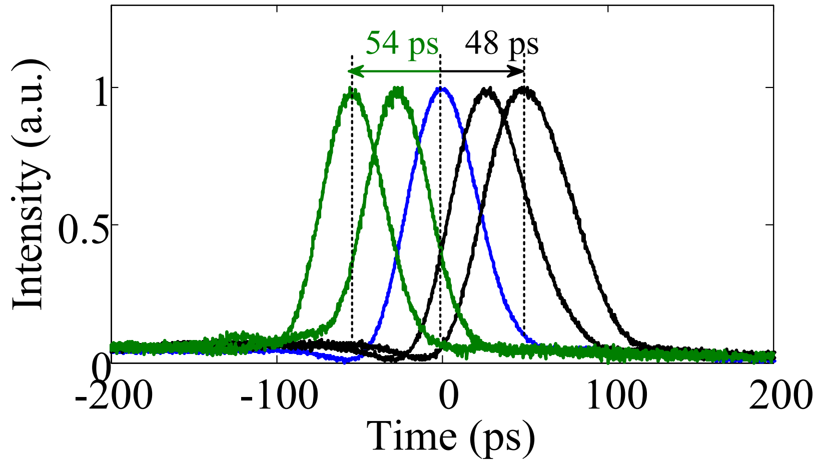

Fig. 5.15. The time delayed (slow light) and advanced (fast light) Gaussian pulses by tuning the input light polarization state in a single-MMI coupler MRR.

APPLICATIONS OF MRR-BASED SLOW AND FAST LIGHT IN MICROWAVE PHOTONICS

6.1. Continuously tunable fractional order differentiator

We propose and demonstrate a tunable fractional order differentiator implemented based on silicon-on-insulator (SOI) MRR with a MMI coupler. Since the resonator is fabricated on a silicon chip, the size is small and the stability is significantly improved. The MMI coupler is optimized for the TM (transverse-magnetic) mode, thus by changing the input polarization state, the self-coupling coefficient is changed and correspondingly, the coupling regime is changed. The coupling regime can be tuned from the over-coupled regime to the under-coupled regime, which leads to the change of the phase shift at the resonance wavelength. This tunable phase shift (nπ) can be used to implement an nth-order all-optical temporal differentiator with the order fully tunable from 0 to 2. The effect of the tunable self-coupling coefficient and the loss factor on the coupling regime and correspondingly on the resonance and the phase shift in the resonance is studied by simulations. A fractional order temporal differentiator based on a microring resonator is studied theoretically and demonstrated experimentally. A Gaussian pulse with a bandwidth of 45 GHz is temporally differentiated with a tunable differentiation order at 0.37, 0.67, 1, 1.2, and 1.3.

An nth-order temporal differentiator provides nth order time derivative of the complex envelope of an input signal $x(t)$, $dx^n(t)/dt^n$. The differentiator can be considered as an optical filter with a frequency response given by

$$H_n(\omega) = \left[j(\omega - \omega_0) \right]^n = \begin{cases} e^{jn\left(\frac{\pi}{2}\right)} \left| (\omega - \omega_0) \right|^n & \omega > \omega_0 \\ e^{jn\left(-\frac{\pi}{2}\right)} \left| (\omega - \omega_0) \right|^n & \omega < \omega_0 \end{cases} . \tag{6-1}$$

As can be seen an nth-order temporal differentiator can be implemented using an optical filter that has a magnitude response of $\left|(\omega-\omega_0)\right|^n$ and a phase jump of nπ at ω_0. An optical filter with a frequency response given by (6-1) can be implemented using a MMI-coupled MRR. A schematic of a MMI-coupled MRR is illustrated in Fig. 6.1(a). The power splitting ratio to port 1 (t^2) and port 2 (K^2) are governed by $t^2 + \kappa^2 = 1$, as indicated in Fig. 6.1(b).

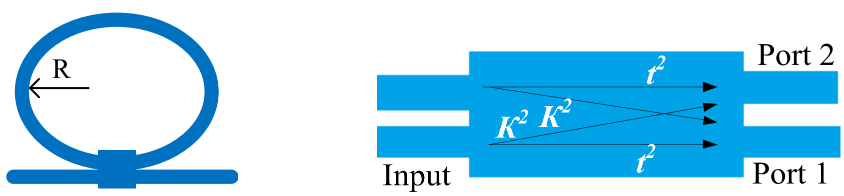

(a) (b)

Fig. 0.1. (a) Microring resonator with a MMI coupler, (b) a close-up view of the MMI coupler.

Mathematically, the frequency response of a MMI-coupled MRR can be expressed as

$$T = \alpha_{MMI} \left[\frac{t - \alpha e^{j\varphi_r}}{1 - \alpha t e^{j\varphi_r}} \right] \tag{6-2}$$

where $\varphi_r = 2\pi n_{eff} L / \lambda$ is the total round-trip phase accumulation, L is the ring cavity length, $\alpha = \alpha_{MMI} \cdot \alpha_r$ is the combined power loss factor including both the round-trip propagation loss factor α_r and the coupler loss factor α_{MMI}, n_{eff} is the waveguide effective index, and λ is the wavelength in vacuum. Thus, the power transmission is given by

$$\left|T\right|^2 = \alpha_{MMI}^2 \left[\frac{\alpha^2 - 2\alpha t \cos\varphi_r + t^2}{1 - 2\alpha t \cos\varphi_r + \alpha^2 t^2} \right]. \tag{6-3}$$

The effect of changing the self-coupling coefficient and the loss factor on the phase change in the resonance wavelength are studied by simulations. The MMI coupler in the SOI microring resonator is optimized for TM mode coupling. By changing the input polarization from a TM to a TE (transverse electric) mode, the self-coupling coefficient is decreased, and the total loss factor is increased in the designed ring at the operating wavelength. Fig. 6.2(a) and (b) shows the impact of changing the polarization from a TM to a TE mode on the introduced phase shift at the resonance wavelength. The coupling coefficient is decreased from 0.83 to 0.71, and the loss factor is increased from 0.75 to 0.79. In fact, the phase change at the resonance wavelength is different for the TE and TM mode. If a pulse has a polarization state just in between, then the total phase change is a vector sum of the two phase terms. As can be seen in Fig. 6.2 a fully tunable phase shift ($n\pi$) is achieved at the center of the resonance, which can be used to implement an *n*th-fractional order all-optical differentiator with a tunable *n* between 0 and 2.

The use of the ring resonance to differentiate a Gaussian pulse with a temporal FWHM of 50 ps with different differentiation orders is also simulated. In this simulation the loss factor is fixed at 0.77 and the coupling coefficient is changed from 0.72 to 0.82. As can be seen in Fig. 6.3, by changing the coupling coefficient the phase change in the resonance wavelength is changed and correspondingly the differentiation order can be changed.

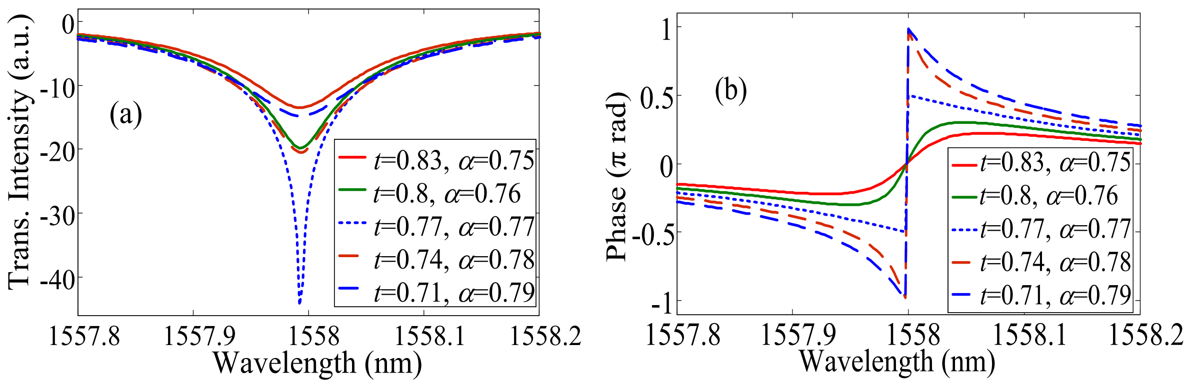

Fig. 0.2. Simulated transmission magnitude and the corresponding phase for t=0.83, 0.8, 0.77, 0.74, 0.71, and t=0.77, α =0.75, 0.76, 0.77, 0.78, 0.79.

A MMI-coupled SOI ring resonator is fabricated on a SOI wafer that has a 260 nm thick silicon layer on a 2 micron thick BOX layer. Waveguides of 450 nm wide were patterned by e-beam lithography and etched in an inductively coupled plasma (ICP) RIE system using C4F8/SF6 chemistry. Inverse tapers down to 150 nm in width were adopted at both the input and output facets to improve the waveguide to fiber coupling efficiency. The perimeter of the ring is 300 µm. The cross section of the ring and the bus waveguides is 450 nm x 260 nm. The upper cladding is a layer of SU8 polymer. The MMI coupler is 2 x 15 µm, and the edge separation of the input/output waveguides is 550 nm. Fig. 6.4 shows the measured transmission and phase spectra of the ring with a perimeter of 300 µm at a resonance wavelength of 1558 nm for two different input polarization states of (i) and (ii). As can be seen, the amount of phase change at the resonance wavelength is different for the two cases. To evaluate the impact of polarization change on the differentiation operation, a Gaussian pulse with a temporal FWHM of 22 ps is used as an input. The differentiated pulses by using the ring with the spectral responses shown in Fig. 6.4, are shown in Fig. 6.5. Two different differentiation orders of 1.85 for case (i) and 0.65 for case (ii), are achieved.

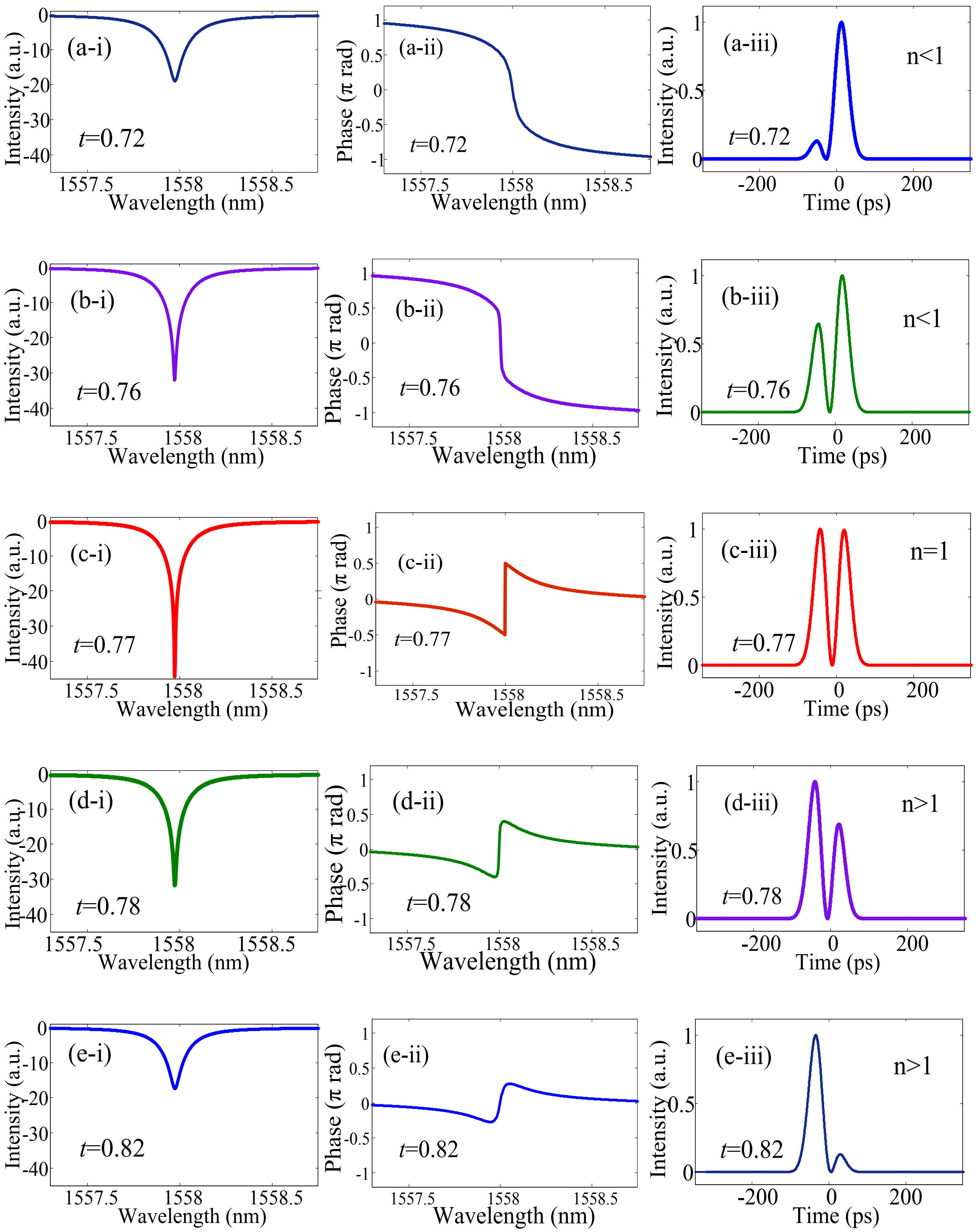

Fig. 0.3. Simulated transmission magnitude (i), phase response (ii), and the corresponding differentiated Gaussian pulse with temporal FWHM bandwidth of 50 ps (iii), for α =0.77, and (a) *t*=0.72*,* (b) *t*=0.76, (c) *t*=0.77*,* (d) *t*=0.78, and (e) *t*=0.82.

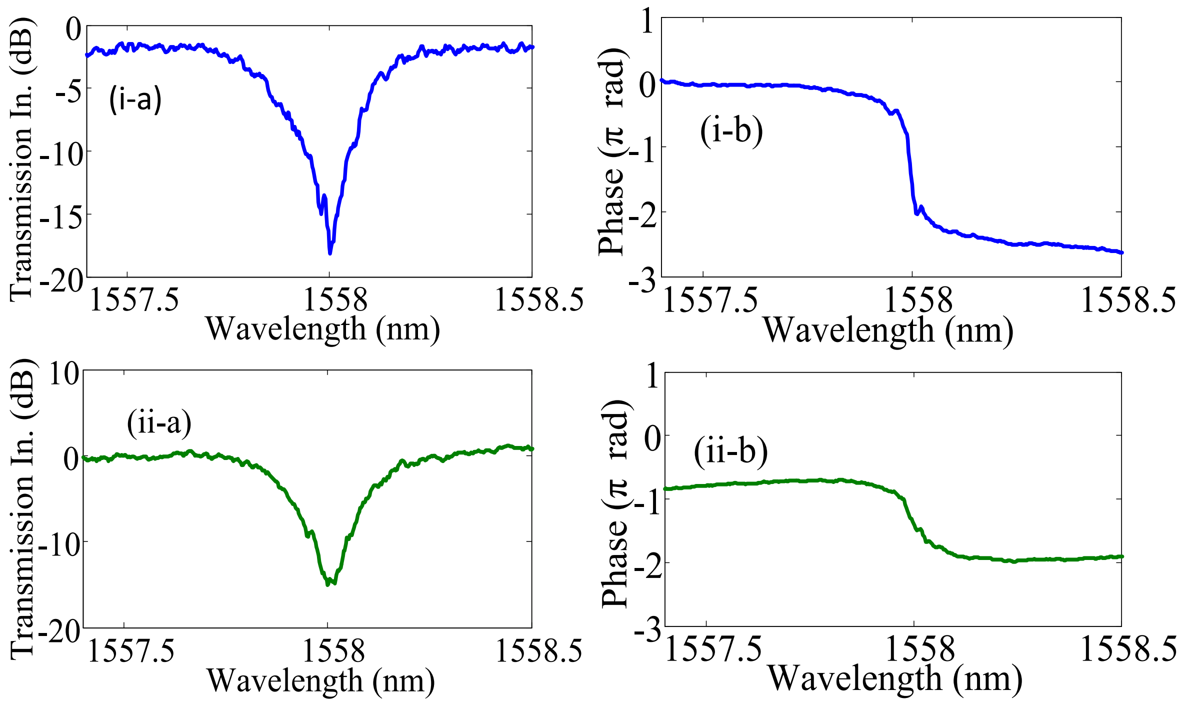

Fig. 0.4. The magnitude (a) and phase response (b) of the ring operating in transmission at 1558 nm for two different input polarization states, i and ii.

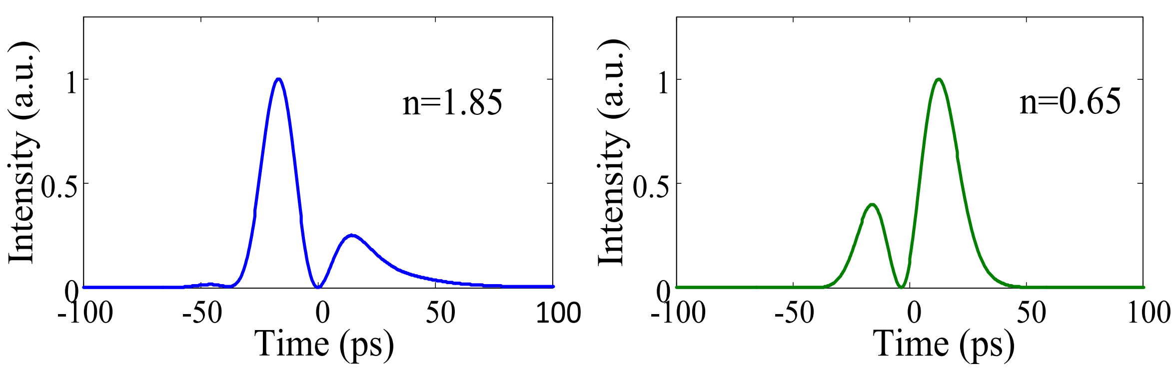

Fig. 0.5. The simulated differentiated pulses at two polarization sates by using the response spectra Fig. 6.4.

An experiment based on the setup shown in Fig. 6.6 is performed. A short Gaussian pulse with a temporal FWHM of 550 fs, centered at 1558.5 nm is generated by a mode locked laser (MLL). A WaveShaper is used to shape the Gaussian pulse to have a temporal FWHM of 22 ps (corresponding to a spectral width of 45 GHz) centered at 1558 nm. An erbium-doped fiber amplifier (EDFA) connected at the output of the WaveShaper is used to amplify the optical signal. A polarizer (Pol) is used to make the light from the EDFA linearly polarized, and a polarization controller (PC) connected to the Pol is to control and tune the polarization state of the input light to the ring. The light coupled into and out the bus waveguides of the ring is achieved by two tapered fibers. The differentiated signal is detected by a 53-GHz photodetector (PD) and its waveform is observed by a sampling oscilloscope (OSC).

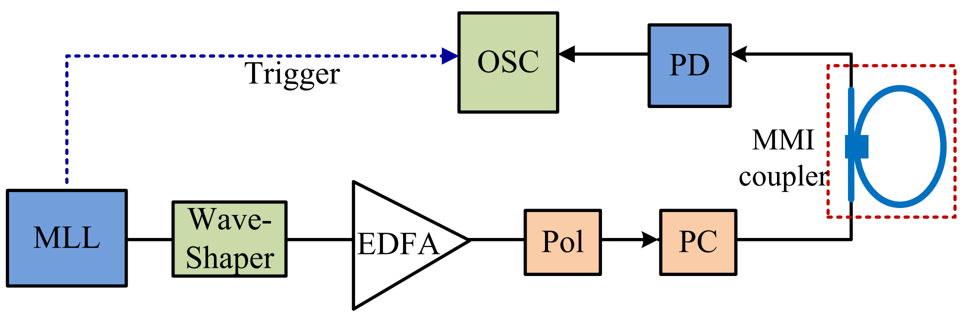

Fig. 0.6. Experimental setup. MML: mode lock laser. EDFA: Erbium doped fiber amplifier, Pol: Polarizer, PC: polarization controller, PD: photo-detector, and OSC: oscilloscope.

The shaped pulse at the output of the Waveshaper is shown in Fig. 6.7(a). An ideal Gaussian pulse with the same temporal width (22 ps) is also shown in Fig. 6.7(a) (dashed line) for comparison. As can be seen experimentally generated input pulse is close to a Gaussian except a slight deviation in the front tail. The polarization state of the input pulse is controlled by tuning the PC. The differentiated pulse is detected by the PD and the waveform is observed by the OSC. A differentiated pulse with the orders of n =1, 1.2, 1.5, 0.67, and 0.37 is generated and shown in Fig. 6.7(b), (c), (d), (e), and (f). Simulated pulses with an ideal input Gaussian pulse and an ideal differentiator with the same orders are also shown in Fig. 6.7 (b)-(f), as dashed lines. As can be seen a good agreement is achieved between the experimentally generated pulses and the pulses with an ideal differentiator. The root mean square error (RMSE) in the worst case (Fig. 6.7 (f)) is equal to 8%. It should be noted that the difference in the notch is caused mainly due to the limited bandwidth of the PD (53 GHz), and the difference in the tail part due to the non-ideal input Gaussian pulse, shown in Fig. 6.7(a).

By changing the polarization state, the round-trip phase accumulation for the TE and TM modes would be different because of different refractive indices. Correspondingly, the resonance wavelength would be shifted. Based on the experiment, for our used ring resonator, however, the resonance wavelength at 1558 nm was almost unchanged when changing the polarization. The largest change was less than 0.01 nm. This would change the differentiation order by 4% which is small and negligible. If the change of the resonance wavelength is large, the optical carrier of the signal to be differentiated should be tuned correspondingly, which may increase the tuning complexity. A simpler solution is to re-design the waveguide geometry to compensate the difference in the round-trip phase accumulation between TE and TM modes [190].

In conclusion, a silicon photonics based continuously tunable *n*th-order temporal differentiator was proposed and experimentally demonstrated. To the best of our knowledge, this is the first time that a ring-resonator-based temporal differentiator was implemented with a continuously tunable order. The key to achieve the differentiation order tuning was based on the tuning of the input polarization state, which led to the tuning of the phase shift. It was demonstrated that resonance phase shift could be tuned from 0.3π to $1.7\pi\, rad$, corresponding to a tunable fractional order from 0.3 to 1.7. The differentiation of a Gaussian pulse with a bandwidth of 45 GHz with different fractional orders was implemented.

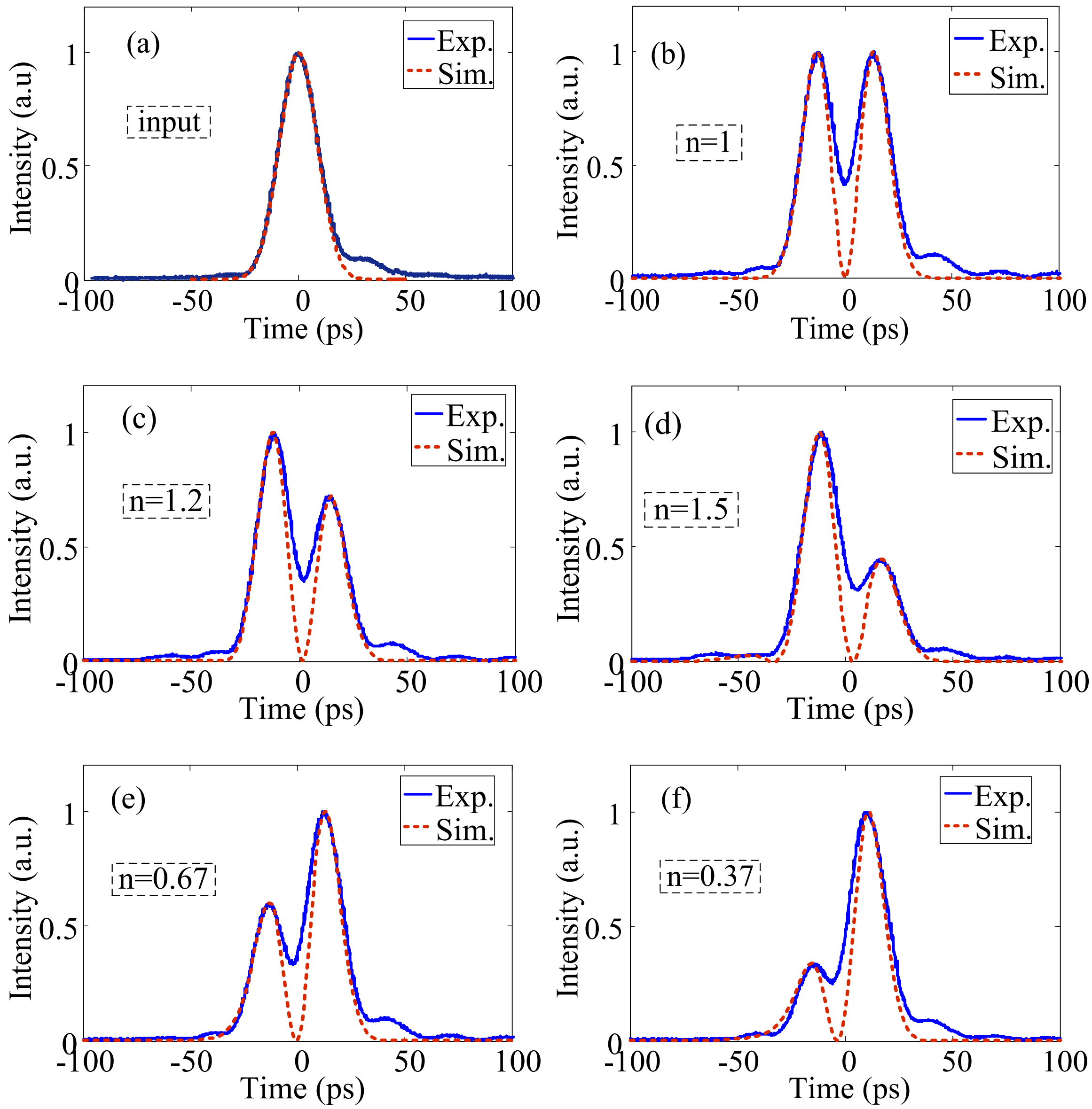

Fig. 0.7. (a) An input Gaussian pulse with an FWHM of 22 ps, and the differentiated pulses at the different input polarization states corresponding to differentiation orders of (b) n = 1, (c) n = 1.2, (c) n = 1.5, (e) n = 0.67, and (f) n = 0.37.

6.2. Continuously tunable fractional order Hilbert transformer

In this section, we propose a new method to implement a FHT by using a high-contrast germanium-doped SOS MRR that is all-optically tunable. The tunability is achieved based on the polarization dependency of the MRR by changing the polarization direction of the incident light to the MRR using a polarization controller. The polarization tuning as fast as a few μs can be achieved by using a high-speed polarization controller. Silica is an isotropic material; however, SOS waveguides show high polarization dependency as a result of thermal stress. The mismatch between the thermal expansion coefficient (TEC) of the silicon substrate and the three glass layers (bottom cladding, core, and top cladding) is the main reason of this stress. The induced polarization dependency has been considered as a drawback in silica planar optical waveguides. Different methods have been proposed to reduce this SOS polarization dependency [191-193]. However, for the implementation of a FHT, this polarization dependency can be perfectly used to all-optically tune the coupling coefficient and the loss factor, leading to the tuning of the phase shift at the resonance wavelength, thus the fractional order of the FHT. In the implementation, the polarization direction of the input signal applied to the MRR is changed, which leads to the change of the phase shift at the resonance wavelength of the MRR, thus the fractional order is changed. A germanium-doped SOS MRR with a high index contrast of 3.8% is fabricated. The use of the fabricated MRR to implement a continuously tunable FHT is demonstrated. In the experiment, Hilbert transformation of a Gaussian pulse with a temporal full-width at half-maximum (FWHM) of 80 ps with tunable fractional orders at 0.85, 0.95, 1, 1.13, and 1.22 is realized.

A HT is an all-pass filter which shifts the phase of the negative frequency components by $+90^{o}$ and the phase of the positive frequency components by -90^{o}. Therefore, the frequency response of a classical HT can be expressed as

$$H_C(\omega) = -j\,\mathrm{sgn}(\omega), \tag{6-4}$$

where ω is the optical frequency, and $\mathrm{sgn}(\omega)$ is the sign function defined as

$$\mathrm{sgn}(\omega) = \begin{cases} +1, & \omega > 0 \\ 0, & \omega = 0 \\ -1, & \omega < 0 \end{cases} \tag{6-5}$$

The generalized format of the HT called FHT has a frequency response given by [67],

$$H_F(\omega) = \begin{cases} e^{-j\varphi}, & \omega > 0 \\ \cos(\varphi), & \omega = 0 \\ e^{+j\varphi}, & \omega < 0 \end{cases} \tag{6-6}$$

where $\varphi = \rho \times \pi / 2$ is the phase shift and ρ is the fractional order. As can be seen from Eq. (6.6) a FHT of an order of ρ has a magnitude response of 1 and a phase shift of ρπ at $\omega = 0$.

The frequency response of the through port of a double-bus ring resonator can be expressed as [188],

$$T = \alpha_c \left[\frac{t - t\alpha e^{j\theta}}{1 - \alpha t^2 e^{j\theta}} \right] \tag{6-7}$$

where $\theta = 2\pi n_{eff} L / \lambda$ is the total round-trip phase accumulation, t is the coupling coefficient, and $\alpha = \alpha_r \cdot \alpha_c$ is total loss factor which is the combination of the loss factor inside the ring (α_r), and the loss of the ring's coupler (α_c). The coupling coefficient and the loss factor of the MRR are strongly polarization dependent. The birefringence in a SOS waveguide origins from the thermal stress caused by TEC mismatch of different layers during the high-temperature treatment employed in the glass deposition process of the fabrication. The thermal stress is dependent on the dopant level of the core. A higher refractive index contrast results in a higher thermal stress and correspondingly a higher polarization dependency. By changing the polarization direction of the input pulse introduced to the ring, the resonance spectral response is changed, which leads to the change of the phase shift at the resonance wavelength. Therefore, by choosing the wavelength of the optical carrier carrying the optical pulse at the resonance wavelength, a tunable phase shift is introduced at the center of the optical pulse, and since the resonance width is ultranarrow, a fractional Hilbert transformation of the pulse is obtained. Tuning of the FHT is achieved by tuning the polarization direction of the input pulse.

A high-contrast germanium-doped SOS waveguide has a low propagation loss and a low bending loss [194]. An ultralow-loss MRR with a propagation loss of 0.085 dB/cm was recorded by using a germanium-doped SOS waveguide with an index contrast of 3.5% [195]. In a MRR, a lower loss would results in a higher Q-factor, corresponding to a narrower resonance bandwidth. In addition, the use of a high-contrast germanium-doped SOS waveguide can reduce the minimum lossless bend radius of a MRR. A smaller radius corresponds to a larger free-spectral range (FSR). Therefore, by using a high-contrast MRR with a narrower resonance bandwidth and a larger FSR, a broadband HT can be implemented.

A germanium-doped waveguide with a high-refractive index core (n_c =1.5) is fabricated. The wafer is oxidized to create the bottom layer. A germanium-doped layer is deposited on the top. The core layer and the cladding layers are annealed after deposition. Since the refractive index of pure silica is n_b =1.445, a high index contrast of 3.8% is achieved ($\Delta n = (n_c - n_b)/n_b$). The cross section of the core is 2 μm x 2 μm. This waveguide shows a bend radius less than 1 mm [196]. A double-bus MRR with 1 mm radius of curvature and 2 μm coupler gaps is fabricated on this waveguide. This MRR shows a low propagation loss of 0.02 dB/cm. The FSR of this ring is 32 GHz, while the full width at half maximum (FWHM) bandwidth of the resonance is as small as 140 MHz. The operation bandwidth of the HT, which is approximately equal to two times the FSR minus the null-to-null bandwidth of the notch, is very large (0.44 nm or 55 GHz). Therefore, this MRR is a good candidate for implementing a broad bandwidth HT. The transmission spectrum of the fabricated MRR is measured by an optical vector analyzer (LUNA TECHNOLOGIES). To study the polarization dependence, the polarization direction of the input light to the MRR is tuned, from the transverse electric (TE) mode to the transverse magnetic (TM) mode, by tuning a polarization controller (PC). When the polarization direction of the input light wave is orientated at an angle of 45^{o} relative to one principal axis of the MRR, the light wave is equally split into the TE and TM modes, with the transmission spectrum shown in Fig. 6.8 as the red-dotted line. If the input light wave is orientated at an angle smaller or greater than 45^{o}, the TE mode is greater or smaller than the TM mode (the blue-solid line and green-dashed line in Fig. 1). From Fig. 6.8 we can also see that a TE mode resonance occurs at the wavelength of 1551.05 nm while a TM mode resonance occurs at 1551.15 nm due to the birefringence of the waveguide. By changing the input light wave from a TE mode to a TM mode, the depth of the TE resonance is decreased from its maximum until it vanishes and the depth of the TM mode resonance is increased to reach its maximum. Since the depth of the resonance is changed by changing the polarization direction of the input light wave, the phase shift at the resonance wavelength is accordingly changed which can be used to implement a tunable FHT.

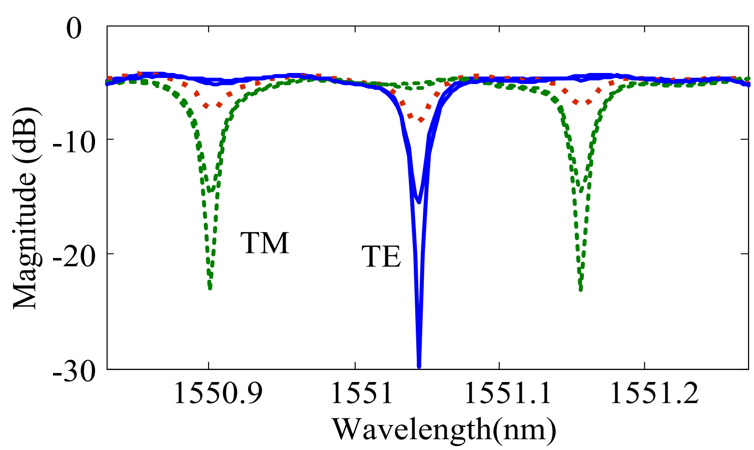

Fig. 0.8. The transmission magnitude response of the MRR at different light polarization directions.

Fig. 6.9 shows the magnitude and phase responses of the MRR around the resonance wavelength of 1551.88 nm for the input light wave at four different polarization directions. As can be seen from Fig. 6.9, by changing the polarization direction from state 1 to state 4, the depth of the resonance is increased and correspondingly the phase shift at the resonance wavelength is changed from 1.55 to 4.16 rad. The frequency responses of the MRR in Fig. 6.9 demonstrate that a tunable FHT can be implemented by changing the input light polarization direction. By applying a Gaussian pulse with a temporal FWHM of 40 ps centered at the resonance wavelength to the MRR, a Hilbert transformed signal is obtained. Fig. 6.10 shows the simulated Hilbert transformed signals by using the spectral response of the MRR for four different polarization directions shown in Fig. 6.9. The corresponding fractional orders are 0.53, 0.82, 1.14, and 1.32. As a comparison, four ideally Hilbert transformed signals with the same fractional orders are also simulated and shown in Fig. 6.10. As can be seen the Hilbert transformed signals using the MRR and the ideally Hilbert transformed signals are very close. The small errors are mainly due to the notch in the magnitude response of the MRR. For an ideal FHT, the magnitude response should be constant over the bandwidth.

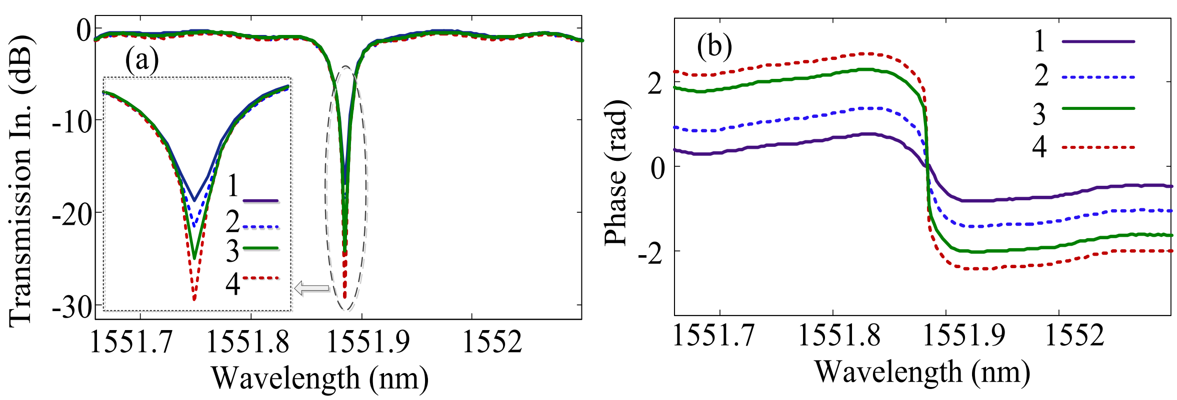

Fig. 0.9. (a) The transmission magnitude responses and (b) the phase responses of the fabricated high-contrast silica-on-silicon MRR for an input light wave with four different polarization directions.

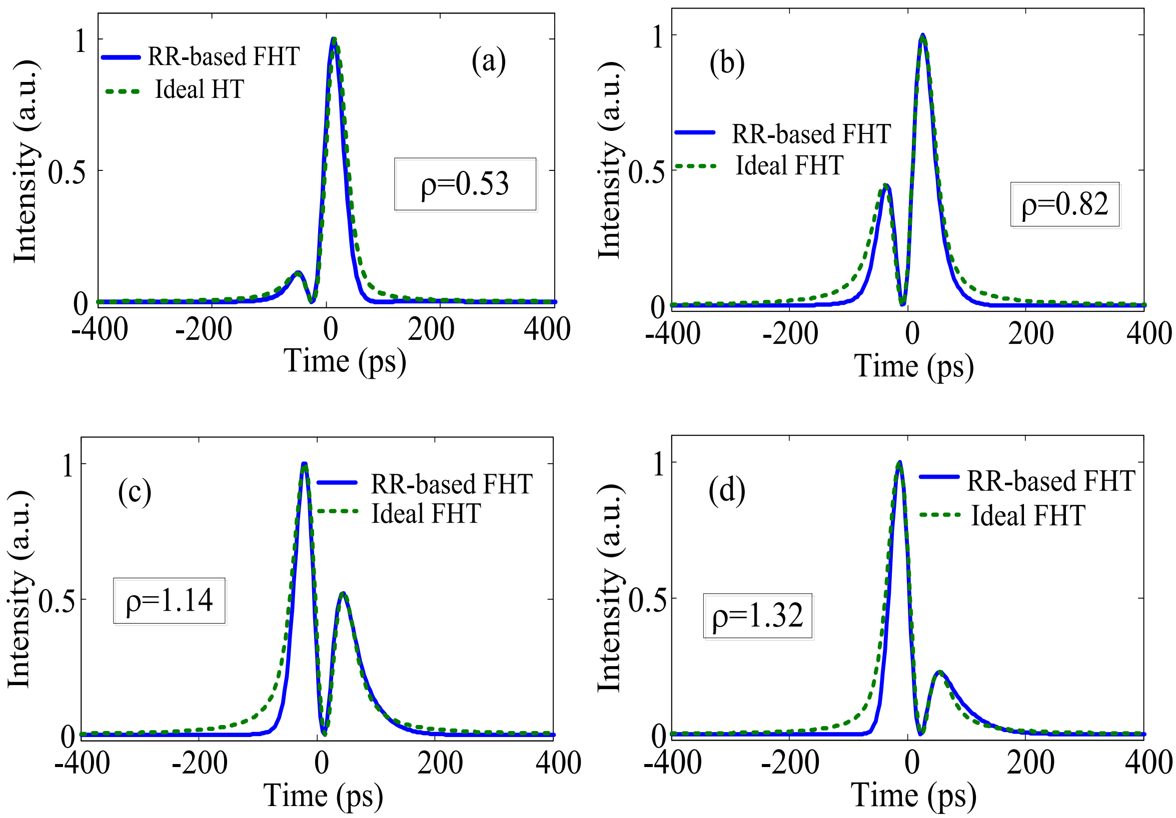

Fig. 0.10. Fractional Hilbert transform of a Gaussian pulse by using spectral response of the MRR for four different polarization directions shown in Fig. 2 (solid lines). The FHT orders corresponding to the polarization directions are (a) 0.53, (b) 0.82, (c) 1.14, and (d) 1.32. Fractional Hilbert transforms of an ideal Gaussian pulse with the same orders are also shown for comparison (dashed lines).

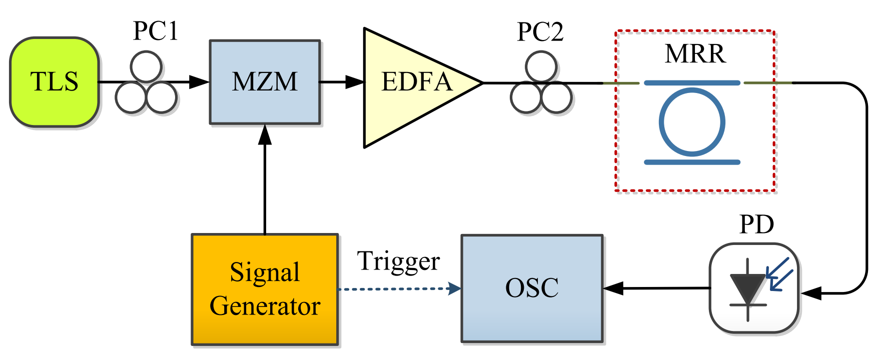

Fig. 0.11. Experimental setup. TLS: tunable laser source, MZM: Mach-Zehnder modulator, EDFA: erbium-doped fiber amplifier, PC: polarization controller, PD: photodetector, OSC: oscilloscope.

An experiment is then performed to evaluate the operation of the MRR as a FHT. The experimental setup is shown in Fig. 6.11. A continues wave (CW) light generated by a tunable laser source (TLS, Anritsu MG9638A) is sent to a 20-GHz Mach-Zehnder modulator (MZM) via a polarization controller (PC1). A Gaussian pulse with a temporal FWHM of 80 ps is generated by a signal generator and applied to the MZM. The modulated signal at the output of the MZM is sent to an erbium-doped fiber amplifier (EDFA). A second polarization controller (PC2), which is electronically controlled with high precision (JDS Uniphase PR2000), is used to control and tune the polarization direction of the modulated light to the MRR. Two tapered fibers are used to couple the modulated light into and out of the MRR. The optical signal at the output of the MRR is detected with a 53-GHz photodetector (PD) and the waveform is observed with a sampling oscilloscope (OSC). The transmission spectrum of the fabricated MRR has a TE mode resonance at 1551.88 nm, which is shown in Fig. 6.9. The wavelength of the TLS is thus tuned at 1551.88 nm. Fig. 6.12(a) shows the input Gaussian signal (solid line) generated by the signal generator. An ideal Gaussian signal with a temporal bandwidth of 80 ps is also shown in Fig. 6.12(a) (dashed line) for comparison. By tuning the polarization direction of the input pulse via PC2, Hilbert transformed Gaussian pulses with different fractional orders are observed. In Fig. 6.12(b)-(f), five fractional Hilbert transformed signals with different fractional orders at 1, 0.85, 0.95, 1.05, and 1.13 corresponding to five different input polarization directions are shown. Fractional Hilbert transforms of the ideal Gaussian pulse shown in Fig. 6.12(a) with an ideal FHT with the same orders are also simulated and shown in Fig. 6.12(b)-(f) as dashed lines. As can be seen a good agreement is reached. The root mean square (RMS) error is calculated, which is less than 5%. The difference between the simulated and experimental results is mainly caused by the non-constant magnitude response of the MRR, the non-ideal Gaussian pulse and the limited bandwidth of the PD.

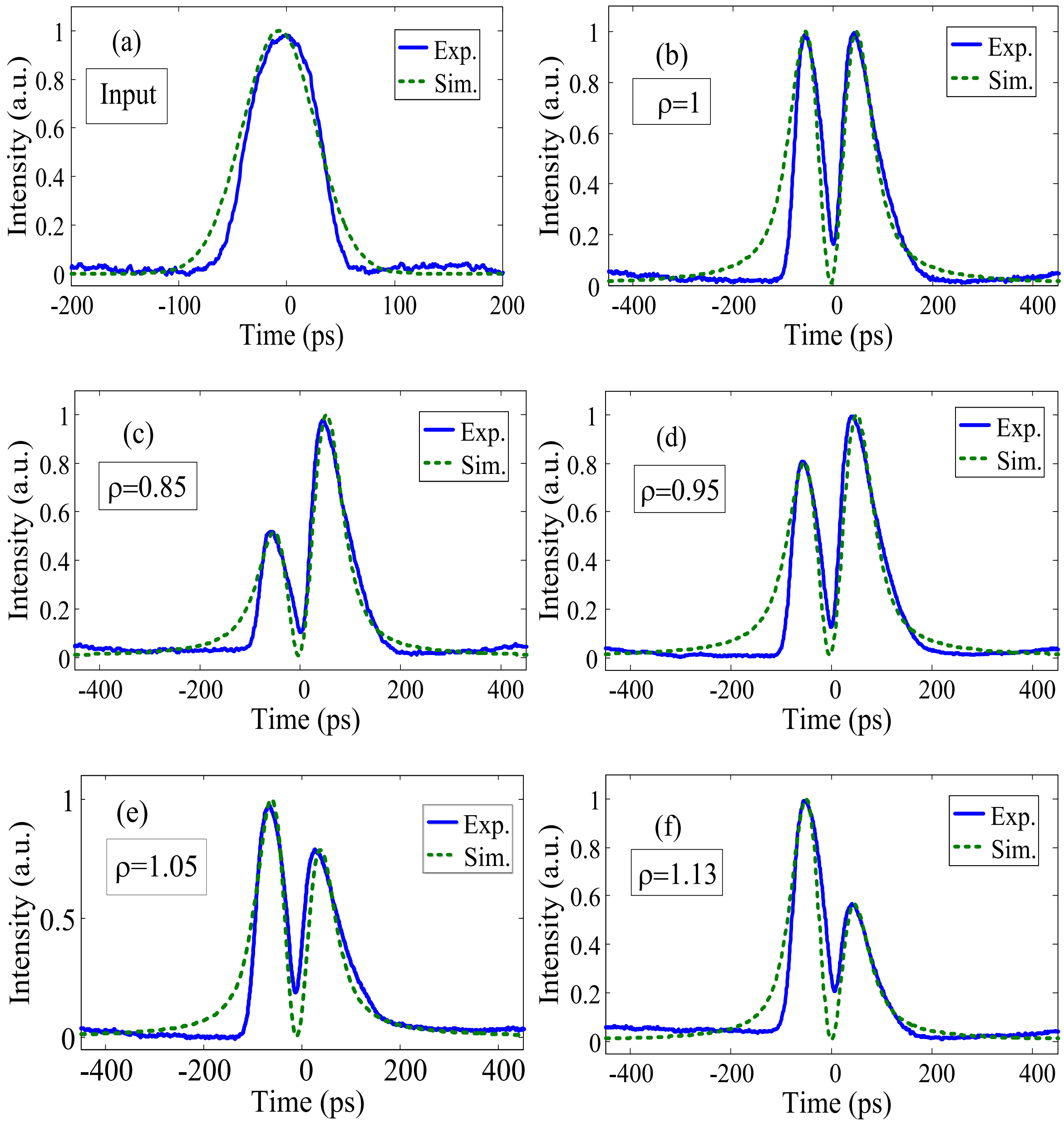

Fig. 0.12. (a) An experimentally generated Gaussian pulse (solid line) with a temporal FWHM of 80 ps. An ideal Gaussian pulse (dashed line) is also shown for comparison. The fractional Hilbert transformed pulses (solid lines) with different orders of (b) 1, (c) 0.85, (c) 0.95, (e) 1.05, and (f) 1.13. Fractional Hilbert transforms of an ideal Gaussian pulse with an ideal FHT at the same orders are also shown for comparison (dashed lines).

In conclusion, a continuously tunable FHT was proposed and experimentally demonstrated by using a high-contrast germanium-doped SOS MRR. Two features of this MRR make it possible to operate as a tunable FHT. First, as a result of a high index contrast, the MRR has a narrow resonance and a large FSR, which is suitable for the implementation of a HT with a wide operation bandwidth. Second, the MRR is highly birefringent, by changing the polarization direction of the input light wave into the MRR, a tunable phase shift at the resonance wavelength is produced which can be used to implement a FHT with a tunable fractional order. A germanium-doped SOS MRR with an index contrast of 3.8% was fabricated. This fabricated MRR provides an FSR of 32 GHz and an FWHM bandwidth of the notch of 140 MHZ which was used to implement a FHT with a wide operation bandwidth of 55 GHz. This fabricated MRR was used to experimentally demonstrate a continuously tunable FHT with tunable fractional orders at 1, 0.85, 0.95, 1.05, and 1.13, and a Gaussian pulse with a temporal FWHM of 80 ps was Hilbert transformed at different orders.

CHAPTER 6 SUMMARY AND FUTURE WORK

7.1. Summary

In this thesis, the research efforts were focused on the investigation of innovative techniques to generate slow and fast light and demonstrate their applications in microwave photonics systems. Novel schemes to generate slow and fast light based on advanced FBGs were proposed and demonstrated experimentally. Two different types of FBGs, LCFBG and TFBG, were designed and fabricated which were playing the key role in generating slow and fast light. In general, the spectral characteristics of an FBG are fixed after fabrication and they are tunable by some mechanical or thermal tunings. In this thesis, for the first time, we proposed and demonstrated optically reconfigurable FBGs by writing them in Er/Yb co-doped fibers. Thanks to the high absorption of the Er/Yb co-doped fiber, the FBG's refractive index is changed when it is pumped with a 980-nm LD, as a result the spectral characteristics of the FBG are changed. Despite the thermoelectric heating, this pump induced thermo-optic heating is rapid and localized which does not need additional procedure during fabrication or additional setup for heat controlling such as a heat sink, sealed environment and feedback. Also this tuning method despite the mechanical tuning has a high stability. Therefore, a fast, reliable and stable tuning was demonstrated. A tunable delay line was demonstrated based on an LCFBG written in an Er/Yb co-doped fiber. The slow and fast light effects observed in this LCFBG were used in an UTPS system as a tunable dispersion to achieve tunable microwave frequency multiplication. In addition, a TFBG written in an Er/Yb co-doped fiber was used to demonstrate tunable slow and fast light. The TFBG-based slow and fast light effects were used to implement linearly chirped microwave waveform generation, all-optical continuously tunable phase shifting, continuously tunable fractional order differentiation, and continuously tunable microwave photonic filtering. In addition, a novel technique to generate continuously tunable slow and fast light based on a silicon-on-insulator microring resonator with MMI couplers was proposed and demonstrated experimentally. By designing the MMI coupler to be optimized for the TM mode, the coupling coefficient of the ring was tunable by changing the input light polarization, therefore the resonance characteristics and correspondingly the achieved slow and fast light was tunable. This tunable slow and fast light effect was used to implement a tunable fractional order differentiator. Finally, a continuously tunable fractional order Hilbert transformer was proposed and experimentally demonstrated by using slow and fast light effects in a MRR on a silica-on-silicon platform. Based on our best knowledge, the silica-on-silicon waveguide's polarization dependency was used for the first time to optically tune the coupling coefficient and the loss factor of a MRR which results a tunable phase shift at the resonance wavelength. This tunable phase shift was used to implement a tunable fractional Hilbert transformer.

7.2. Future work

In this thesis, different FBGs have been fabricated and incorporated into the proposed systems to achieve slow and fast light. Also integrated MRRs have been fabricated and used for the same purpose. In the proposed structures, the used discrete optical devices, such as high-speed electro-optical modulators and photodetectors are bulky and costly. A solution to reduce the size and cost of the whole system is to integrate all discrete optical devices on a photonic integrated circuit (PIC).

The size and stability of the FBGs used in this thesis can be significantly improved by using integrated FBGs. In an integrated FBG, by designing the grating apodization through the change of the rib width, the group delay spectrum can be adjusted and tuned.

In this thesis, the tunability in the MRRs has been achieved by changing the input polarization direction. However, for most application, it is demanded that the polarization remains unchanged. A solution to achieve a fast and reliable group delay spectrum tuning in an integrated FBG or MRR without using an additional procedure during fabrication is to use dope the integrated waveguides with Er/Yb dopant. Thus by optically pumping the FBG or MRR, a fast and reliable group delay tuning can be achieved.

The slow and fast light generate by the proposed techniques in the thesis has been used for the implementation of microwave photonic functions. Again, due to the use of discrete components, the systems were bulky and the performance, especially the stability, was limited. A solution to improve the performance is to integrate the system using PICs.

LIST OF REFERENCE

[1] J. Capmany, I. Gasulla, and S. Sales, “Microwave photonics: Harnessing slow light,” Nature Photon., vol. 5, no. 12, pp. 731–732, Dec. 2011.

[2] L. V. Hau, S. E. Harris, Z. Dutton, and C. H. Behroozi, “Light speed reduction to 17 metres per second in an ultracold atomic gas,” Nature, vol. 397, no. 6720, pp. 594–598, Feb. 1999.

[3] M. S. Bigelow, N. N. Lepeshkin, and R. W. Boyd, “Superluminal and slow light propagation in a room-temperature solid,” Science, vol. 301, no. 5630, pp. 200–202, Jul. 2003.

[4] A. Schweinsberg, N. N. Lepeshkin, M. S. Bigelow, R. W. Boyd, and S. Jarabo, “Observation of superluminal and slow light propagation in erbium-doped optical fiber,” Europhys. Lett., vol. 73, no. 2, pp. 218-224, Jan. 2006.

[5] W. Xue, S. Sales, J. Capmany, and J. Mørk, “Wideband 360° microwave photonic phase shifter based on slow light in semiconductor optical amplifiers,” Opt. Express, vol. 18, no. 6, pp. 6156–6163, Mar. 2010.

[6] K. Y. Song, M. G. Herráez, and L. Thévenaz, “Observation of pulse delaying and advancement in optical fibers using stimulated Brillouin scattering,” Opt. Express, vol. 13, no. 1, pp. 82–88, Jan. 2005.

[7] L. Xing, L. Zhan, S. Luo, and Y. Xia, “High-power low-noise fiber Brillouin amplifier for tunable slow-light delay buffer,” IEEE J. Quantum Electron., vol. 44, no. 12, pp. 1133–1138, Dec. 2008.

[8] Z. Zhu, A. M. C. Dawes, D. J. Gauthier, L. Zhang, and A. E. Willner, “12-GHz-bandwidth SBS slow light in optical fibers,” Optical Fiber Communication Conference. OFC 2006, Anaheim, CA, pp. 1-3, paper PDP1.

[9] K. Y. Song and K. Hotate, “25 GHz bandwidth Brillouin slow light in optical fibers,” Opt. Lett., vol. 32, no. 3, pp. 217–219, Feb. 2007.

[10] Y. Wang, C. Yu, L. S. Yan, A. E.Willner, R. Roussev, C. Langrock, M. M. Fejer, Y. Okawachi, J. E. Sharping, and A. L. Gaeta, "44-ns continuously tunable dispersionless optical delay element using a PPLN waveguide with a two pump configuration, DCF, and a dispersion compensator," IEEE Photon. Technol. Lett., vol. 19, no. 11, pp. 861–863, Jun. 2007.

[11] A. Gaeta, J. Sharping, and C. Xu, "All Optical, continuously tunable pulse delay generator using wavelength conversion and dispersion," United State Patent, patent No. 7,538,935 B2, May 2006.

[12] C. R. Giles, "Lightwave applications of fiber Bragg gratings," J. Lightw. Technol., vol. 15, no. 8, pp. 1391-1404, Aug. 1997.

[13] J. Capmany, D. Pastor, B. Ortega, J. L. Cruz, and M. V. Andres, "Applications of fiber Bragg gratings to microwave photonics," Fiber Integrated Opt., vol. 19, no. 4, pp. 483-494. 2000.

[14] J. T. Mok, C. M. de Sterke, I. C. M. Littler, and B. J. Eggleton, "Dispersionless slow light using gap solitons," Nature Phys., vol. 2, no. 11, pp. 775–780, Oct. 2006.

[15] Y. Lui, J. Yang, and J. Yao,"Continuous true-time-delay beamforming for phased array antenna using a tunable chirped fiber grating delay line," IEEE Photon. Technol. Lett. , vol. 14, no. 8, pp. 1172–1174, Aug. 2002.

[16] B. Ortega, J. L. Cruz, J. Capmany, M. V. Andres, and D. Poster, "Analysis of a microwave time delay line based on a perturbed uniform fiber Bragg grating operating at constant wavelength," J. Lightw. Technol., vol. 18, no. 3, pp. 430-436, Mar. 2000.

[17] M. Pisco, S. Campopiano, A. Cutolo, and A. Cusano, "Continuously variable optical delay line based on a chirped fiber Bragg grating," IEEE Photon. Technol. Lett., vol. 18, no. 24, pp. 2551–2553, Dec. 2006.

[18] M. Pisco, A. Ricciardi, S. Campopiano, C. Caucheteur, P. Megret, A. Cutolo, and A. Cusano, "Fast and slow light in optical fibers through tilted fiber Bragg gratings," Opt. Express, vol. 17, no. 26, pp. 23502–230510, Dec. 2009.

[19] F. Xia, L. Sekaric, and Y. Vlasov, "Ultracompact optical buffers on a silicon chip," Nat. Photon., vol. 1, pp. 65–71, Jan. 2007.

[20] F. Morichetti, A. Melloni, A. Breda, A. Canciamilla, C. Ferrari, and M. Martinelli, "A reconfigurable architecture for continuously variable optical slow-wave delay-lines," Opt. Express, vol. 15, no. 25, pp. 17273–17282, Dec. 2007.

[21] P. Chamorro-Posada and F. J. Fraile-Pelaez, "Fast and slow light in zigzag microring resonator chains," Opt. Lett., vol. 34, no. 5, pp. 626-628, Mar. 2009.

[22] C. Ciminelli, C. E. Campanella, F. Dell'Olio, and M. N. Armenise, "Fast light generation through velocity manipulation in two vertically-stacked ring resonators," Opt. Express, vol. 18, no. 3, pp. 2973-2986, Feb. 2010.

[23] N. Pornsuwancharoen, N. Sangwara, and P. P. Yupapin, "Generalized fast and slow lights using multi-state microring resonators for optical wireless links," Optik, vol. 121. no. 19, pp. 1721-1724, Oct. 2010.

[24] T. Wang, F. Liu, T. Ye, Z. Zhang, J. Wang, Y. Tian, M. Qiu, and Y. Su, "Continuesly-tunable slow and fast light using silicon microring add-drop filter with mutual mode coupling," Optical Fiber Communication (OFC) Conference, Mar. 2009, San Diego, CA paper OWC4.

[25] Q. Li, Z. Zhang, J. Wang, M. Qiu, and Y. Su, "Fast light in silicon ring resonator with resonance-splitting," Opt. Express, vol. 17, no. 2, pp. 933–940, Jan. 2009.

[26] X. Luo, H. Chen, and A. W. Poon, "Electro-optical tunable time delay and advance in silicon microring resonators," Opt. Lett., vol. 35, no. 17, pp. 2940-2942, Sep. 2010.

[27] H. Atabaki, B. Momeni, A. A. Eftekhar, E. S. Hosseini, S. Yegnanarayanan, and A. Adibi, "Tuning of resonance-spacing in a traveling-wave resonator device," Opt. Express, vol. 18, no. 9, pp. 9447–9455, Apr. 2010.

[28] Y. H. Wang, C. S. Ma, X. Yan, and D. M. Zhang, "Analysis for amplifying characteristics of Er^{3+}−Yb^{3+}-co-doped microring resonators," Opt. Laser Technol., vol. 42, no. 2, pp. 336–340, Mar. 2010.

[29] D. G. Rabus, Z. Bian, and A. Shakouri, "Ring resonator lasers using passive waveguides and integrated semiconductor optical amplifiers," IEEE J. Sel. Top. Quantum Electron., vol. 13, no. 5, pp. 1249–1256, Sep. 2007.

[30] R. Pant, A. Byrnes, C. G. Poulton, E. Li, D. Y. Choi, S. J. Madden, B. Luther-Davies, and B. J. Eggleton, "On-chip slow and fast light using stimulated Brillouin scattering,"

Bragg Gratings, Photosensitovity, and Polling in glass waveguides (BGPP) Confrence, Jun. 2012, paper ITu3C.

[31] M. Bertero, M. Miyakawa, P. Boccacci, F. Conte, K. Orikasa, and M. Furutani, “Image restoration in chirp-pulse microwave CT (CP-MCT),” IEEE Trans. Biomed. Eng., vol. 47, no. 5, pp. 690–699, May 2000.

[32] J. U. Kang, M. Y. Frankel, and R. D. Esman, “Demonstration of microwave frequency shifting by use of a highly chirped mode-locked fiber laser,” Opt. Lett., vol. 23, no. 15, pp. 1188–1190, Aug. 1998.

[33] J. M. Fuster, D. Novak, A. Nirmalathas, and J. Marti, “Single-sideband modulation in photonic time-stretch analogue-to-digital conversion,” Electron. Lett., vol. 37, no. 1, pp. 67–68, Jan. 2001.

[34] J. Azana, N. K. Berger, B. Levit, V. Smulakovsky, and B. Fischer, “Frequency shifting of microwave signals by use of a general temporal self-imaging (Talbot) effect in optical fibers,” Opt. Lett., vol. 29, no. 24, pp. 2849–2851, Dec. 2004.

[35] C. Wang, M. Li, and J. P. Yao, “Continuously tunable photonic microwave frequency multiplication by use of an unbalanced temporal pulse shaping system,” IEEE Photon. Technol. Lett., vol. 22, no. 17, pp. 1285–1287, Sep. 2010.

[36] J. P. Yao, “Photonic generation of microwave arbitrary waveforms,” Opt. Comm., vol. 284, no. 15, pp. 3723-3736, Jul. 2011.

[37] [Online]. Available: http://www.tek.com/signal-generator/awg70000-arbitrary-waveform-generator

[38] J. D. McKinney, D. E. Leaird, and A. M. Weiner, “Millimeter-wave arbitrary waveform generation with a direct space-to-time pulse shaper,” Opt. Lett., vol. 27, no. 15, pp. 1345–1347, Aug. 2002.

[39] J. D. McKinney, D. Seo, D. E. Leaird, and A. M. Weiner, “Photonically assisted generation of arbitrary millimeter-wave and microwave electromagnetic waveforms via direct space-to-time optical pulse shaping,” J. Lightwave Technol., vol. 21, no. 12, pp. 3020-3028, Dec. 2003.

[40] V. Torres, J. Lancis, P. Andres, and L. R. Chen, “Reconfigurable RF-waveform generation based on incoherent-filter design,” J. Lightw. Technol., vol. 26, no. 15, pp. 2476–2483, Aug. 2008.

[41] J. W. Shi, F. M. Kuo, N. W. Chen; S. Y. Set, C. B. Huang, and J. E. Bowers, “Photonic generation and wireless transmission of linearly/nonlinearly continuously tunable chirped millimeter-wave waveforms with high time-bandwidth product at W-band,” IEEE Photon. J., vol. 4, no. 1, pp. 215-223, Feb. 2012.

[42] H. Chi and J. P. Yao, “All-fiber chirped microwave pulses generation based on spectral shaping and wavelength-to-time conversion,” IEEE Trans. Microw. Theory Tech., vol. 55, no. 9, pp. 1958–1963, Sep. 2007.

[43] C. Wang and J. P. Yao, “Photonic generation of chirped millimeterwave pulses based on nonlinear frequency-to-time mapping in a nonlinearly chirped fiber Bragg grating,” IEEE Trans. Microw. Theory Tech., vol. 56, no. 2, pp. 542–553, Feb. 2008.

[44] M. Li, L. Shao, J. Albert, and J. P. Yao, “Tilted fiber Bragg grating for chirped microwave waveform generation,” IEEE Photon. Technol. Lett., vol. 23, no. 5, pp. 314–316, Mar. 2011.

[45] Y. Dai and J. P. Yao, “Chirped microwave pulse generation using a photonic microwave delay-line filter with a quadartic phase response,” IEEE Photon. Technol. Lett., vol. 21, no. 9, pp. 569–571, May 2009.

[46] G. A. Ball, W. H. Glenn, and W. W. Morey, “Programmable fiber optic delay line,” IEEE Photon. Technol. Lett., vol. 6, no. 6, pp. 741-743, Jun. 1994.

[47] J. L. Cruz, B. Ortega, M. V. Andres, B. Gimeno. D. Pastor, J. Capmany and L. Dong, “Chirped fibre Bragg gratings for phased-array antennas,” Electron. Lett., vol. 33, no. 7, pp. 545-546, Mar. 1997.

[48] J. Capmany, B. Ortega, D. pastor, and S. Sales, “Discrete-time optical processing of microwave signals,” J. Lightw. Technol., vol. 23, no. 2, pp. 702-723, Feb. 2005.

[49] M. R. Fisher and S. L. Chuang, “A microwave photonic phase-shifter based on wavelength conversion in a DFB laser,” IEEE Photon. Technol. Lett., vol. 16, no. 6, pp. 1714–1716, Aug. 2006.

[50] A. Loayssa and F. J. Lahoz, “Broad-band RF photonic phase shifter based on stimulated Brillouin scattering and single-sideband modulation,” IEEE Photon. Technol. Lett., vol. 18, no. 1, pp. 208–210, Jan. 2006.

[51] P. K. Kondratko and S. L. Chuang, “Slow-to-fast light using absorption to gain switching in quantum-well semiconductor optical amplifier,” Opt. Express, vol.15, no. 16, pp. 9963-9969, Aug. 2007.

[52] J. Mørk, R. Kjær, M. van der Poel, and K. Yvind, "Slow light in a semiconductor waveguide at gigahertz frequencies," Opt. Express, vol. 13, no. 20, pp. 8136–8145, Oct. 2005.

[53] W. Xue, S. Sales. J. Capmany, and J. Mørk, “Microwave phase shifter with controllable power response based on slow- and fast-light effects in semiconductor optical amplifiers,” Opt. Lett., vol. 34, no. 7, pp. 929-931, Apr. 2009.

[54] J. Sancho, J. Llort, I. Gasulla, S. Sales, and J. Capmany, “Fully 3600 microwave photonic phase shifter on a single semiconductor optical amplifier,” Opt. Express, vol. 19, no. 18, pp. 17421-17426, Aug. 2011.

[55] F. Li, Y. Park, and J. Azaña, “Complete temporal pulse characterization based on phase reconstruction using optical ultrafast differentiation (PROUD),” Opt. Lett., vol. 32, no. 22, pp. 3364–3366, Nov. 2007.

[56] J. P. Yao, F. Zeng, and Q. Wang, “Photonic generation of ultrawideband signals,” J. Lightw. Technol., vol. 25, no. 11, pp. 3219–3235, Nov. 2007.

[57] Y. Park, M. Kulishov, R. Slavík, and J. Azaña, “Picosecond and sub-picosecondn flat-top pulse generation using uniform long-period fiber gratings,” Opt. Express, vol. 14, no. 26, pp. 12670–12678, Dec. 2006.

[58] H. J. da Silva and J. J. O’Reilly, “Optical pulse modeling with Hermite-Gaussian functions,” Opt. Lett., vol. 14, no. 10, pp. 526–528, May 1989.

[59] J. A. Ney da Silva and M. L. R. de Campos, “Spectrally efficient UWB pulse shaping with application in orthogonal PSM,” IEEE Trans. Commun., vol. 55, no. 2, pp. 313–322, Feb. 2007.

[60] J. Xu, X. Zhang, J. Dong, D. Liu, and D. Huang, "High-speed all-optical differentiator based on semiconductor optical amplifier and an optical filter," Opt. Lett., vol. 32, no. 13, pp. 1872–1874, Jul. 2007.

[61] M. Kulishov and J. Azaña, "Long-period fiber gratings as ultrafast optical differentiators," Opt. Lett., vol. 30, no. 20, pp. 2700-2702, Oct. 2005.

[62] N. K. Berger, B. Levit, B. Fischer, M. Kulishov, D. V. Plant, and J. Azaña, "Temporal differentiation of optical signals using a phase-shifted fiber Bragg grating," Opt. Express, vol. 15, no. 2, pp. 371–381, Jan. 2007.

[63] M. Li, D. Janner, J. P. Yao, and V. Pruneri, "Arbitrary-order all-fiber temporal differentiator based on a fiber Bragg grating: Design and experimental demonstration," Opt. Express, vol. 17, no. 22, pp. 19798–19807, Oct. 2009.

[64] F. Liu, T. Wang, L. Qiang, T. Ye, Z. Zhang, M. Qiu, and Y. Su, "Compact optical temporal differentiator based on silicon microring resonator," Opt. Express, vol. 16, no. 20, pp. 15880–15886, Sep. 2008.

[65] C. Cuadrado-Laborde and M. V. Andrés, "In-fiber all-optical fractional differentiator," Opt. Lett., vol. 34, no. 6, pp. 833-835, Mar. 2009.

[66] A. D. Poularikas, Transforms and Applications Handbook, 3rd ed. Boca Raton, CRC Press, 2010, ch. 7.

[67] A. W. Lohmann, D. Mendlovic, and Z. Zalevsky, "Fractional Hilbert transform," Opt. Lett., vol. 21, no. 4, pp. 281-283, Feb. 1996.

[68] C. S. Guo, Y. J. Han, J. B. Xu, and J. Ding, "Radial Hilbert transform with Laguerre-Gaussian spatial filters," Opt. Lett., Vol. 31, no. 10, pp. 1394-1396, May 2006.

[69] H. Emami, N. Sarkhosh, L. A. Bui, and A. Mitchell, "Wideband RF photonic in-phase and quadrature-phase generation," Opt. Lett., vol. 33, no. 2, pp. 98–100, Jan. 2008.

[70] H. Emami, N. Sarkhosh, L. A. Bui, and A. Mitchell, "Amplitude independent RF instantaneous frequency measurement system using photonic Hilbert transform," Opt. Express, vol. 16, no. 18, pp. 13707–13712, Sep. 2008.

[71] Z. Li, H. Chi, X. Zhang, and J. P. Yao, "A continuously tunable microwave fractional Hilbert transformer based on a photonic microwave delay-line filter using a polarization modulator," IEEE Photon. Technol. Lett., vol. 23, no. 22, pp. 1694–1696, Nov. 2011.

[72] Z. Li, Y. han, H. Chi, X. Zhang, and J. P. Yao, "A continuously tunable microwave fractional Hilbert transformer based on a nonuniformly spaced photonic microwave delay-line filter," J. Lightw. Technol., vol. 30, no. 12, pp. 1948-1953, Jun. 2012.

[73] X. Wang, M. Hanawa, K. Nakamura, K. Takano, and K. Nakagawa, "Sideband suppression charactersitics of optical SSB generatin filter with sampled FBG based 4-taps optical Hilbert transformer," in Proc. of Asia-Pacific Conference on Comunication (APCC 2009), pp. 622-625.

[74] M. H. Asghari and J. Azaña, "All-optical Hilbert transformer based on a single phase-shifted fiber Bragg grating: Design and analysis," Opt. Lett., vol. 34, no. 3, pp. 334–336, Feb. 2009.

[75] M. Li and J. P. Yao, "Experimental demonstration of a wideband photonic temporal Hilbert transformer based on a single fiber Bragg grating," IEEE Photon. Technol. Lett., vol. 22, no. 21, pp. 1559–1561, Nov. 2010.

[76] C. Sima, J. C. Gates, H. L. Rogers, P. L. Mennea, C. Holmes, M. N. Zervas, and P. G. Smith, "Phase controlled integrated interferometric single-sideband filter based on planar Bragg gratings implementing photonic Hilbert transform," Opt. Lett., vol. 38, no. 5, pp. 727-729, Mar. 2013.

[77] L. Zhuang, M. R. Khan, W. Beeker, A. Leinse, R. Heideman, C. Roeloffzen, "Novel microwave photonic fractional Hilbert transformer using a ring resonator-based optical all-pass filter," Opt. Express, vol. 20, no. 24, pp. 26449-26510, Nov. 2012.

[78] R. A. Minasian, "Photonic signal processing of microwave signals," IEEE Trans. Microw. Theory Tech., vol. 54, no. 2, pp. 832–846, Feb. 2006.

[79] J. P. Yao, "A tutorial on microwave photonics," IEEE Photon. Soc. Newsletter, vol. 26, no. 2, pp. 4-12, Apr. 2012.

[80] X. Xue, X. Zheng, H. Zhang, and B. Zhou, "Widely tunable single-bandpass microwave photonic filter employing a non-sliced broadband optical source," Opt. Express, vol. 19, no. 9, pp. 18423-18429. Sep. 2011.

[81] A. Loayssa, J. Capmany, M. Sagues, and J. Mora, "Demonstration of Incoherent Microwave photonic filters with all-optical complex coefficients," IEEE Photon. Technol. Lett., vol. 18, no. 16, pp. 1744-1746, Aug. 2006.

[82] Y. Yan, and J. P. Yao, "A tunable photyonic micriowave filter with a complex coefficinet using an optical RF phase shifter," IEEE Photon. Technol. Lett., vol. 19, no. 19, pp. 1472-1474, Oct. 2007.

[83] W. Xue, S. Sales, J. Mørk, and J. Capmany, "Widely tunable microwave photonic notch filter based on slow and fast light effects," IEEE Photon. Technol. Lett., vol. 21, no. 3, pp. 167-169, Feb. 2009.

[84] J. Lloret, G. Morthier, F. Ramos, S. Sales, D. V. Thourhout, T. Spuesens, N. Olivier, J. M. Fedeli, and J. Capmany, "Broadband microwave photonic fully tunable filter using a single heterogeneously integarted III-V/SOI-microdisk-based phase shifter," Opt. Express, vol. 20, no. 10, pp. 10796-10806, May 2012.

[85] X. Yi, T. X. H. Huang, and R. A. Minasian, "Tunable and reconfigurable photonic signal processor with programmable all-optical complex-coefficients," IEEE Trans. Microw. Theory Tech., vol. 58, no. 11, pp. 3088-3093, Nov. 2010.

[86] M. Song, C. M. Long, R. Wu, D. Seo, D. E. Leaird, and A. M. Weiner, "Reconfigurable and tunable flat-top microwave photonics filters utilizing optical frequency combs," IEEE Photon. Technol. Lett., vol. 23, no. 21, pp. 1618-1620, Nov. 2011.

[87] J. Lloret, J. Sancho, M. Pu, I. Gasulla, K. Yvind, S. Sales, and J. Capmany, "Tunable complex-valued multi-tap microwave photonic filter based on single silicon-on-insulator microring resonator," Opt. Express, vol. 19, no. 13, pp. 12402-12406, Jun. 2011.

[88] H. Shahoei, M. Li , and J. P. Yao, "Continuously tunable time delay using an optically pumped linearly chirped fiber Bragg grating," J. Lightw. Technol., vol. 29, no. 10, pp. 1465-1472, May 2011.

[89] H. Shahoei and J. P. Yao, "Continuously tunable slow and fast light by using an optically pumped tilted fiber Bragg grating written in an erbium/ytterbium co-doped fiber," IEEE Photon. Technol. Lett., vol. 24, no. 10, pp. 818-820, May 2012.

[90] H. Shahoei and J. P. Yao, "Continuously tunable microwave frequency multiplication by optically pumping linearly chirped fiber Bragg gratings in an unbalanced temporal pulse shaping system," J. Lightw. Technol., vol. 30, no. 12, pp. 1954-1959, Jun. 2012.

[91] H. Shahoei and J. P. Yao, "Continuously tunable chirped microwave waveform generation using a tilted fiber Bragg grating written in an erbium/ytterbium co-doped fiber," IEEE Photon. J., vol. 4, no. 3, pp. 765-771, Jun. 2012.

[92] H. Shahoei and J. P. Yao, "Tunable microwave photonic phase shifter based on slow and fast light effects in a tilted fiber Bragg grating," Opt. Express, vol. 20, no. 13, pp. 14009-14014, Jun. 2012.

[93] H. Shahoei, J. Albert, and J. P. Yao, "Tunable fractional order temporal differentiator by optically pumping a tilted fiber Bragg grating," IEEE Photon. Technol. Lett., vol. 24, no. 9, pp. 730-732, May 2012.

[94] H. Shahoei and J. P. Yao "Slow and fast light effects in a tilted fiber Bragg grating and the application in a continuously tunable microwave photonic Filter," International Microwave Symposuim Digest (IMS) 2013, Seattle, WA, USA, pp. 1-3.

[95] H. Shahoei and J. P. Yao, "A continuously tunable multi-tap complex-coefficient microwave photonic filter based on a tilted fiber Bragg grating," Opt. Express, vol. 21, no. 6, pp. 7521-7527, Mar. 2013.

[96] H. Shahoei, D. Xu, and J. P . Yao, "Continuous slow and fast light generation by a silicon-on-insulator microring resonator incorporating a MMI coupler," submitted.

[97] H. Shahoei, D. Xu, J. Schmid, and J. P. Yao, "Photonic fractional-order differentiator using an SOI microring resonator with an MMI coupler," IEEE Photon. Technol. Lett., vol. 25, no. 15, pp. 1408-1411, Aug. 2013.

[98] H. Shahoei, P. Dumais, and J. P. Yao, "Continuously tunbale photonic fractional Hilbert transformer using a high-contrast Germanium-doped silica-on-siliocn microring resonator," submitted.

[99] J. P. Yao, "Microwave photonics," J. Lightw. Technol., vol. 27, no. 3, pp. 314-335, Feb. 2009.

[100] H. Su, P. Kondratko, and S. L. Chaung ,"Variable optical delay using population oscillation and four-wave mixing in semiconductor optical amplifiers," Opt. Express, vol. 14, no. 11, pp. 4800-4807, May 2006.

[101] J. S. Toll, "Causality and the dispersion relation: logical foundations," Phys. Rev., vol. 104, no. 6, Jan. 1956.

[102] A. Molony, C. Edge, and I. Bennion, "Fibre grating time delay element for phased array antennas," Electron. Lett., vol. 31, no. 17, pp. 1485-1486, Aug. 1995.

[103] H. Zmuda, R. A. Soref, P. Payson, S. Johns, and E. N. Toughlian, “Photonic beamformer for phased array antennas using a fiber grating prism,” IEEE Photon. Technol. Lett., vol. 9, no. 2, pp. 241-243, Feb. 1997.

[104] R. Kashyap, Fiber Bragg Gratings, 2nd ed. New York: Academic Press, 1999.

[105] C. Yang, S. Yazdanfar, and J. Izatt, “Amplification of optical delay by use of matched linearly chirped fiber Bragg gratings,” Opt. Lett., vol. 29, no. 7, pp. 685-687, Apr. 2004.

[106] S. S. Lee and H. D. Chae, “Continuous photonic microwave true-time delay using tapered chirped fibre Bragg grating,” Electron. Lett., vol. 41, no. 12, pp. 690-691, Jun. 2005.

[107] J. P. Yao, J. Yang, and Y. Liu, “Continuous true-time-delay beamforming employing a multiwavelength tunable fiber laser source,” IEEE Photon. Technol. Lett., vol. 14, no. 5, pp. 687-689, May 2002.

[108] J. L. Corral, J. Marti, S. Regidor, J. M. Foster, R. Laming, and M. J. Cole, “Continuously variable true time-delay optical feeder for phased-array antenna employing chirped fiber grating,” IEEE Trans. Microwav. Theory Tech., vol. 45, no. 8, pp. 1531-1536, Aug. 1997.

[109] D. Pastor and J. Capmany, “Fibre optic tunable transversal filter using laser array and linearly chirped fibre grating,” Electron. Lett., vol. 34, no. 17, pp. 1684-1685, Aug. 1998.

[110] G. C. Valley, “A review of stimulated Brillouin scattering excited with a broad-band pump laser,” IEEE J. Quantum Electron., vol. 22, no. 5, pp. 704-712, May 1986.

[111] Y. Aoki and K. Tajima, “Stimulated Brillouin scattering in a long single-mode fiber excited with a multimode pump laser,” J. Opt. Soc. Am. B., vol. 5, no. 2, pp. 358-363, Feb. 1988.

[112] G. M. Gehring, R. W. Boyd, A. L. Gaeta, D. J. Gauthier, and A. E. Willner, “Fiber-based slow-light technologies,” J. Lightw. Technol., vol. 26, no. 23, pp. 3752-3762, Dec. 2008.

[113] R. W. Boyd, Nonlinear Optics, 2nd ed. NewYork: Academic Press, 2003.

[114] G. P. Agrawal., Nonlinear Fiber Optics, 2nd ed. San Diego: Academic Press, 1995.

[115] S. Chin, "Governing the speed of a light signal in optical fibers: Brillouin slow and fast light," PhD thesis, Swiss Federal Institute of Technology in Lausanne (EPFL), 2009.

[116] Z. Zhu, A. M. C. Dawes, D. J. Gauthier, L. Zhang, and A. E. Willner, "Broadband SBS slow light in an optical fiber," J. Lightw. Technol., vol. 25, no. 1, pp. 201-206, Jan. 2007.

[117] M. Gonzalez-Herráez, K. Y. Song, and L. Thévenaz, "Arbitrary-bandwidth Brillouin slow light in optical fibers," Opt. Express, vol. 14, no. 4, pp. 1395-1400, Feb. 2006.

[118] K. Y. Song, M. Gonzalez-Herráez, and L. Thévenaz, "Gain-assisted pulse advancement using single and double Brillouin gain peaks in optical fibers," Opt. Express, vol. 13, no. 24, pp. 9758-9765, Nov. 2005.

[119] Z. Zhu and D. J. Gauthier, "Nearly transparent SBS slow light in an optical fiber," Opt. Express, vol. 14, no. 16, pp. 7238-7245, Aug. 2006.

[120] S. Chin, M. Gonzalez-Herráez, and L. Thévenaz, "Simple technique to achieve fast light in gain regime using Brillouin scattering," Opt. Express, vol. 15. no. 17, pp. 10814-10821, Aug. 2007.

[121] R. Pant, M. D. Stenner, M. A. Neifeld, and D. J. Gauthier, "Optimal pump profile designs for broadband SBS slow-light systems," Opt. Express, vol. 16, no. 4, pp. 2764-2777, Feb. 2008.

[122] M. D. Stenner, M. A. Neifeld, Z. Zhu, A. M. C. Dawes, and D. J. Gauthier, "Distortion management in slow-light pulse delay," Opt. Express, vol 13, no. 25, pp. 9995-10002, Dec. 2005.

[123] A. Minardo, R. Bernini, and L. Zeni, "Low distortion Brillouin slow light in optical fibers using AM modulation," Opt. Express, vol. 15, no. 13, pp. 5866-5876, Jun. 2006.

[124] N. Yoshizawa and T. Imai, "Stimulated Brillouin scattering suppression by means of applying strain distribution to fiber with cabling," J. Lightw. Technol., vol. 11, no. 10, pp. 1518-1522, Oct. 1993.

[125] M. Nikles, L. Thevenaz, and P. A. Robert, "Brillouin gain spectrum characterization in single-mode optical fibers," J. Lightw. Technol., vol. 15, no. 10, pp. 1842-1851, Oct. 1997.

[126] K. Y. Song, K. S. Abedin, K. Hotate, M. Gonzalez-Herráez, and L. Thévenaz, "Highly efficient Brillouin slow and fast light using As2Se3 chalcogenide fiber," Opt. Express, vol. 14, no. 13, pp. 5860-5865, Jun. 2006.

[127] K. S. Abedin, "Observation of strong stimulated Brillouin scattering in single-mode As2Se3 chalcogenide fiber," Opt. Express, vol. 13, no. 25, pp. 10266-10271, Dec. 2005.

[128] M. Gonzalez-Herráez, K.Y. Song., and L. Thévenaz, "Optically controlled slow and fast light in optical fibers using stimulated Brillouin scattering," Appl. Phys. Lett., vol. 87, no. 8, pp. 081113, Jan. 2005.

[129] S. Chin, M. Gonzalez-Herráez, and L. Thévenaz, "Zero-gain slow & fast light propagation in an optical fiber," Opt. Express, vol. 14, no. 22, pp. 10684-10692, Oct. 2006.

[130] Z. Zhu, D. J. Gauthier, Y. Okawachi, J. E. Sharping, A. L. Gaeta, R. W. Boyd, and A. E. Willner, "Numerical study of all-optical slow-light delays via stimulated Brillouin scattering in an optical fiber," J. Opt. Soc. Am. B, vol. 22, no. 11, pp. 2378-2384, Nov. 2005.

[131] R. W. Boyd, D. J. Gauthier, A. L. Gaeta, and A. E. Willner, "Maximum time delay achievable on propagation through a slow-light medium," Phys. Rev. A, vol. 71, no. 2, pp. 023801, Feb. 2005.

[132] D. A. B. Miller, "Fundamental Limit to Linear One-Dimensional Slow Light Structures," Phys. Rev. Lett., vol. 99, no. 20, pp. 203903, Jul. 2007.

[133] M. Gonzalez-Herraez and L. Thévenaz, "Physical limits to broadening compensation in a linear slow light systems," Opt. Express, vol. 17, no. 6, pp. 4732-4739, Mar. 2009.

[134] M. Lee, R. Pant, and M. A. Neifeld, "Improved slow-light delay performance of a broadband stimulated Brillouin scattering system using fiber Bragg gratings," Appl. Opt., vol. 47, no. 34, pp. 6404-6415, Dec. 2008.

[135] S. Chin and L. Thévenaz, "Optimized shaping of isolated pulses in Brillouin fiber slow-light systems," Opt. Lett., vol. 34, no. 6, pp. 707-709, Mar. 2009.

[136] M. D. Stenner and M. A. Neifeld, "Optimal pulse design for communication-oriented slow-light pulse detection," Opt. Express, vol. 16, no. 2, pp. 651-662, Jan. 2008.

[137] S. W. Chang, P. K. Kondratko, H. Su, and S. L. Chuang, "Slow light based on coherent population oscilation in quantum dots at room temprature," IEEE J. Quantum Electron., vol. 43, no. 2, pp. 196-205, Feb. 2007.

[138] M. S. Bigelow, N. N. Lepeshkin, and R.W. Boyd, “Observation of ultraslow light propagation in a ruby crystal at room temperature,” Phys. Rev. Lett., vol. 90, no. 11, pp. 113903, Mar. 2003.

[139] P. C. Ku, F. Sedgwick, C. Chang-Hasnain, P. Palinginis, T. Li, H. Wang, S. W. Chang, and S. L. Chuang, “Slow light in semiconductor quantum wells,” Opt. Lett., vol. 29, no. 19, pp. 2291-2293, Oct. 2004.

[140] P. Palinginis, F. Sedgwick, S. Crankshaw, M. Moewe, and C. J. Chang-Hasnain, “Room temperature slow light in a quantum-well waveguide via coherent population oscillation,” Opt. Express, vol. 13. no. 24, pp. 9909-9915, Nov. 2005.

[141] P. Palinginis, S. Crankshaw, F. Sedgwick, E.-T. Kim, M. Moewe, C. J. Chang-Hasnain, H. Wang, and S.-L. Chuang, “Ultraslow light (<200 m/s) propagation in a semiconductor nanostructure,” Appl. Phys. Lett., vol. 87, no. 17, pp. 171102-171102-3, Oct. 2005.

[142] F. Öhman, K. Yvind, and J. Mørk, “Voltage-controlled slow light in an integrated semiconductor structure with net gain,” Opt. Express, vol. 14, no. 21, pp. 9955-9962, Oct. 2006.

[143] H. Sue and S. L. Chuang, "Room temperature slow and fast light in quantum-dot semiconductor optical amplifiers," Appl. Phys. Lett., vol. 88, no. 6, pp. 061102-061104, Feb. 2006.

[144] P. K. Kondratko, S. W. Chang, H. Su, and S. L. Chuang, “Optical and electrical control of slow light in p-doped and intrinsic quantum-dot electroabsorbers,” Appl. Phys. Lett., vol. 90, no. 25, pp. 251108-251108-3, Jun. 2007.

[145] C. J. Chang-Hasnain and S. L. Chuang, “Slow and Fast Light in Semiconductor Quantum-Well and Quantum-Dot Devices,” J. Lightw. Technol., vol. 24, no. 12, pp. 4642-4654, Dec. 2006.

[146] M. V. D. Poel, J. Mørk, and J. M. Hvam, “Controllable delay of ultrashort pulses in a quantum dot optical amplifier,” Opt. Express, vo. 13, no. 20, pp. 8032-8037, Oct. 2005.

[147] F. Öhman, K. Yvind, and J. Mørk, "Slow light in a semiconductor waveguide for true-time delay applications in microwave photonics," IEEE Photon. Technol. Lett., vol. 19, no. 15, pp. 1145–1147, Aug. 2007.

[148] G. M. Gehring, A. Schweinsberg, C. Barsi, N. Kostinski, and R.W. Boyd , "Observation of backward pulse propagation through a medium with a negative group velocity," Science, vol. 312, no. 5775, pp. 895-897, May 2006.

[149] H. Shin, A. Schweinsberg, G. Gehring, K. Schwertz, H. J. Chang, R. W. Boyd, Q. H. Park, and D. J. Gauthier, "Reducing pulse distortion in fast-light pulse propagation through an erbium-doped fiber amplifier," Opt. Lett., vol. 32, no. 8, pp. 906-908, Apr. 2007.

[150] S. Sales, F. Öhman, A. Bermejo, J. Mørk, and J. Capmany, "Phased-array antennas employing slow and fast light in alternating amplifying and absorbing sections," MWP 2006, International Topical Meeting on Microwave Photonics, pp. 1-4, 2006.

[151] W. Xue, Y. Chen, F. Öhman, S. Sales, and J. Mørk, "Enhancing light slow-down in semiconductor optical amplifiers by optical filtering," Opt. Lett., vol. 33, no. 10, pp. 1084-1086, May 2008.

[152] E. Shumakher, S. O. Duill, and G. Eisenstein, "Optoelectronic oscillator tunable by an SOA based slow light element," J. Lightw. Technol.,vol. 27, no. 18, pp. 4063-4068, Sep. 2009.

[153] J. Sharping, Y. Okawachi, J. van Howe, C. Xu, Y. Wang, A. E. Willner, and A. L. Gaeta, "All-optical, wavelength and bandwidth preserving, pulse delay based on parametric wavelength conversion and dispersion," Opt. Express, vol. 13, no. 20, pp. 7872-7877, Oct. 2005.

[154] J. E. Sharping, Y. Okawachi, J. van Howe, C. Xu, and A. L. Gaeta, "All-optical, continuously tunable, nanosecond pulse delay using wavelength conversion and fiber dispersion," Conference on Lasers and Electro-Optics (CLEO) 2005, Baltimore, Maryland, USA, vol. 2, pp. 971-973.

[155] F. Morichetti, A. Melloni, C. Ferrari, and M. Martinelli, "Error-free continuously-tunable delay at 10 Gbit/s in a reconfigurable on-chip delay-line," Opt. Express, vol. 16, no. 12, pp. 8395-8405, Jun. 2008.

[156] A. Melloni, F. Morichetti, C. Ferrari, and M. Martinelli, "Continuously tunable 1 byte delay in coupled-resonator optical waveguides," Opt. Lett., vol. 33, no. 20, pp. 2389-2391, Oct. 2008.

[157] J. K. S. Poon, L. Zhu, G. A. DeRose, and A. Yariv, "Transmission and group delay of microring coupled-resonator optical waveguides," Opt. Lett., vol. 31, no. 4, pp. 456-458, Feb. 2006.

[158] M. S. Rasras, C. K. Madsen, M. A. Cappuzzo, E. Chen, L. T. Gomez, E. J. Laskowski, A. Griffin, A. Wong-Foy, A. Gasparyan, A. Kasper, J. Le Grange, and S. S. Patel, "Integrated resonance-enhanced variable optical delay lines," IEEE Photon. Technol. Lett., vol. 17, no. 4, pp. 834-836, Apr. 2005.

[159] L. Zhuang, C. G. H. Roeloffzen, R. G. Heideman, A. Borreman, A. Meijerink, and W. van Etten, "Single-chip ring resonator-based 1×8 optical beam forming network in CMOS-compatible waveguide technology," IEEE Photon. Technol. Lett., vol. 19, no. 15, pp. 1130-1132, Aug. 2007.

[160] J. Cardenas, M. A. Foster, N. Sherwood-Droz, C. B. Poitras, H. L. R. Lira, B. Zhang, A. L. Gaeta, J. B. Khurgin, P. Morton, and M. Lipson, "Wide-bandwidth continuously tunable optical delay line using silicon microring resonators," Opt. Express, vol. 25, no. 18, pp. 26525–26534, Dec. 2010.

[161] A. Melloni, F. Morichetti, and M. Martinelli, "Linear and nonlinear pulse propagation in coupled resonator slow-wave optical structures," Opt. Quant. Electron., vol. 35, no. 4-5, pp. 365-379 , Mar. 2003.

[162] T. Baba, "Slow light in photonic crystals," Nature Photon., vol. 2, no. 8, pp. 465-473, Aug. 2008.

[163] C. Y. Lin, X. Wang, S. Chakravarty, B. S. Lee, W. C. Lai, and R. T. Chen, "Wideband group velocity independent coupling into slow light silicon photonic crystal waveguide," Appl. Phys. Lett., vol. 97, no. 18, 183302, Nov. 2010.

[164] Y. Hamachi, Sh. Kubo, and T. Baba, "Slow light with low dispersion and nonlinear enhancement in a lattice-shifted photonic crystal waveguide," Opt. Lett., vol. 34, no. 7, pp. 1072-1074, Apr. 2009.

[165] C. Y. Lin, H. Subbaraman, A. Hosseini, A. X. Wang, L. Zhu, and R. T. Chen, “Silicon nanomembrane based photonic crystal waveguide array for wavelength-tunable true-time-delay lines,” Appl. Phys. Lett., vol. 101, no. 5, pp. 051101, 051101-4, Jul. 2012.

[166] Y. Jiang, W. Jiang, X. Chen, L. Gu, B. Howley, and R. T. Chen, “Nano-photonic crystal waveguides for ultra-compact tunable true time delay lines,” Proc. of SPIE, vol. 5733, pp. 166-175, Apr. 2005.

[167] J. Adachi, N. Ishikura, H. Sasaki, and T. Baba, “Wide range tuning of slow light pulse in SOI photonic crystal coupled waveguide via folded chirping,” IEEE J. Sel. Top. Quantum Electron., vol.16, no. 1, pp.192-199, Jan. 2010.

[168] A. Melloni, A. Canciamilla, C. Ferrari, F. Morichetti, L. O’Faolain, T. F. Krauss, R. De La Rue, A. Samarelli, and M. Sorel, “Tunable delay lines in silicon photonics: coupled resonators and photonic crystals, a comparison,” IEEE Photon. J., vol. 2, no.2, pp. 181-194, Apr. 2010.

[169] S. Khan, M. A. Baghban, and S. Fathpour, “Electronically tunable silicon photonic delay lines,” Opt. Express, vol. 19, no. 12, pp. 11780-11785, Jun. 2011.

[170] S. Khan and S. Fathpour, “Complementary apodized grating waveguides for tunable optical delay lines,” Opt. Express, vol. 20, no. 18, pp. 19859-19867, Aug. 2012.

[171] I. Giuntoni, D. Stolarek, D. I. Kroushkov, J. Bruns, L. Zimmermann, B. Tillack, and K. Petermann, “Continusouly tunable delay line based on SOI tapered Bragg gratings,” Opt. Express, vol. 20, no. 10, pp. 11241-11246, May 2012.

[172] K. O. Hill, B. Malo, F. Bilodeau, and D. C. Johnson, “Photosensitivity in optical fibers,” Annu. Rev. Mater. Sci., vol. 23, pp. 125-157, Aug. 1993.

[173] A. Yariv, “Coupled-mode theory for guided-wave optics,” IEEE J. Quantum Electron., vol. 9, no. 9, pp. 919-933, Sep. 1973.

[174] T. Erdogan, “Fiber grating spectra,” J. Lightw. Technol., vol. 15, no. 8, pp. 1277-1294, Aug. 1997.

[175] M. McCall, “On the application of coupled mode theory for modeling fiber Bragg gratings,” J. Lightw. Technol., vol. 18, no. 2, pp. 236-242, Feb. 2000.

[176] M. Yamada and K. Sakuda, “Analysis of almost-periodic distributed feedback slab waveguides via a fundamental matrix approach,” Appl. Opt., vol. 26, no. 16, pp. 3474-3478, Aug. 1987.

[177] M. K. Davis, M. J. F. Digonnet, and R. H. Pantell, “Thermal effects in doped fibers,” J. Lightw. Technol., vol. 16, no. 6, pp. 1013-1023, Jun. 1998.

[178] C. Kittel and H. Kroemer, Thermal Physics, 2nd ed. New York: W. H. Freeman, 1980.

[179] K. S. Lee and T. Erdogan, “Fiber mode coupling in tranmissive and reflective tilted fiber gratings,” Appl. Opt., vol. 39, no. 9, pp. 1394-1404, Mar. 2000.

[180] M. A. Muriel, J. Azana, and A. Carballar, “Real-time Fourier transformer based on fiber gratings,” Opt. Lett., vol. 24, no. 1, pp. 1-3, Jan. 1999.

[181] Y. Han, Z. Li, S. Pan, M. Li, and J. P. Yao, “Photonic-assisted tunable microwave pulse fractional Hilbert transformer based on a temporal pulse shaping system,” IEEE Photon. Technol. Lett., vol. 23, no. 9, pp. 570–572, May. 2011.

[182] H. Chi and J. P. Yao, “Symmetrical waveform generation based on temporal pulse shaping using amplitude-only modulator,” Electron. Lett., vol. 43, no. 7, pp. 415–417, Mar. 2007.

[183] Y. Dai and J. P. Yao, "Arbitrary phase-modulated RF signal generation based on optical pulse position modulation," J. Lightw. Technol., vol. 26, no. 19, pp. 3329–3336, Oct. 2008.

[184] L. Dong, B. Ortega, and L. Reekie, “Coupling characteristics of cladding modes in tilted optical fiber Bragg gratings,” Appl. Opt., vol. 36, no. 22, pp. 5099-5105, Aug. 1998.

[185] D. Sáez-Rodriguez, J. L. Cruz, A. Díez, and M. V. Andrés, “Coupling between counterpropagating cladding modes in fiber Bragg gratings,” Opt. Lett., vol. 36, no. 8, pp. 1518-1520, Apr. 2011.

[186] A. V. Oppenheim and J. S. Lim, “The importance of phase in signals,” Proc. of the IEEE, vol. 69, no. 5, pp. 529- 541, May 1981.

[187] E. J. Klein, “Densely integrated microring-resonator based components for fiber-to-the-home applications,” PhD thesis, University of Twente, 2007.

[188] A. Yariv, “Universal relations for coupling of optical power between microresonators and dielectric waveguides,” Electron. Lett., vol. 36, no. 4, pp. 321-322, Feb. 2000.

[189] D. X. Xu. A. Densmore, P. Waldron, J. Lapointe, E. Post, A. Delâge, S. Janz, P. Cheben, J. H. Schmid, and B. Lamontagne, “High bandwidth SOI photonic wire ring resonators using MMI couplers,” Opt. Express, vol. 15, no. 16, pp. 3149-3155, Mar. 2007.

[190] D. X. Xu, S. Janz, and P. Cheben, "Design of polarization-insensitive ring resonators in silicon-on-insulator using MMI couplers and cladding stress engineering," IEEE Photon. Technol. Lett., vol. 18, no. 2, pp. 343-345, Jan. 2006.

[191] H. H. Yaffe, C. H. Henry, R. F. Kazarinov, and M. A. Milbrodt, “Polarization-independent silica-on-silicon Mach-Zehnder interferometers,” J. Lightw. Technol., vol. 12, no. 1, pp. 64-67, Jan. 1994.

[192] A. Kilian, J. Kirchof, G. Przyrembel, and W. Wischmann, “Birefringence free planar optical waveguide made by flame hydrolysis deposition (FHD) through tailoring of the overcladding,” J. Lightw. Technol., vol. 18, no. 2, pp. 193-198, Feb. 2000.

[193] B. M. A. Rahman, N. Somasiri, and K. T. V. Grattan, “Birefringence compensation of silica waveguides,” IEEE Photon. Technol. Lett., vol. 17, no. 6, pp. 1205-1207, Jun. 2005.

[194] A. Melloni, R. Costa, G. Cusmai, and F. Morichetti, “The role of index contrast in dielectric optical waveguides,” Inter. J. Mater. Technol., vol. 34, no. 4, pp, 421-437, May 2009.

[195] G. Bourdon, G. Alibert, A. Beguin, B. Bellman, and E. Guiot, “Ultralow loss ring resonators using 3.5% index-contrast Ge-doped silica waveguides,” IEEE Photon. Technol. Lett., vol. 15, no. 5, pp. 709-711, May 2003.

[196] P. Dumais, C. Callender, C. Blanchetière, and C. Ledderhof, “High-contrast germanium-doped silica-on-silicon waveguides,” Photonics North 2012, Proc. Of SPIE, vol. 8412, id. 84120M, 2012.

PUBLICATION LIST

Refereed journal papers

[1] **H. Shahoei** and J. P. Yao, **"Delay lines,"** Wiley Encyclopedia of Electrical and Electronics Engineering, under revision.

[2] **H. Shahoei**, D. Xu, and J. P . Yao, “Continuous slow and fast light generation by a silicon-on-insulator microring resonator incorporating a MMI coupler,” under revision.

[3] **H. Shahoei**, P. Dumais, and J. P. Yao, “Continuously tunable photonic fractional Hilbert transformer using a high-contrast Germanium-doped silica-on-silicon microring resonator,” Opt. Lett., vol. 39, no. 9, May. 2014.

[4] **H. Shahoei**, D. Xu, J. Schmid, and J. P. Yao, “Photonic fractional-order differentiator using an SOI microring resonator with an MMI coupler,” IEEE Photon. Technol. Lett., vol. 25, no. 15, pp. 1408-1411, Aug. 2013.

[5] **H. Shahoei** and J. P. Yao, “A continuously tunable multi-tap complex-coefficient microwave photonic filter based on a tilted fiber Bragg grating,” Opt. Express, vol. 21, no. 6, pp. 7521-7527, Mar. 2013.

[6] **H. Shahoei** and J. P. Yao, “Tunable microwave photonic phase shifter based on slow and fast light effects in a tilted fiber Bragg grating,” Opt. Express, vol. 20, no. 13, pp. 14009-14014, Jun. 2012.

[7] **H. Shahoei** and J. P. Yao, “Continuously tunable chirped microwave waveform generation using a tilted fiber Bragg grating written in an erbium/ytterbium co-doped fiber,” IEEE Photon. J., vol. 4, no. 3, pp. 765-771, Jun. 2012.

[8] **H. Shahoei** and J. P. Yao, “Continuously tunable microwave frequency multiplication by optically pumping linearly chirped fiber Bragg gratings in an unbalanced temporal pulse shaping system,” J. Lightw. Technol., vol. 30, no. 12, pp. 1954-1959, Jun. 2012.

[9] **H. Shahoei** and J. P. Yao, "Continuously tunable slow and fast light by using an optically pumped tilted fiber Bragg grating written in an erbium/ytterbium co-doped fiber," IEEE Photon. Technol. Lett., vol. 24, no. 10, pp. 818-820, May 2012.

[10] **H. Shahoei**, J. Albert, and J. P. Yao, "Tunable fractional order temporal differentiator by optically pumping a tilted fiber Bragg grating," IEEE Photon. Technol. Lett., vol. 24, no. 9, pp. 7300-732, May 2012.

[11] **H. Shahoei**, M. Li , and J. P. Yao, "Continuously tunable time delay using an optically pumped linearly chirped fiber Bragg grating," J. Lightw. Technol., vol. 29, no. 10, pp. 1465-1472, May 2011.

Conference Papers and Talks

[1] **H. Shahoei** and J. P. Yao, "Slow and fast Light effects in a tilted fiber Bragg grating and the application in a continuously tunable microwave photonic filter," Microwave Symposium Digest (IMS), 2-7 June 2013, Seattle, WA, USA, pp. 1-3.

[2] **H. Shahoei** and J. P. Yao, "Continuously tunable microwave phase shifter based on a tilted fiber Bragg grating," Microwave Photonics (MWP), 11-14 September 2012, Amsterdam, The Netherlands, pp. 18-21.

[3] **H. Shahoei** and J. P. Yao, "Tunable fractional order temporal differentiator using an optically pumped tilted fiber Bragg grating," 2012 OSA Topical Meeting on Bragg Gratings, Photosensitivity, and Poling in Glass Waveguides, 17-21 June 2012, Colorado Springs, Colorado, USA, paper BW4E.2.

[4] **H. Shahoei** and J. P. Yao, "Continuously tunable chirped microwave pulse generation using an optically pumped tilted fiber Bragg grating," 2012 OSA Topical Meeting on Bragg Gratings, Photosensitivity, and Poling in Glass Waveguides, 17-21 June 2012, Colorado Springs, Colorado, USA, paper BW2E.4.

[5] **H. Shahoei** and J. P. Yao, "Achieving continuously tunable slow and fast light by using an optically pumped tilted fiber Bragg grating," 2012 IEEE Conference on Lasers and Electro-Optics (CLEO), 6-11 May 2012, San Jose, USA, paper JW4A.9.